Development of a Laser Based Inspection System for Surface Defect Detection

By

Mohammed Belal Hossain Bhuian, B. Sc. Eng.

This thesis is submitted as the fulfilment of the

Requirement for the award of degree of

Master of Engineering (MEng)

By research from

School of Mechanical & Manufacturing Engineering,

Dublin City University

April 2002

Research Supervisors:

Professor M. A. El Baradie

Dr. Dermot Brabazon

DECLARATION

I hereby certify that this material, which I now submit for assessment on the programme of study leading to the award of Master of Engineering is entirely my own work and has not been taken from the work of others save to the extent that such work has been cited and acknowledged within the text of my work

Signed: _____ ID No.: 98971247

Candidate

Date: 15/5/02

ACKNOWLEDGEMENTS

I would like to express my profound gratitude to my project supervisor Professor Mohie El Baradie for his supervision and guidance throughout the period of my research.

I am also very much grateful to my other supervisor Dr. Dermot Brabazon for his friendly supports and advice, which was very instrumental to bring about this work.

I would like to thank the European Commission for the funding of the project (BRITE/EURAM, project no BE-5049). It was a privilege for me to have been able to work in this project.

I am indebted to Liam Domican, Michael May, Keith Hickey, Jim Barry, Martina Reddy and all other staffs in the school for the contribution they made and the co-operation they offered to the success of the project.

I would like to thank Professor M. S. J Hashmi for his all kind of support during my study.

My thanks are upon all the fellow postgraduate students and all the Bangladeshi students. I must thank all the members (Ekhlas, Duke, Tarik, Rudra, Harun, and Mahbub) of the so called "Seven Star" group, which provided a lots of fun in my life in Dublin.

Finally, and specially, I would like to thank my family back in Bangladesh for their love and encouragement throughout the period of my study.

DEDICATION

To my parents

Abstract

Development of a Laser Based Inspection System for Surface Defect Detection

By

Mohammed Belal Hossain Bhuian

The objective of this project was to design and develop a laser based inspection system for the detection of surface defects and to assess its potentiality for high-speed online applications. The basic components of this inspection system are a laser diode module as illumination source, a random access CMOS camera as detector unit, and an XYZ translation stage. Algorithms were developed to analyze the data obtained from the scanning of different sample surfaces. The inspection system was based on optical triangulation principle. The laser beam was incident obliquely to the sample surface. Differences in surface height were then detected as a horizontal shift of the laser spot on the sample surface. This enabled height measurements to be taken, as per the triangulation method.

The developed inspection system was first calibrated in order to obtain a conversion factor that would render a relationship between the measured spot shift on the sensor and the vertical displacement of the surface. Experiments were carried out on different sample material surfaces: brass, aluminum and stainless steel. The developed system is able to accurately generate three-dimensional topographic maps of the defects presented to it in this work. A spatial resolution of approximately 70 μm and a depth resolution of 60 μm were achieved. Characterization of the inspection system was also performed by measuring the accuracy of distance measurements.

Table of contents

Chapter One

1 Introduction.

Inspection plays an important role in modern manufacturing processes in order to evaluate part surface properties. In industry, the need to inspect the part surfaces is the result of the need to ensure high quality. Control of surface quality is of importance in manufacturing operations such as in semiconductor wafer growth; very large scale integrated (VLSI) circuit chips, paper production, and fabrication of automotive and other mechanical parts. In advanced automated production systems, surface defect detection systems are employed not but also to reduce costs. These include raw material scrap costs and labor charges incurred to test the product.

In the production process it is possible to develop different types of defects on the part surface. Defects that occur on the surface or different materials are of different types. The most common defects are holes, pits, bubbles, scratches on the surface, indentation, foreign particles, imperfect polish of the surface, stain. Visual inspection process as for locating those defects is extremely important to increase yield. One of the reasons that on line inspection systems for defect detection are in high demand is due to the increased production speed. Current techniques of surface measurement use contact methods such as surface profilometers and co-ordinate measuring machines and non-contact methods such as optical inspection systems. However, contact methods are inherently slow in acquiring point data since they need to make physical contact with a part surface for every point that is sampled. Optical inspection systems have found widespread acceptance in industrial manufacturing for increasing productivity, product quality and process control. In order to perform on-line optical inspection of surfaces, the inspection devices need to be able to quickly obtain a large amount of point data from the surface, which might include a high-speed data processing unit to deal with the enormous amount of data generated. So a typical optical inspection system consists of a laser diode module as a monochromatic illumination source, an optical laser scanner, a detection unit (camera) and the data processing unit.

In the present system, a laser based optical inspection system is developed in order to detect surface defects. The inspection system consists of a laser diode module as the illumination source and a random access CCf15 camera as the detection unit. Scanning of the surface was performed by mounting the sample part on a XYZ translation stage and manually incrementing it. Data processing task was carried out by the software developed using LabVIEW. Development of the inspection system required specifications such as designing the laser beam focusing lens and objective lens parameters, as well as the incident angle and the observation angle of the laser beam. This laser based inspection system can generate a three-dimensional topographic map of a surface using the optical triangulation principle. This map can then be compared later on with the topographical map of a surface with no defects and thereby detect surface defects. The objective of this project was to assess the capability of the inspection system in generating three-dimensional topographic maps of surfaces and the potential for the development of a high-speed online inspection system. For the scanning system developed a spatial resolution of 70μm and depth resolution of 60μm were achieved.

This thesis is organized into seven chapters and five appendices. In chapter two, literature survey is carried out. It mainly covers the basic theory of lasers and their properties, different scanning technologies and different surface inspection methods previously carried out by different researchers. Chapter three describes the triangulation method and the measurement principle of the current inspection system.

Chapter four gives a detailed outline of the different components used to develop the inspection system. Descriptions of the laser diode module, detector unit, various other optical equipment and the mechanical design are presented. Chapter four also explains the different data processing algorithms used to develop the software for the inspection system. These algorithms include conversion of the BMP image format to text format and the detection of the laser beam spot centroid position on the image.

Chapter five contains the experimental results obtained from using the developed inspection system. These include calibration and characterization of the system.

Chapter six is the discussion and chapter seven outlines the conclusions and the recommendations for further work.

Chapter Two

2 Literature Survey

This chapter deals with the literature survey carried out prior to the development of a surface defect sensor. The chapter is broken into three main sections. The first section describes lasers as light source. The second section reviews laser-scanning systems. Different methods of range data measurement are described in the last section.

2.1 Lasers

Laser is an acronym for Light Amplification by Stimulated Emission Radiation. Stimulated emission is the process by which light passing through a fluorescing substance is amplified. With sufficient amplification, a powerful, highly directional beam can be propagated. The laser is a unique source that simultaneously produces both coherent (in-phase) and monochromatic (single-wavelength) radiation. Laser light has propagation characteristics that make possible numerous applications that cannot be achieved with random or collimated sources.

2.1.1 Principle of Laser Operation

Laser [1-6] radiation originates from electronic transitions in atoms or molecules, involving both absorption and emission of electromagnetic radiation. Three types of transitions involving photons in laser operation are of interest: absorption, spontaneous emission, and stimulated emission [1]. Absorption occurs when a photon with energy equal to the energy difference between two levels is absorbed, and the atom or molecule is excited to a higher energy level. In spontaneous emission, an electron descends from a higher energy levels to a lower level and as a result a photon is emitted. In stimulated emission, an electron also descends from higher energy level to lower energy level. This process, however, is not random, but it is triggered by external radiation or photon that interacts with the atom. The released radiation is coherent with triggering radiation. In stimulated emission, the released radiation is coherent with the triggering radiation. It has the exact same frequency, is in the same

phase, and travels in the same direction [1]. Thus it can be said that amplification of light has taken place.

In a laser the amplification is provided by the stimulated emission process. This takes place in an optical medium that has two or more electron levels. The energy levels in typical two level medium are shown schematically in the figure 2.1, where level 1 represents the higher energy level and level 0, and the lower. Stimulated emission takes place at the condition when N1>N0 and then the applied radiation are amplified. This condition is called population inversion [1].

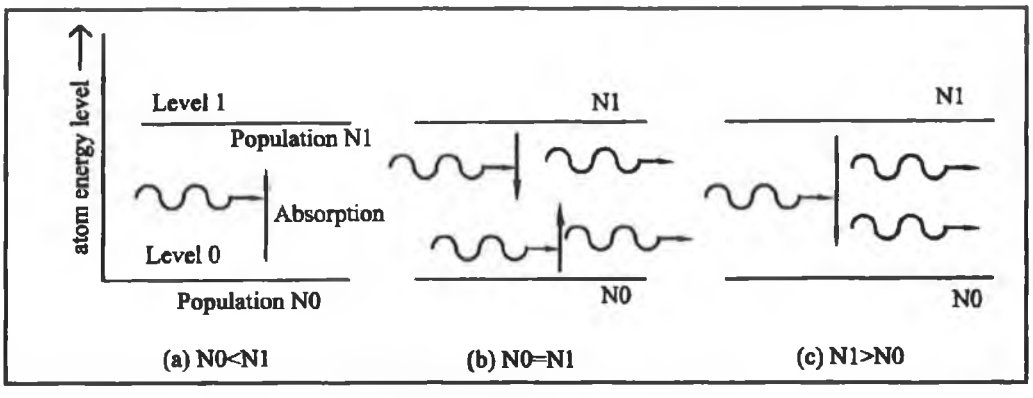

Figure 2.1: Absorption and emission in a two-level laser system [1]

A laser device, which is also called a laser oscillator, requires a resonator in which feedback of light occurs [3]. The laser device needs a power supply to provide the energy. In lasers the energy is supplied by lifting the elections to a higher energy level. This is called pumping. Pumping can be achieved in many ways: high intensity radiation, high temperature, and electric current [1]. The optical resonator, because of its geometrical configuration, provides for a highly unidirectional output. At the same time, through the feedback process, sufficient stimulated radiation in the laser is produced to ensure a high number of energy.

Feedback in the oscillator is achieved through forming a laser cavity as shown in figure 2.2. Light is confined to the lasing cavity by two mirrors, one of which partially transmits to form the output beam. This light confinement process produces a standing wave. Stimulated emission in the resonator cavity occurs with the same phase as that of the standing wave [3]. The combined action of the resonator and

stimulated emission produces an extremely bright light source even for lasers of relatively low power output.

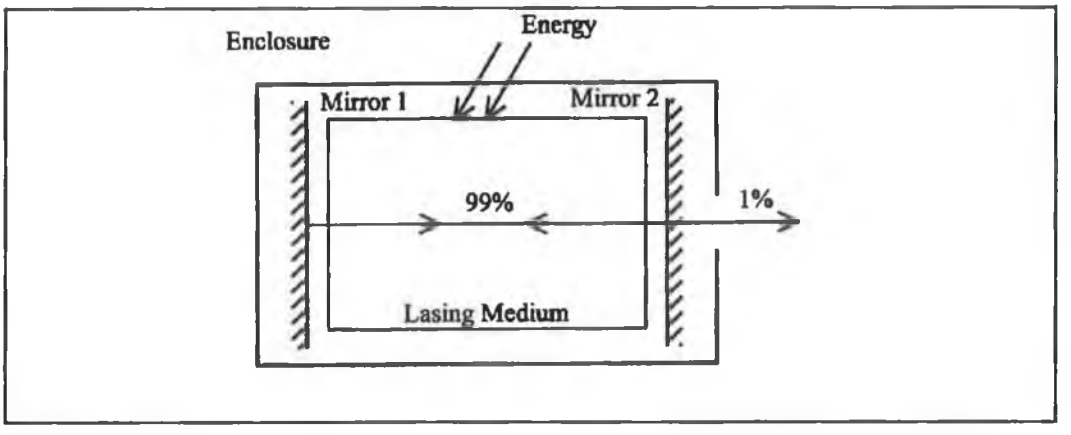

Figure 2.2: Feedback and tuning method in laser cavity.

2.1.2 Types of Lasers

Lasers can be classified by the lasing medium or pumping methods [1]. The first determines the laser wavelength, and the latter, output power and operating mode. Lasers can be operated in three modes: continuous output, pulsed, and pulse with very short duration (Q-switched) mode. Figure 2.3 shows a classification based on lasing medium. Lasers Classified according to the lasing medium are described in the following section.

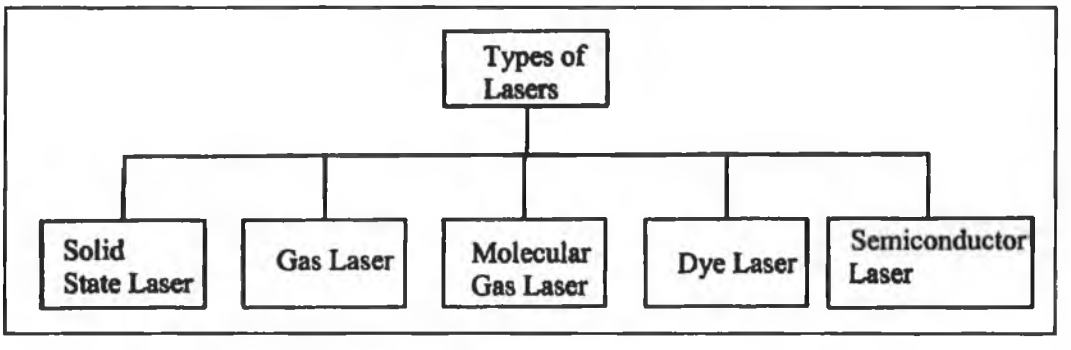

Figure 2.3: Classification of lasers.

Solid State Lasers

The ruby and YAG laser are the two common solid state lasers. The ruby laser uses a ruby crystal ($Al_2O_3:Cr^{3+}$) as lasing medium. The ruby rod is pumped with an intense

pulse of light produced by a flashbulb. The cavity is formed by two mirrors at the end of the rod or by polished and coated rod ends. It radiates a red light of 694-nm wavelength. In a YAG laser the lasing medium is an yttrium aluminum garnet ($Y_3A_{l5}O_{12}$) crystal. YAG lasers are operated continuously or at high repetition rates with average or continuous power output of from a few watts to 1 kW. The laser is optically pumped by a flash lamp or a high intensity xenon (Xe) or krypton (Kr) lamp. Their output is near infrared, with a wavelength of 1.06 μm. Solid state lasers are used for general research, and development work, holography, materials working, and communications.

Gas Lasers

The helium-neon (He-Ne) laser is the most common gas laser. The He-Ne laser consists of a sealed glass tube filled with He-Ne gas mixture under low pressure. Pumping is accomplished by two high voltage electrodes inserted into the tube that carry current through the gas causing population inversion. The mirrored ends of the tube or separate mirrors provide feedback and resonance cavity action [1]. The energy is transferred rapidly to a neutral neon atom, which has an energy level that is very slightly below that of the helium atom. Lasing takes place at three wavelengths, 633nm, 1150 nm, and 3390nm. The laser can deliver up to 50mW at 633 nm and less at longer wavelengths. It operates in continuos wave (CW) mode. Because of its low cost, simplicity, and reliability the He-Ne laser is the most widely used laser. It has numerous applications in alignment, holography, reprographics, measurement, and many other fields.

Molecular Gas Lasers

The carbon dioxide (CO_2) laser is a molecular laser in which molecular vibrations rather than electric transitions provide the lasing action [6]. The lasing medium is CO_2 and N_2 mixed with He under low pressure. The gas is circulated between two high voltage electrodes that provide the pumping energy. The important transition occurs between vibrational energy levels of the CO_2 molecules. Even a small, continuous CO_2 laser is capable of emitting a fraction of a watt and can heat most materials to

incandescence in a short time. The CO_2 laser can emit wavelengths between 9000 and 11000 nm (typically 9600 and 10600 nm in infrared range). The laser can operate in CW and pulsed mode. Applications for this laser are numerous and include cutting, hole piercing, welding, heat treatment, scribing, and marking.

Dye Lasers

Liquid or dye lasers are a group of lasers that are capable of delivering radiation over a wide wavelength range [1]. The lasing medium in these lasers consists of certain organic dye compounds dissolved in ethyl alcohol, methyl alcohol, or water. By using several dyes, it is possible to obtain thousands of distinct, closely spaced wavelengths in the visible part of the spectrum from a single laser. Depending of the dye selected, a tunable output range from 300 nm to 1000 nm may be achieved. These lasers are pumped by xenon lamp, argon laser, nitrogen laser, excimer laser, or frequently multiplied neodymium yttrium-aluminum-garnet (Nd-YAG) laser [3]. The output of dye lasers is normally pulsed. Dye lasers are used in spectroscopy, photochemical reaction studies, pollution detection, and surgery.

Semiconductor Laser

This type of laser is also known as a diode laser. In principle, the laser diode is an light emitting diode (LED) with an added optical cavity that provides feedback and generates stimulated emission. Optical feedback in diode lasers is achieved by using the reflections from carefully cleaved end faces of the semiconductor [5]. The cavity is completed by polishing the emitting sides. Because of the high refractive index of the material, the polished faces have sufficient reflectance to allow oscillation. Radiation therefore takes place from both sides of the device. Often a photodiode is attached to the inactive side, to work as a sensor for the power supply and control the output of the diode. The diode laser emits coherent radiation with a much narrower wavelength spread than the incoherent emission of an LED.

A schematic of the essential elements in an injection laser diode is shown in Figure 2.4 [2]. Modern diode lasers are chiefly composed of a variety of ternary compounds, such as $GaAl_xAs_{1-x}$ $(0 \le x \le 1)$. The shaded layer indicates the laser cavity. The active

medium (p-GaAs), where lasing occurs, is sandwiched between two cladding layers of both higher bandgap and lower refractive index. This structure is on a substrate (p-GaAs) ; a contact layer to facilitate electrical connection is deposited on top of the stack. In operation, the p-n junction is forward biased; this causes charge carriers (holes and electrons) to be injected from the cladding layer into the active region, where they are confined by the energy barrier between adjacent layers.

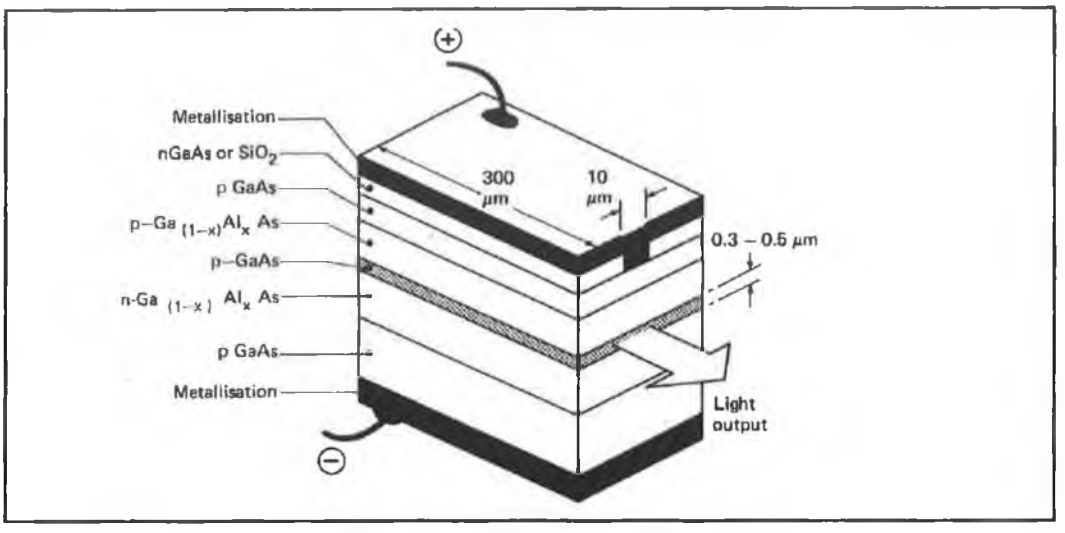

Figure 2.4: Structure of a double-heterojunction laser diode [2]

Carrier recombination in the active region produces light, which is confined to this region by the surrounding regions of lower index. A photon produced by recombination can cause other carriers to recombine and emit photons coherent with the first (stimulated emission). As current increases in the active region, the gain due to stimulated emission eventually exceeds the intrinsic losses in the cavity due to absorption, and the device emits laser beam radiation. The radiation pattern from a laser diode is similar to the pattern from the edge-emitting LED, as shown in the figure 2.5.

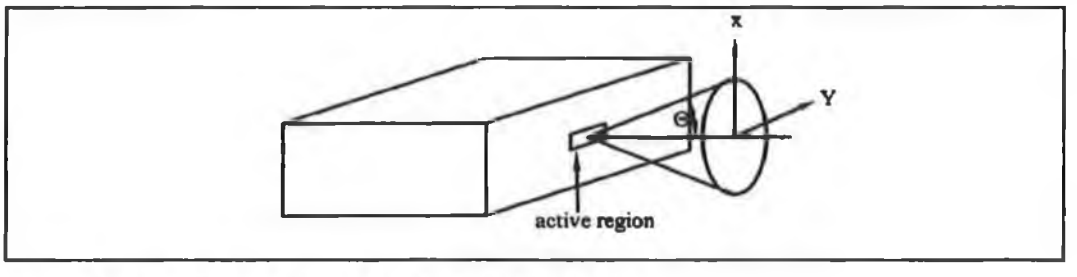

Figure 2.5: Radiation pattern from a laser diode [1]

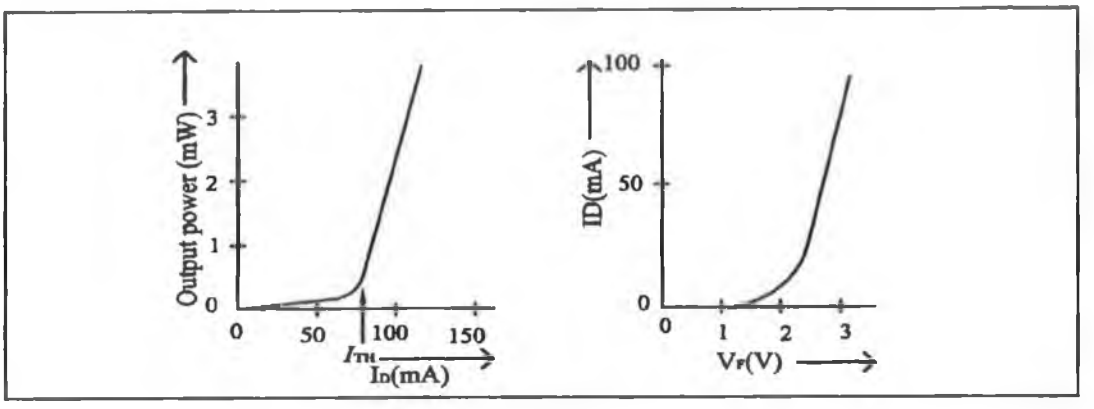

Figure 2.6: (a) Output power versus current (b) forward current versus voltage [1]

A typical output power-current relationship is shown for lasers in figure 2.6(a). The current voltage characteristic of the laser diode is similar to any semiconductor diode, as seen in figure 2.6(b). The output power versus forward current curve is however quite different. Initially the laser diode behaves identically to an LED but when the forward current reaches the threshold current, I_{TH}, the device starts operating as a laser. Figure 2.7 shows the sensitivity of threshold current to temperature. The threshold current increases about 1.5% per °C. Thus the device has the ability to turn itself off after warming up.

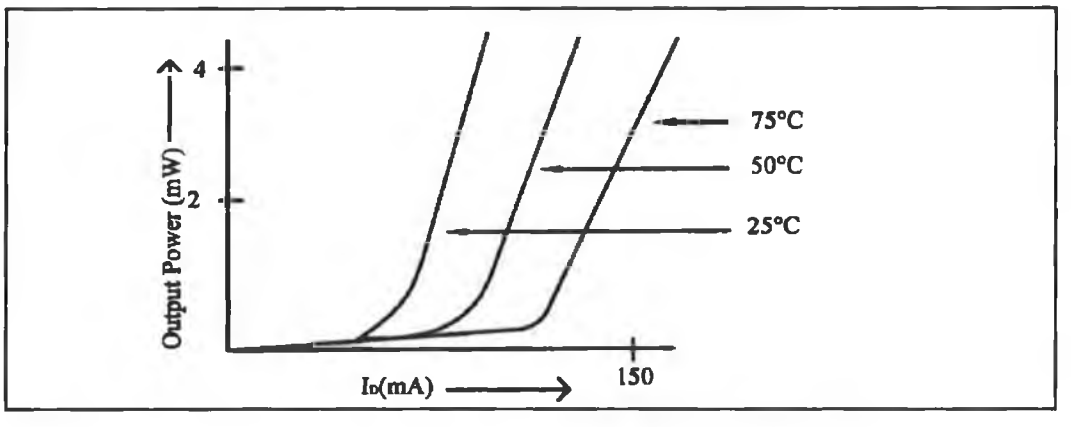

Figure 2.7: Effect of temperature on threshold current and output power [1]

Two types of laser diodes are commonly used: index guided and gain guided. In index-guided laser diodes, the active layer material has a refractive index larger than that of the material surrounding the layer. This index difference guides the laser radiation within the diodes and confines the beam to both the transverse and vertical

directions. Because of the large confinement and good guidance of the beam, index-guided laser diodes are more likely to operate with a single longitudinal mode, and hence are widely used in those applications requiring good quality beams. In gain-guided laser diodes, the refractive indices of the active layer material and its surrounding material are the same. However the lasing process taking place inside the active layer will slightly increase the index of the active layer. The resultant weak confinement and guidance of the beam makes gain guided laser diodes more likely to operate with multi-longitudinal modes and multi-transverse modes.

2.1.3 Properties of Laser Beam

Laser beams provide a source of high intensity light. The radiation that it emits is not fundamentally different than any other form of electromagnetic radiation. Laser beam shows some remarkable properties that are not available from other light source.

2.1.3.1 Coherence

One of the characteristics of stimulated emission is that the stimulated wave is in phase with the stimulating wave; that is, the spatial and temporal variation of the electric field of the two waves is the same [5]. So lasers have high degree of spatial and temporal coherence. Temporal coherence refers to correlation of the electromagnetic waves in phase at the same point in space at different times [6]. If the phase changes uniformly with time then the beam is said to show perfect temporal coherence. The temporal coherence of a He-Ne laser can be extend for hundreds of meters, while a typical diode laser will have a coherence length of around 8 meters. By contrast an incandescent source has a coherence length of a few tens of millimeters.

Spatial coherence refers to correlation in phase at the same time but at different points in space. Spatial coherence may be appreciated by considering two points that are on the same part of a wave front. The length in the transverse direction (perpendicular to the direction of propagation of laser light) over which the phase front is constant is called the coherent length. If a laser beam with a coherence length, x_c, is focused by a lens, the diameter D of the beam spot (see figure 2.8) is given as:

$$\Delta D \cong 2.44\lambda f / x_c \qquad 2.1$$

This spot size is called the diffraction limit and the ability to focus a laser beam to that limit is one of the features of spatial coherence [3].

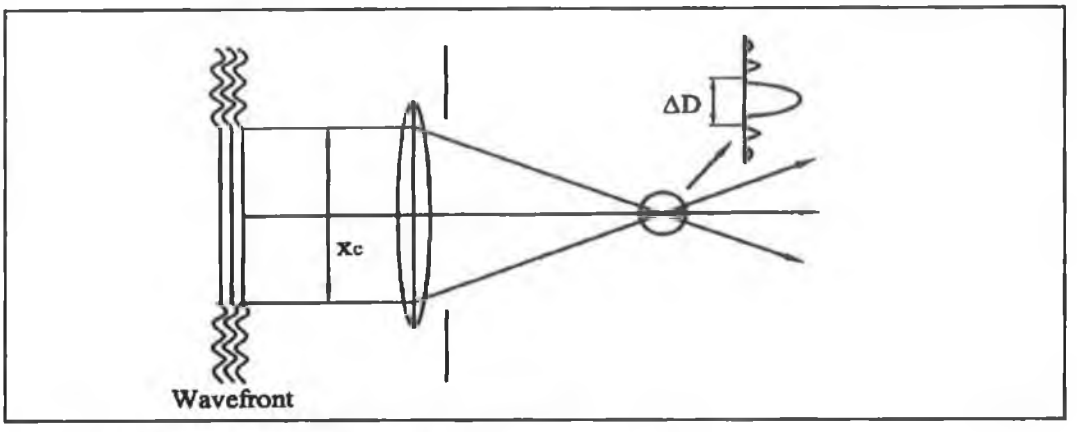

Figure 2.8: Spatial coherence and focusing spot [3]

Although laser beams are said to be coherent light sources, they are not completely coherent. While the coherence of the output from continuous wave (CW) gas lasers can be very high, that from pulsed lasers is usually somewhat lower.

Coherence is important in any application where the laser beam is split into parts that traverse different distances. These include the interferometric measurement of distance and holography. While coherence is essential for interference systems it can be a significant disadvantage in other applications. It is the coherence property of laser beam that causes speckle [7]. Speckle is caused by constructive and destructive interference between wavelets formed by different light scattering from an object surface. Speckle can be used in some measurement applications, but can create problems in others.

2.1.3.2 Oscillation Modes

It has been described that laser is a light oscillator and the space between its two end mirrors forms the resonating cavity. Unless special measures are adopted, the cavity will accommodate several strings of standing waves called mode [2].

Longitudinal Modes

Like an air whistle, in which more than one tone can be sustained by the resonator length, a laser can sustain oscillation of more than just one frequency. As long as an integer number of half-waves fits neatly into the cavity length and provided there is sufficient system gain, an oscillation may be sustained. Those frequencies and wavelength at which stable oscillations of this kind actually exist in a laser characterize its longitudinal modes. Only a very few of the mathematically possible longitudinal modes exist in a laser, namely those that fit the energy level transition equation.

$$\Delta E = E_2 - E_1 = hf \qquad 2.2$$

Figure 2.9 shows the spectral pattern of the longitudinal mode laser. There are multiple peaks at a range of wavelengths.

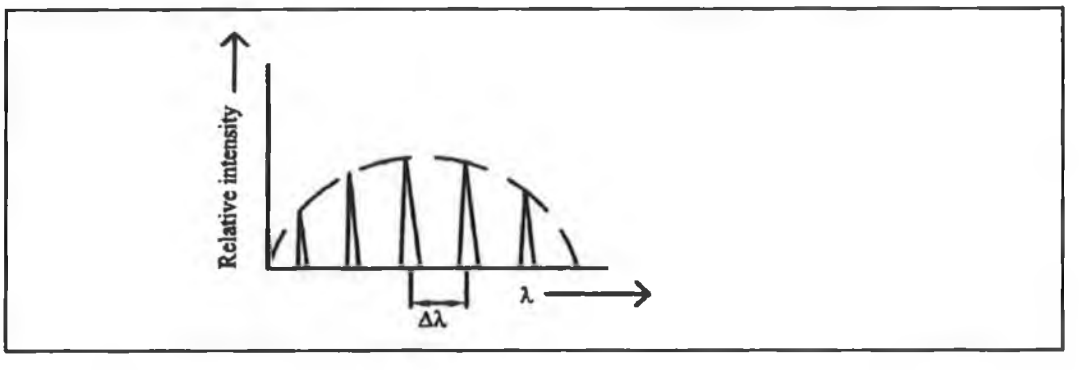

Figure 2.9: Radiation pattern of a multimode laser [1]

Transverse Modes

A mode that has a field vector normal to the direction of propagation is called transverse mode. In the transverse electromagnetic mode (TEM), both the electric and magnetic field vectors are normal to the propagation direction. In diode lasers, these are spatial modes perpendicular to the active layer. These are most easily understood in terms of a cavity such as a confocal cavity. The confocal cavity shown in figure 2.10 has two identical mirrors with a common focus at w_o.

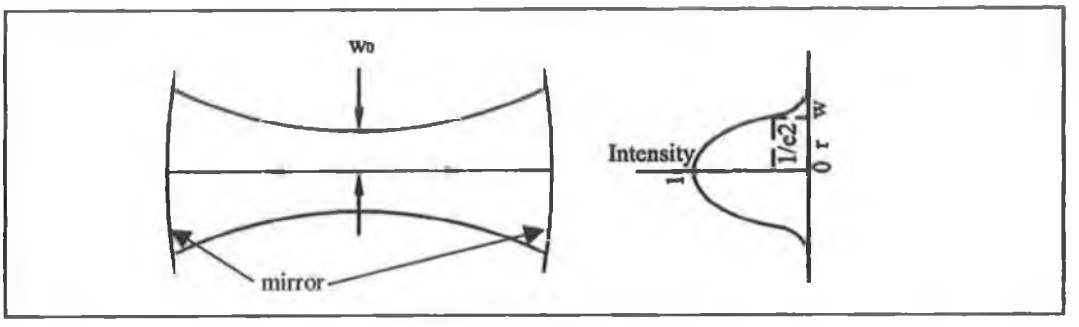

Figure 2.10: Transverse mode in a confocal cavity. [4]

The simplest mode in a confocal cavity is described by a ray that travels back and forth along its axis (see figure 2.10). This is the "TEM_{00} mode" or fundamental mode. The output of a laser oscillating in this mode is a spherical wave with gaussian intensity distribution. Its projection gives a single spot, a circular bright zone, fading gradually away, outward from the center as shown in the figure 2.11(a). The beam width is usually expressed as the radius w at which the beam intensity falls to $1/e^2$ of its maximum value [4].

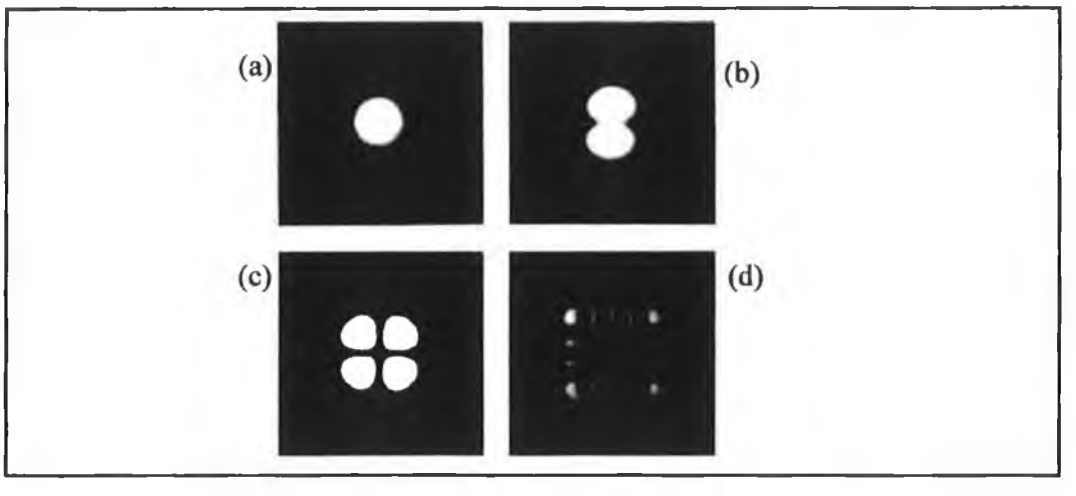

Figure 2.11: Laser transverse mode-patterns [4]

The next simplest modes are shown in figure 2.11(b), 2.11(c) and 2.11(d). This mode will oscillate only if the aperture is large enough. The output is a spherical wave with the intensity distribution shown.

2.1.3.3 Gaussian Beam

Beam Diameter

Laser oscillating in the TEM_{00} mode emits a beam with gaussian intensity distribution. Higher order modes also exhibit gaussian intensity distributions, multiplied by certain polynomials. The field distribution in any curved-mirror cavity is characterized by a beam waist as shown in figure 2.10. The beam waist is located in the center of the cavity [4]. The irradiance intensity distribution in the plane of the waist is gaussian for TEM_{00} mode. That is,

$$I(r) = \exp\left(-2r^2/w_0^2\right) \qquad 2.3$$

where r is the distance from the center of the beam. For convenience, the intensity is normalized to 1 at the center of the beam. When $r=w_o$ (see figure 2.10), the intensity is $1/e^2$ times the intensity at the center and width of that gaussian intensity profile changes along the axis. The parameter w_o is often called the beam radius or spot size, and $2w_o$, the beam diameter [8]. The gaussian beam contracts to a minimum diameter $2w_o$ at the beam waist where the phase front is plane.

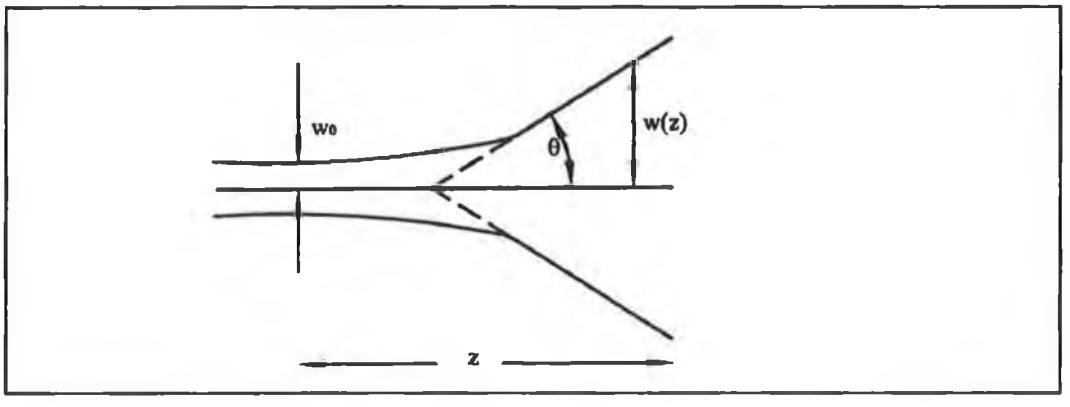

Figure 2.12: Propagation of Gaussian laser beam [4]

Figure 2.12 shows the propagation of gaussian beam. Both inside and outside the cavity, it retains its gaussian profile. At a distance z from the beam waist, w (z), is given by the following equation

$$w(z) = w_o\left[1+\left(\frac{\lambda z}{\pi w_o^2}\right)^2\right]^{1/2} \qquad 2.4$$

Where λ is the wavelength of the laser radiation [4].

Beam Divergence

One of the important features of most lasers is that the output is in the form of an almost parallel beam. This is very useful feature for a number of applications since it means that it is very easy to collect the emitted radiation and focus it onto a small area using a simple lens system. However, laser beams are not perfectly parallel, the beam exhibits a slight divergence. This is due to diffraction caused by the wave nature of light. From equation 2.4 it can be seen that at large distances z from the beam waist, the term in brackets becomes much larger than 1. In this case, the gaussian beam diverges with angle θ, where

$$\theta = \lambda/\pi w_o \qquad 2.5$$

This is the far-field divergence of a gaussian beam (see figure 2.12) [4]. The radiation converges toward a beam waist and diverges away from it. Therefore, the wavefront must be plane at the beam waist. At a distance z from the waist, the radius of curvature R (z) of the wavefront is

$$R(z) = z\left[1+\left(\frac{\pi w_o^2}{\lambda z}\right)^2\right] \qquad 2.6$$

Focusing the Laser Beam

Focusing ability is important in many laser applications. Some lasers are capable of being focused to what is called a diffraction limited beam spot. This is the smallest spot size attainable by any optical system. It also means a laser beam cannot be focused infinitely smaller. The diameter of the focused beam is governed by the focal length of the optics used and the divergence of beam. As values of divergence increase, a lens of short focal length will concentrate more power on the focal area. Focal length, f, divergence, θ, and beam diameter, d, are related by the equation

$$d = f\theta \qquad 2.7$$

Where f is the focal length of the lens and θ is the divergence of the laser beam [5].

2.1.3.4 Brightness

Brightness is defined as the power emitted per unit solid angle. It has been discussed in the earlier section that the divergence of laser beam is generally very small compared to the conventional sources. Thus although a similar amount of power may be involved, the small solid angle into which the laser beam is emitted ensures a corresponding high brightness

2.1.3.5 Monochromaticity

Laser beams tend to emit all photons at the same energy, thus it has constant wavelength. This property is called the monochromaticity. However, no light source can be perfectly monochromatic. Lasers tend to be relatively monochromatic but this depends on the type of laser in question. Monochromatic output is of great importance for lasers being used on interferometric measurements. For example constant wavelength used as a measure of length or distance, it must be known with extreme precision. It must also remain constant with time. The same holds true for lasers used in chemical and many other scientific analytical applications.

2.1.3.6 Astigmatism

Astigmatism is an inherent property of the output beam of diode lasers. Astigmatism is a condition in which the apparent focal points of the two axes do not coincide. It limits the ability to focus the laser beam to a small spot size In applications requiring collimation or transformation of the diode laser's beam, this astigmatism must be considered, and often corrected, if the final wavefront is to approach the diffraction limit.

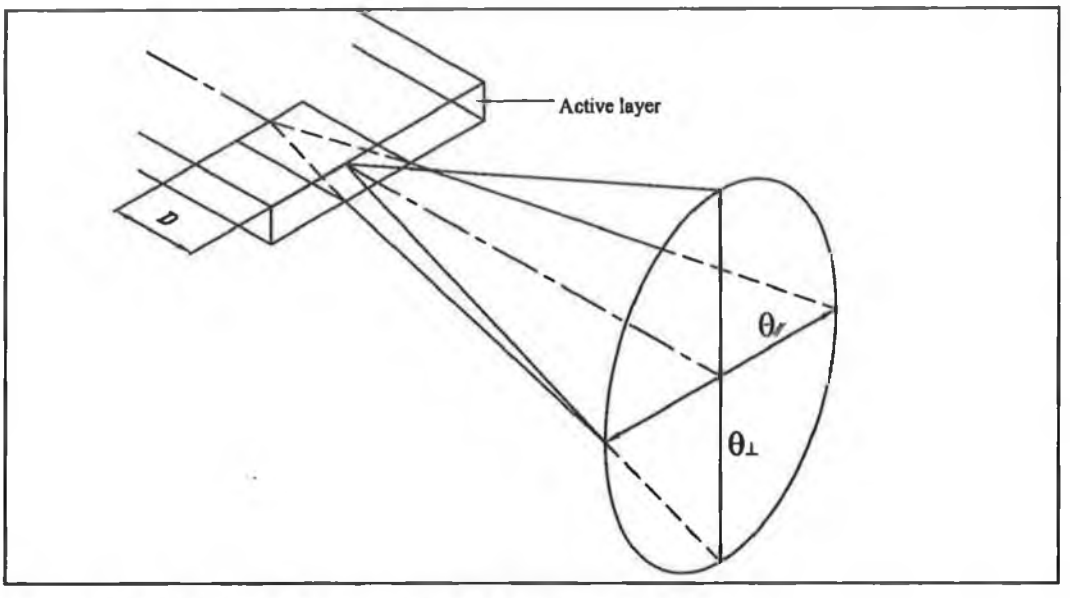

Figure 2.13: Amount of astigmatism in a laser diode.

In gain guided lasers, the wavefront exiting from the diode laser is elliptical. The beam waist perpendicular to the junction plain is still located at the output facet of the diode laser, but the waist parallel to the junction plane is displaced a distance, D, behind the facet as shown in the figure 2.13. This distance is the longitudinal astigmatism inherent in the diode laser. For index guided lasers there is less astigmatism.

2.1.4 Applications of Lasers

The application of lasers involves a wide range of fields: laser materials processing, communications and information processing, medical applications, analysis and testing, alignment, gauging and inspection to name a few [9].

Material processing is a general term that involves common processes such as cutting; welding and drilling. The concentrated energy of high power lasers makes them useful tools for many materials processing applications. Laser material processing has an advantage over more conventional methods involving mechanical drills or saws because the laser beam does not require physical contact with the material. Laser tools are versatile and can be used to manipulate metals, plastics, cloth, leather, wood, ceramics, etc. Lasers are excellent for applications on a miniature scale, as required in microelectronics. Laser processing is adaptable for easy automation and provides freedom from tool wear.

The use of light in information processing and communication has increased rapidly. Light offers several advantages over other technologies. The unique properties of laser light such as monochromaticity and coherence have created new areas of information manipulation that were not possible before. Conventional electronic communications relies on electrons passing through wires. Since optical fiber has no metallic components, electromagnetic interference is not and issue. Other applications involve optical storage devices such as the compact disk (CD), information manipulation using barcodes and laser printers. Laser scanning is also used to generate images.

The laser's concentrated energy is the reason the laser plays an increasingly large role in therapeutic medical applications. This energy provided by medium to high power lasers allows surgeons to cut tissue and cauterize the incision simultaneously. Various wavelengths of light are absorbed at different levels by different types of tissue. The surface area and depth of the laser beam can be controlled by taking advantage of tissue properties and by controlling the beams parameters. Common areas of laser surgery include ophthalmology (i.e. retinal detachment), dermatology and diagnostic applications.

Laser applications also include distance measurement, non-destructive testing spectroscopy and other forms of analysis. Accurate distance measurements as small as a wavelength of light or as large as several kilometers can be measured due to the optical properties of the laser beam. The uni-directionality of the beam provides for long-distance projection and range finding. The coherence of the laser beam allows

the use of interference effects to discover changes in stressed objects and minute changes in distance.

Holograms are three-dimensional pictures formed by the interference effects of laser beams. Holographic interferometry is the interferometric analysis of a complex object by utilizing the three-dimensional hologram. By causing a laser beam to diverge into two directions, one of which directly strikes a holographic recording medium and one of which is diffusely reflected to the medium, an interference pattern of fringes may be formed on a photographic plate, and upon reconstruction produces hologram. Holographic interferometry is used in the nondestructive testing of manufactured parts and materials [10].

Many of the most sophisticated uses of lasers involve measuring wavelengths of light absorbed and emitted by various materials; this discipline is referred to as spectroscopy. Observations of light emitted from can identify materials, reference the quantities present and help in studying their properties. Spectroscopy can determine the types and concentration of elements and compounds in an unknown chemical through the amount of light that has been absorbed. Laser spectroscopy involves the study of the theory and interpretation of spectra.

2.2 Laser Scanning Systems

Scanning systems have been used to achieve uniform product quality at high throughput speed. Optical scanning may be represented by the convolution of a point-spread function over an information-bearing surface [11]. The information of the surface may appear as an image or as a signal for subsequent computation. Scanning involves the controlled sampling and the synchronous restoration of a sequence of data points. The more closely spaced the samples, the higher the resolution.

2.2.1 Classification of Laser Scan Technology

A laser beam can be used for scanning when used in conjunction with different types of deflectors. Figure 2.14 illustrates one classification of laser scan technology: high and low inertia scanners.

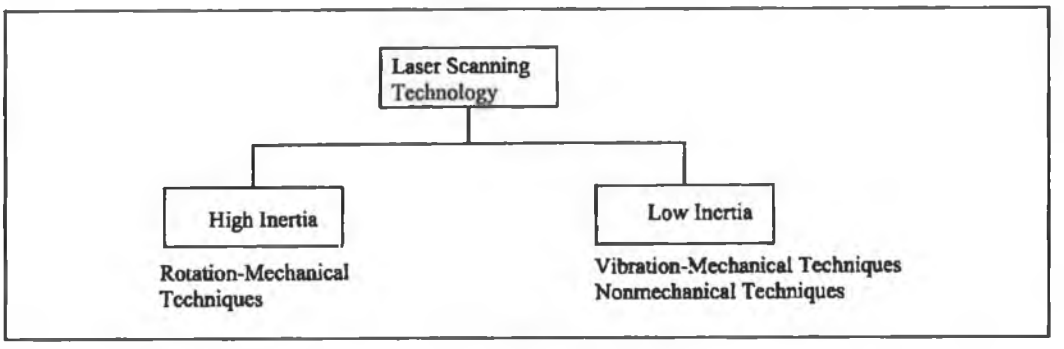

Figure 2.14: General classification of laser scanning technology [12].

Figure 2.15 illustrates the position of the scanner in relation to the objective lens. Three possible regions for the scanner are illustrated: preobjective (before the lens), objective (at the lens), or postobjective (after the lens). A group of rays from a reference (object) point P_0, which is transferred to the conjugate-image point P_i by means of scanning the ray group. The ray direction makes this illustration of active scanning, because the light source (laser) forms the fixed object point and the rays are directed through the scan regions. An objective lens converges the light beam at the focal point. The focal point moves along the surface to be scanned by the scanner. Point P_o is fixed, whereas P_i is displaced on the information surface. In passive scanning the ray directions are reversed, sustaining the reciprocal nature of conjugate imaging. That is, the reflected laser beam from each sampled point (P_i on the right) is addressed by the scanner for its optical transfer to a fixed detector (at P_o on the left) [11].

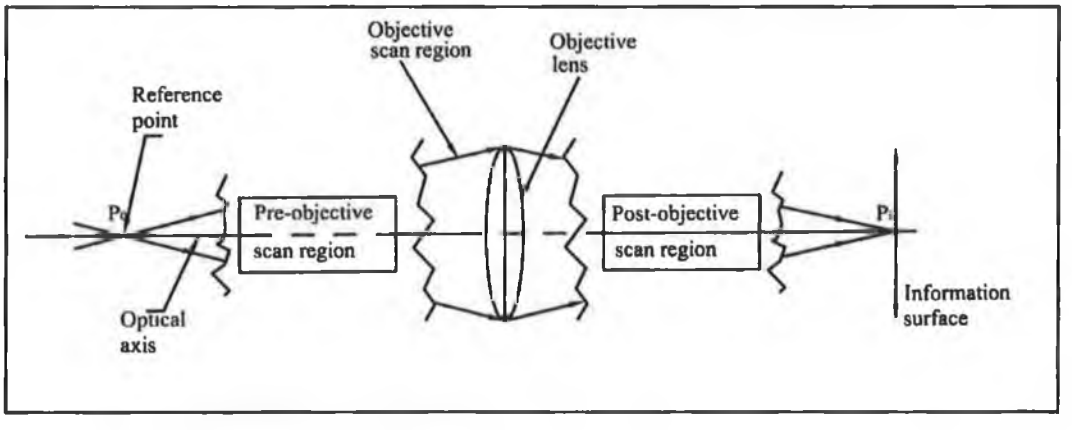

Figure 2.15: Classification of scanners with respect to the position of the objective lens [11].

The currently available laser beam scanners rely mainly on mechanical, electro-optic or acousto-optical phenomena. Hence, the classification can be made as:

a) Mechanical scanners.
b) Acousto-optical scanners.
c) Electro-optical scanners.

The first two are well-established methods while the third is being currently developed. The rest of this section is based on this latter classification.

2.2.2 Mechanical Deflectors

The simplest mechanical scanning systems avoid beam deflectors by allowing the part to move under a stationary beam [13]. This system was further investigated in the current work. More expensive systems incorporate a beam deflector into the laser scanning system. The basic concept of the mechanical deflectors is simple and straightforward. The laser beam is made to fall onto a continuously moving mirror, which directs it to the wanted location. All mechanical deflectors involve mechanical motion of some component. Mechanical deflectors consist of a mirror or prism that is moved in some manner so as to send the beam from one position to different position. A plane mirror is the basic optical element that forms the simplest of all mechanical scanning devices. It becomes a device when the mirror is mounted and capable of moving about an axis of rotation. The direction and position of the rotational axis with respect to the plane of the mirror and with respect to the direction of the incident light beam, are key factors in the operation of mechanical scanning device [14].

There are three methods used in mechanical deflection systems: rotating mirrors, galvanometers, and holographic deflectors. Galvanometer scanner is a simple motor in which the moving iron rotor is limited to angular displacement of about $\pm 15°$ from the neutral position [14]. Moving coil or moving iron mechanisms respond to the deflection controlling current and torsion returns them to the zero position. When an electrical current pulse is applied to the coil, it rotates the magnetic field. The mirror can be rotated to any position within its range simply by pulsing the electric current.

The galvo deflectors in the figure 2.16 works in random access way, i.e. The quantized deflection commands are aperiodic, sending the beam to the required address only when asked to and leaving them there for the required duration.

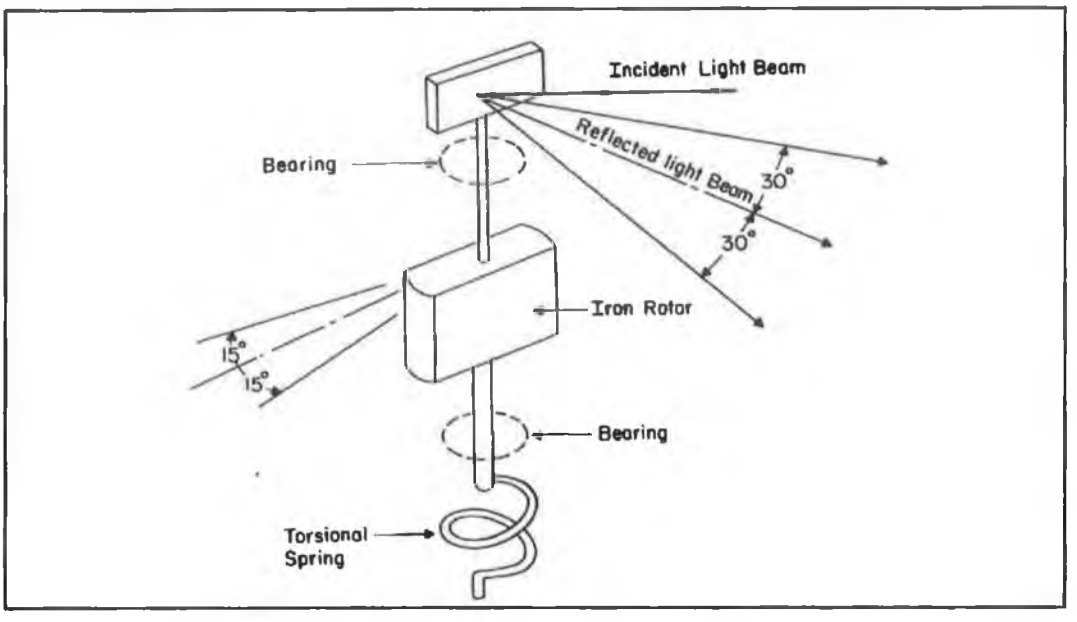

Figure 2.16:Basic component of a galvanometer scanner [14].

There are two distinct classes of galvanometer that exhibit different ranges of performance. These are,

- Broadband galvanometer, and
- Resonant galvanometer

Broadband galvanometer scanner can provide a linear ramp scan and it is possible to be held in a fixed position. Thus it can address any arbitrary chosen position just by applying a specified current pulse. Frequencies up to 300 Hz are possible with a resolution up to 2000 elements per scan. Resonant galvanometer follows a sinusoidal scanning function at a fixed resonant frequency. It is possible to scan a repetitive pattern at higher frequency.

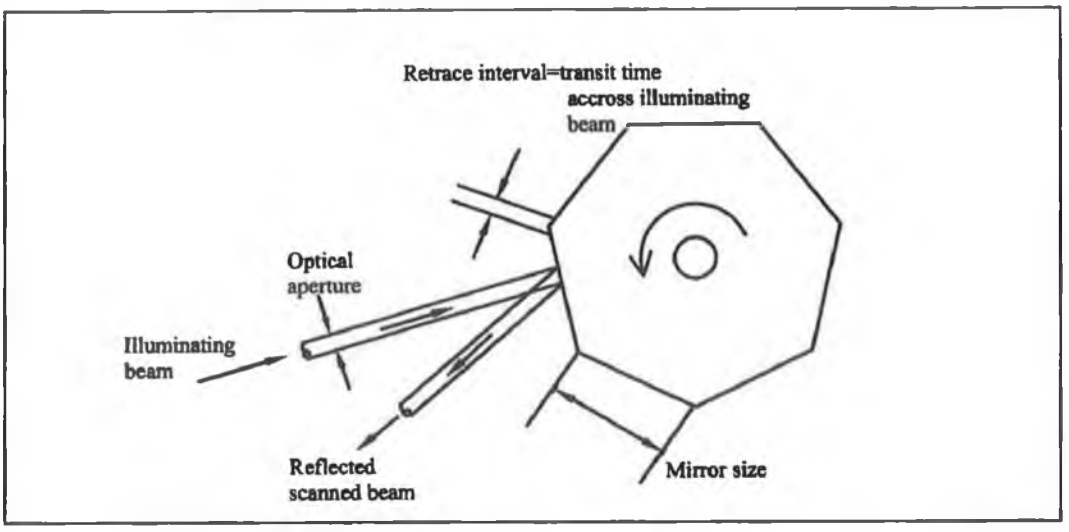

Figure 2.17: Partially illuminated polygon [12].

Rotating mirror deflectors often consists of a polygon-shaped mirror mounted on a fast-rotating shaft. The sides of the polygon are polished to a mirror finish. One of the most familiar rotating mirror techniques is illustrated in figure 2.17. A multifaceted polygon is illuminated with a single narrow pencil beam such that only a fraction of the mirror surface is exposed to the beam at any time. If the polygon has n sides, incident laser light reflected off each side is deflected through an angle of $\pm 360°/n$ from the normal. An angular displacement of the polygon through the angle θ imparts a 2θ angular displacement to the reflected pencil beam. This double speed scan continues until the corner of the polygon encounters the illuminating beam, whereupon the reflected beam is split into two: one part finishing the scan and the other part initiating the new scan. This period of split reflectance establishes the "retrace interval" and waits for some time to resume the next scan. However, this system is optically and mechanically inefficient since only a small fraction of the mirrored surface is actively engaged in reflecting the illuminating beam.

Holographic scanners create holographic images using similar principles to the operation of the rotating polygon method. Figure 2.18 shows a holographic scanner that takes the form of a disk, which is rotated about its axis. The deflector consists of multiple plane diffraction grating facets in a photo-emulsion on a glass substrate [15]. A transmission hologram is encoded on the rotating disk. The holographic gratings

encoded on different sectors of the disk represent the different facets of the rotating polygon. The incident laser beam is diffracted by the disk to form an aberration-free point image of the source used to fabricate the hologram. As the hologram rotates, the point image is scanned in a circle in the image plane.

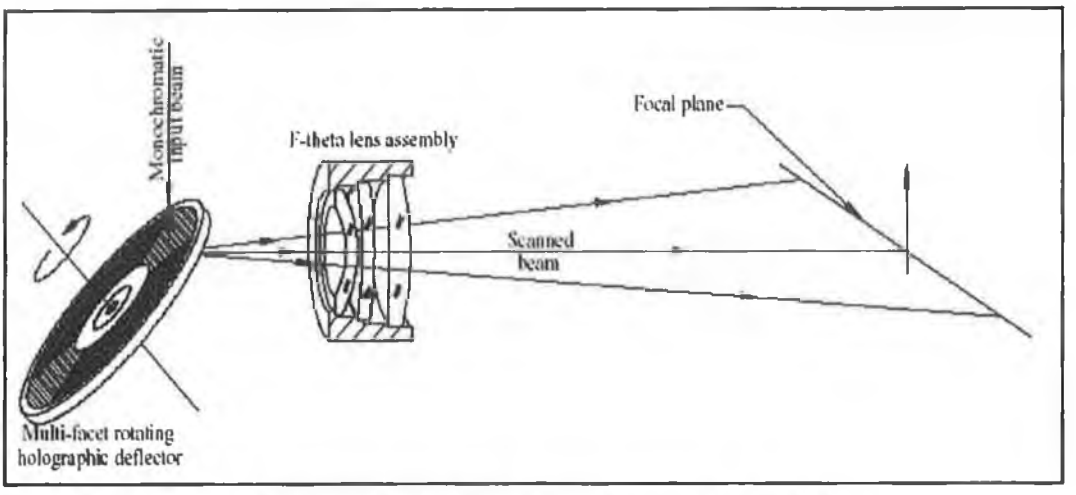

Figure 2.18: Typical holographic deflector-based scanner design [15]

One of the main advantages of mechanical scanners is that there is no interaction of light with the medium. Since the scanner has only a single surface, distortion of the beam because of imperfect medium quality can be avoided. A large number of resolvable spots or a large deflection angle is achievable in mechanical deflectors. Small loss of light in the deflected light beam and low driving power are other attributes of this type of scanner. However, since mechanical scanners involve physical motion of material, the scanning accuracy and speed are both lower than for nonmechanical deflectors. The inertia of the mass of the material limits the speed at which the light beam can be deflected.

2.2.3 Acousto-optic Deflectors

Solid state acousto-optic devices solve many problems in designing laser beam scanners [16]. Acousto-optic (AO) deflectors are based on the diffraction of light. Acousto-optic interaction provides a simple means to deflect an optical beam in a sequential or random access manner. As a simple solid state scanner, the acousto-optic deflector (AOD) eliminates certain inherent drawbacks of mechanical scanners due to moving parts such as facet errors and need for realignment. For applications

that require rapid random access time, the AOD offers a distinct advantage. They are used to deflect laser beams at different wavelengths in optical signal processing systems, spectrum analyzers, displays, and laser radar systems.

The acousto-optic effect occurs when a light beam passes through a material in which acoustic waves are also present. When a sound wave travels through a transparent material, it causes periodic variations of the index of refraction. Due to the series of compressions and rarefactions of the sound wave moving through the material, there is a spatial periodic density variations in the material corresponding to the compressions and rarefactions of the traveling acousto wave [17]. This effect leads to a sinusoidal variation of the index of refraction of the material. An acousto-optic deflector in principle is made of an optical crystal, such as tellurium dioxide (TeO_2), which is a piezoelectric material. Applying a high frequency voltage to this element generates acousto waves that move through the crystal [18]. It is known as a Bragg cell [2]. For acoustic waves of sufficiently high power, most of the light incident on the acousto-optic device will be diffracted and therefore, deflected from its incident direction. In an acousto-optic device, a light beam is deflected in much the same way that light is deflected by a diffraction grating. So the travelling ultrasonic wave establishes a thick diffraction grating in the interaction medium, with grating spacing equal to the ultrasonic wavelength. In a scanner the result is a linear scan as shown in the figure 2.19 [16]. Interaction between an acoustic wave and a light wave develops within the acousto-optic deflector such that the light wave is redirected through an angle, which is controlled by the frequency of the acoustic wave. In an acousto-optic deflector the diffraction grating is a crystal of a substantial thickness and the spatially variable optical parameter is the refractive index. The magnitude of the deflection is mainly dependent on the frequency [17]. This is defined by

$$\Delta\theta = \lambda\Delta f / V \qquad 2.8$$

Where V is the acoustic velocity within the optical medium, λ is the laser wavelength within the medium, and Δf is the bandwidth of the acoustic frequency. Since the deflection angle is proportional to the acoustic frequency and inversely proportional to the acoustic velocity, generation of relatively large scan angles requires that the

deflectors operate with a large acoustic-frequency bandwidth and a low acoustic velocity.

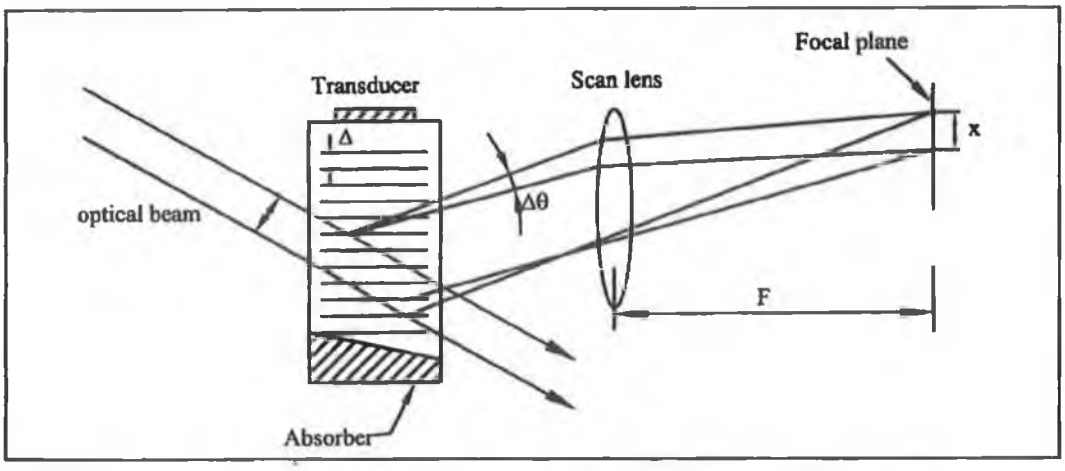

Figure 2.19: Principals of operation of an acousto-optic deflector [16].

Acousto-optic systems are best suited for that application in which the cost is moderate, sequential scanning is needed, and the required linear resolution is less than 1000 spots. Random access addressing can be achieved in times of approximately 10μ sec.

Acousto-optic scanners have been applied with good success in the flying spot laser microscope. The basic function of this device is to scan the focus of the laser beam over the field to be examined, detect the reflected or transmitted light, and display the magnified image on a television receiver. Fujita [19] developed 2-D scanner, which is capable of stepwise deflection of a laser beam with the resolution of the order of 0.01 microns in both the X and Y direction. X scanning is achieved using an acousto-optical device and Y scanning is done with a specially shaped prism coupled to a piezo translator (PZT). Maak et al. have developed a two-dimensional acousto-optic deflector [20]. The two dimensional acousto-optic deflector was designed for operation at 1064 nm in the 40-80 MHz acoustic frequency range. The acousto-optic configuration is chosen to obtain the highest possible deflection angle range. The deflector consists of two adjacent TeO_2 Bragg cells for diffraction of light in perpendicular directions.

2.2.4 Electro-optic Deflector

The linear electro-optic effect, the linear change of the refractive index of a material under the influence of an electric field, has found widespread application in beam deflection. The obvious advantage for the electro-optic deflector is that it can be treated as a capacitor, with the speed of operation dependent on the output characteristics of the drive circuitry. In the most advantageous situation nanosecond sweep rates can be obtained with pico-second resolution. Electro-optic deflectors use prisms of electro-optic crystals like lithium niobate. Voltages applied to the crystal change its refractive index, and hence the direction of propagation of the beam traveling through it. Electro-optic scanning exhibit very fast response and short access time but have relatively small numbers of resolvable spots.

In electro-optical materials, an applied electric field results in a change in optical birefringence (refractive index). Birefringence splits light passing through the material into two parts that travel at different speeds. When the light emerges from the other side of the material, its two parts will be recombined to form light having different polarization. The basic principle of the electro-optical deflector prism is shown in figure 2.20. The polarities of adjoining crystals are inverted in each adjoining crystal. When an electric field $E = V/d$, is present across deflector, the electro-optic effect induces a change in refractive index by an amount

$$\Delta n = \frac{1}{2} n^3 r \frac{V}{d} \qquad 2.9$$

and the deflecting angle of this prism is

$$\theta = \Delta n \frac{L}{l} \qquad 2.10$$

Where n is the linear refractive index of the medium, r is the electro-optic coefficient, V is the applied voltage, and d is the thickness of the wafer. When the diffraction-limited angle of the deflector is θ_R, the number of resolvable spots for the deflector is

$$N = \frac{\theta}{\theta_R} \qquad 2.11$$

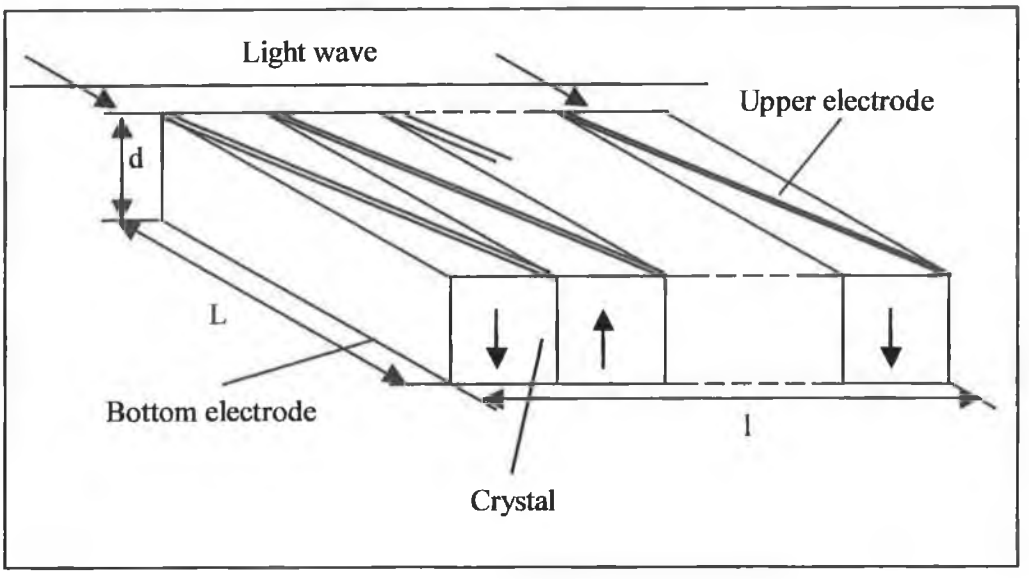

Figure 2.20: Electro-optic prism array.

A schematic diagram of a novel electro-optical laser beam deflector is shown in figure 2.21. The electro-optical deflector unit consists of a solid state integrated prism array of alternating domain inverted and non-inverted prisms, i.e. with alternating direction of the C-axis of the electro-optical crystal (Z-cut $LiNbO_3$ or $LiTaO_3$) [21]. The domain inversion in ferroelectric crystals is a process, which allows to locally rotate (at 180°) the domains in a suitably structured substrate. It can be performed at room temperature by applying to the crystal an electric voltage, which is higher than its coercive voltage, 24 kV/mm for $LiNbO_3$. The deflector chip consists of 2 segments: the prism-array part and the phase-shift part. The prisms are arranged in pairs with alternating domain polarization. By applying an electric field to a metal electrode common to all the prisms, refractive-index changes of alternating sign ($+\Delta n$ and $-\Delta n$, respectively) are induced in every prism pair. The laser beam is refracted at the interfaces between corresponding prisms and can be deflected stepwise. Continuous (analog) deflection is obtained by adapting the phases of the portions of the refracted beam with additional electrodes in front of the prism. The fabrication method of such deflectors which uses an array of prisms individually polished and attached to each other to form the refracting area [22]. The conventional fabrication method requires a

complicated and expensive technology. However, the use of domain inverted prisms for novel electro-optical deflectors have no such drawbacks. Because of well-defined interfaces between the prisms, superior beam quality can be expected. In a first step photolithographically well-defined domain-inverted regions are produced by domain inversion in $LiNbO_3$ (or in $LiTaO_3$). The inverted prisms are formed using a completely planer technology. To complete the deflection structure a common rectangular metal electrode is deposited in a second step, which produces a homogenous electric field.

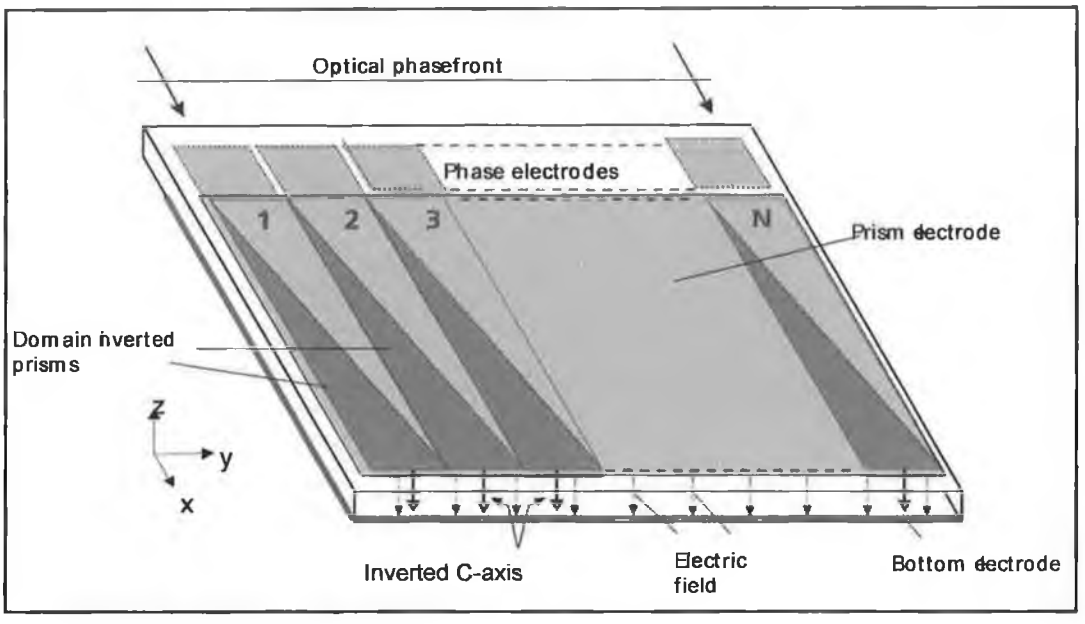

Figure 2.21: Schematic diagram of an electro-optic deflector array.

Elliot et al. [23] describe the theoretical analysis of the use of electrooptic beam deflectors as a streak camera [24]. Prism deflectors have been analyzed taking into account the transit time of the light pulse. Gahagan et al. [25] described integrated electro-optic lens and scanner fabricated on a single crystal of Z-cut $LiTaO_3$ as shown in the figure 2.21. Chen et al. [26] demonstrated the operation of electro-optic beam deflectors using domain reversal in planner waveguides fabricated on $LiTaO_3$ substrates. The deflection sensitivity of the device was measured to be about 6.7 mrad/kv. Ninomiya [22, 27] describes an elector-optic deflector with ultra-high resolving power and the method to remove the limit on the resolving power. Nelson [28] described the digital type electro-optic deflector that has high resolving power theoretically. Lotspeich [29] and Lee et al. [30] explained the analog type deflector.

Khayim et al [31] described an ultrafast electro-optic deflector which is able to include the lens effect. The lens effect can be described as the scanning of the laser beam spot to the direction of the propagation axis. This deflector utilizes the lens effect to make a light beam spot scan in two dimensions. A quadrupole electro-optic deflector has been developed by Friel et al. [32] using lithium-tantalite and lithium-niobate. This device is able to produce linear beam deflections of 6 mrad/kV and can produce short pulses (1.1 ns) using simple laser geometry. Thomas et al. [33] developed a cascaded phase array deflectors that allows high-resolution random access beam deflection. Optical phase array is typically composed of a multichannel array of electro-optic phase modulators. Thomas et al. demonstrated two 32-channel optical phases arrays that fabricated on lanthanum-modified lead zirconate titanate. The experimental device was able to address all 32 resolvable beam positions.

2.2.5 Other Types of Deflectors

There are other types of scanner apart from the scanners described above. They are described below.

Piezoelectric Deflectors

Beiser [12] described piezoelectric vibrational deflectors. Certain natural and processed crystals such as Rochelle salt display piezoelectric properties. Beiser describes two types of piezoelectric deflectors according to the deformation of the piezoelectric materials. They are:

- The shear mode piezoelectric deflector.
- The bending mode piezoelectric deflector.

Digital Light Deflector

Titus et al. [34] described digital light deflector (DLD) that can be used to deflect a laser beam with no moving part used. It is a liquid crystal beam steering device that deflects incident light by discrete amounts. Both inorganic crystals and liquid crystals

have been utilized in DLD devices. The basic structure of this device consists of two beam steering components as shown in the figure 2.22.

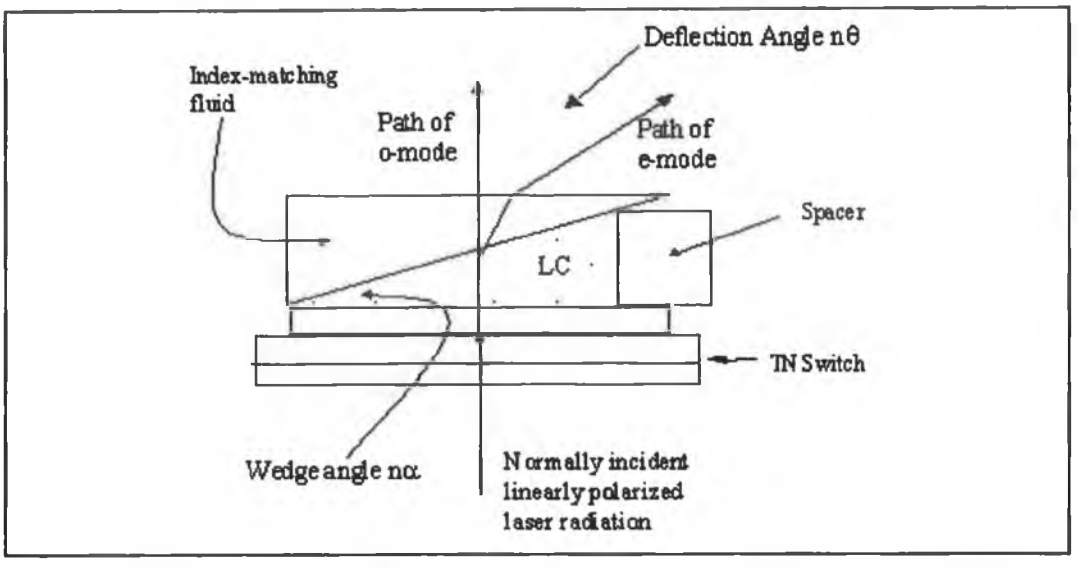

Figure 2.22: Basic beam steering switch for digital light deflector [34].

Each component consists of two optical elements, a passive deflector, which deflects incident light of two perpendicular linear polarization orientations by different angles, and an optical switch which selects the polarization state to be passed on to the deflector. The DLD consists of a passive birefringent deflecting wedge and a separate switching element. The birefringent element deflects the incident beam by two possible angles and the accompanying switch selects the incident linear Polarization state, thus deciding the output deflection. A compound device consisting of a stack of N stages, each with a different angular separation is capable of steering an incident beam to any of 2^N positions.

Liquid Crystal Deflector

Klaus et al. [35] described a liquid crystal beam deflector. The beam steering device consists of a novel array illuminator and a LC grating with multi-resistive electrodes generates a blazed phase profile [34]. Blazed phase grating is used to deviate light into the certain diffraction order. Laser beam passing through the active areas of the array is modulated spatially in a continuous and linear manner. Deflection of the beam

at an arbitrary angle can be achieved and the intensity of the deflected beam over the deflection range remains constant.

Fiber Optic Resonant Scanner (FORS)

Roberts et al. [36] demonstrated a hybrid pre-objective fiber optic resonant scanning (FORS) device which is able to generate 1D and 2D laser line scan. The scanning device is shown in the figure 2.23. Light from a semiconductor laser diode is coupled to a single mode optical fiber. The optical fiber is supported by a cantilever beam, which is free to resonate in one or two dimensions. Resonate modes of the cantilever are excited by a commercially available piezo-electric transducer. Both 1D and 2D-laser line are generated by using a lens to magnify the motion at the free end of the fiber optical waveguide.

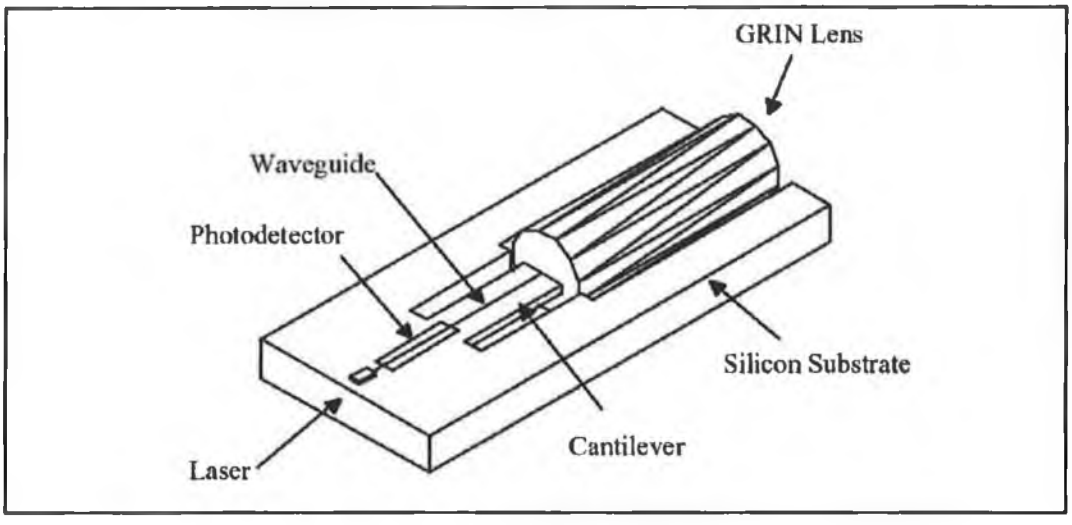

Figure 2.23: schematic diagram of integrated FORS device [36].

2.3 Surface Profile Detection Methods

Continuous progress in industrial automation and demand for increasing product quality require that the inspection system of the object should be fast and exact. Over the last century, a vast number of inspection systems have evolved. These methods follow two primary directions: passive and active sensing. Passive approach does not interact with the object, whereas active approaches make contact with the object or project some kind of energy onto it. Passive method is largely focused on computer

vision research where it is used to extract shape from one or more digitized images. Active range measurement techniques are described in the rest of this section. Figure 2.24 introduces taxonomy of active range measurement techniques [37]. Active sensing methods comprises of two approaches: contact and non-contact sensors.

2.3.1 Contact Sensing Method

Contact sensors are typically touch probes that consist of jointed arms or pulley-mounted tethers attached to a narrow pointer. The angles of the arms or the lengths of the tethers indicate the location of the pointer at all times. By touching the pointer to the surface of the object, a contact event is singled and the position of the pointer is recorded. Touch probes come in a wide range of accuracies as well as costs. Co-ordinate Measuring Machines (CMM's) are extremely precise and they are currently the standard tools for making precision shape measurements in industrial manufacturing. The main drawbacks of touch probes are:

- they are slow,
- they can be clumsy to manipulate,
- they usually require a human operator, and
- they must make contact with the surface, which may be undesirable for fragile objects.

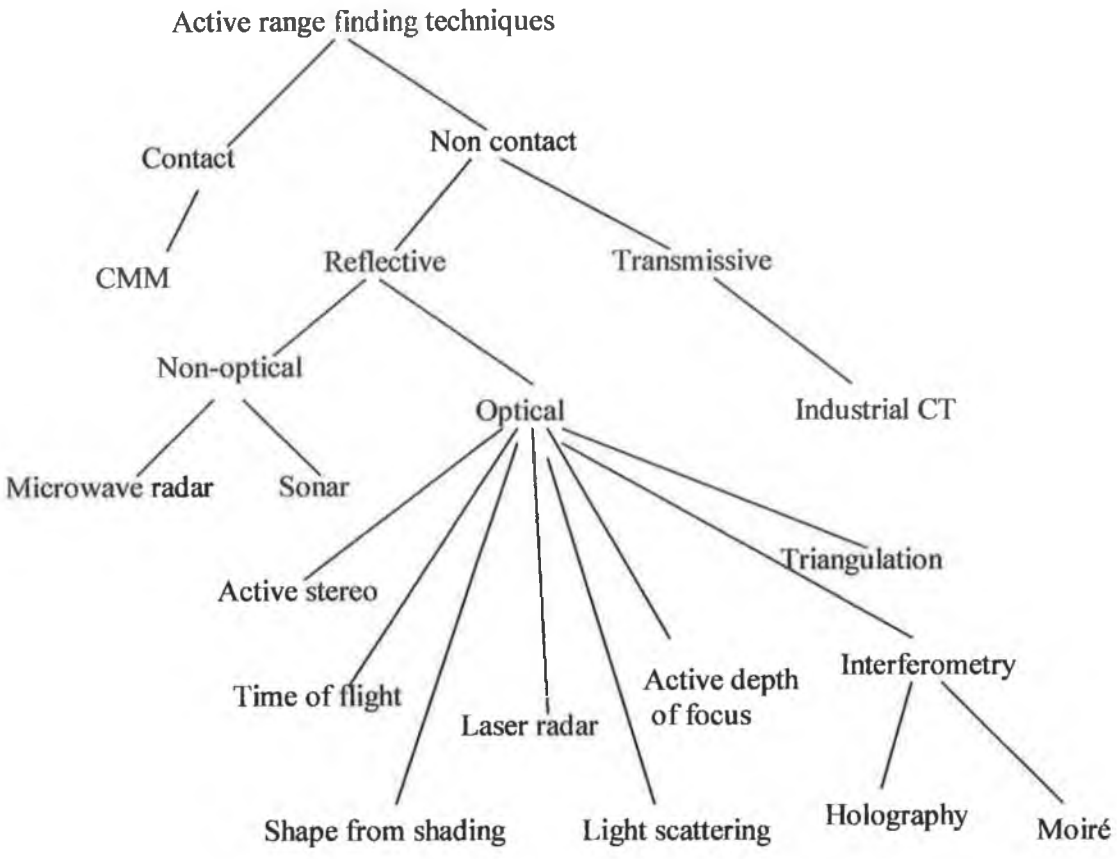

Figure 2.24: Taxonomy of active range acquisition methods [37].

2.3.2 Non-Contact Sensing Method

Active, non-contact methods generally operate by projecting energy waves onto an object followed by recording the transmitted or reflected energy. A powerful transmissive approach for shape capture is industrial computer tomography (CT).

Industrial CT entails bombarding an object with high energy x-rays and measuring the amount of radiation that passes through the object along various lines of sight. After back projection or Fourier projection slice reconstruction, the result is a high resolution volumetric description of the density of space in and around the object. This volume is suitable for direct visualization or surface reconstruction. The principle advantage of this method over reflective methods is that it is largely insensitive to the reflective properties of the surface, and it can capture the internal

cavities of an object that are not visible to the naked eye. The principal disadvantages of industrial CT scanners are:

- they are expensive,
- large variations in materials densities (e.g. wood glued to metal) can degrade accuracy, and
- they are potentially very hazardous due to the use of radioactive materials.

Active reflection methods for shape acquisition can be subdivide into two more categories: non-optical and optical reflection approaches. Non optical approaches include sonar and microwave radar, which typically measure distances to objects by measuring the time required for a pulse of sound or microwave energy to bounce back from an object. Microwaves are particularly suitable for large-scale 3-D measurements either by triangulation (e.g. global positioning system (GPS), determination of unknown point of a triangle by three sides) or directly by time-of-flight measurements. For industrial production automation, these techniques, in general, do not reach the required angular resolution due to diffraction. Sonar range sensors are typically inexpensive, but they are also not very accurate and do not have high acquisition speeds. Microwave radar is typically intended for use with long range remote sensing.

Optical reflection approach plays an important role in range finding. Fast and non-contact optical form measurements are of significant importance in industrial production, including inspection on tolerances and completeness, robot vision in automatic assembly, surface inspection, and reverse engineering [38]. Three-dimensional optical form measurements deliver the absolute 3-D geometry of objects that are largely independent of the objects surface reflectivity, the distance of the objects from the sensor, and illumination conditions. In optical methods, light is projected onto an object in a structured manner, and by measuring the reflections from the object, shape of the object can be determined. In contrast to passive and non-optical methods, many active optical rangefinders can rapidly acquire dense, highly accurate range samplings. In addition they are safer and less expensive than industrial CT, with the limitation that they can only acquire the optically visible portions of the

surface. Optical methods include imaging radar, interferometry, active depth-of-defocus, active stereo, and triangulation.

2.3.2.1 Light Scattering Method.

Light scattering from a surface can be used to measure the properties of the rough surface to determine roughness and detect defects [39-40]. Light is focused onto the target surface at some pre-set angle. This light is separated into two components by the nature of the surface; the specular portion and the scattered portion. The scattered portion is collected using an integrating sphere, which effectively guides the scattered light to a conveniently placed photo-diode where the total scattered light intensity is measured.

2.3.2.2 Laser Radar

Laser radar is capable of providing range information over a two-dimensional field of view. A laser radar system determines the distance of an object by transmitting amplitude modulated laser beam towards the object and then measuring the phase shift of the reflected beam with respect to the outgoing laser beam [41-42]. Laser radar is able to produce range image of the object at a high data rate and is capable of performing continuous measurements. However, range image is often corrupted by noise, and contains an appreciable number of erroneous reading [42]. For large objects, a variety of imaging radars has been demonstrated to give excellent results. For smaller objects, on the order of one meter in size, attaining 1 part per 1000 accuracy with time-of-flight radar requires very high speed timing circuitry, because the time differences to be detected are in femtosecond (10^{-12}) range.

2.3.2.3 Time of Flight

The pulsed time of flight (TOF) [43-46] is a laser range finding method for measuring distance and has been incorporated into many distance measurement applications. A basic device consists of a pulsed laser transmitter, a receiver channel for start and stop pulses, and a time interval measurement unit. The distance camera to object or the depth, z, can be determined by sending a relatively short impulse of light on a

reflective surface and measuring the time, say τ, it takes to travel the whole distance [46].

$$z = c\frac{\tau}{2} \qquad 2.12$$

Where c is the speed of light. Time-of-flight techniques usually are utilized in long range distance (>10m)

2.3.2.4 Optical Interferometry

In optical interferometry shape measurement systems, two coherent optical beams interfere with each other to generate an interferometry fringe carrying shape information. Then the shaped information is decoded by using an image processing procedure. For general interferometers, the sensitivity of the interferometry pattern is about the same level with the wavelength of the lighting. So, the resolution is from sub-microns to nano-meters. A large number of different interferometric depths measuring systems with different measuring properties are currently available. The moiré interferometry [46] involves the projection of coarse, spatially varying light patterns onto the object. Moiré methods can have phase discrimination problems when the surface does not exhibit smooth shape variations. This difficulty usually places a limit on the maximum slope the surface can have to avoid ranging errors. Another interferometric methods, Holographic interferometry enables deformation of 3-D objects caused, for example, by thermal or mechanical stress to be measured in the nanometer range. Speckle interferometry utilizes the interference pattern due to the roughness of the surface in optical metrology for exact deformation measurements. Speckles are generated when coherent light is reflected from a rough surface. The reflected wavefronts interfere with each other on the detector surface and generate a speckle pattern that is characteristic for the surface roughness elements. If an additional reference beam generates a second speckle pattern, this is coherently superimposed to the first one and produces a speckle interferogram.

2.3.2.5 Depth From Focus/Defocus

Depth of focus is a problem of reconstructing the depth of the scene by actively changing the optics of the camera until the point of interest is in focus [47]. Active depth of focus operates on the principal that the image of an object is blurred by an amount proportional to the distance between points on the object and the in-focus object plane. The amount of blur varies across the image plane in relation to the depths of the imaged points. This method has evolved as both passive and an active sensing strategy. In the passive case, variations in surface reflectance (also called surface texture) are used to determine the amount of blurring. Thus, the object must have surface texture covering the whole surface in order to extract shape. Further the quality of shape extraction depends on the sharpness of surface texture. Active methods avoid these limitations by projecting a pattern of light (e.g. a checkered board grid) onto the object. Most prior work in active depth from focus has yielded moderate accuracy. Depth of defocus technique is used to reconstruct the depth map of a scene from a set of images collected from the same camera but with different optical settings.

2.3.2.6 Shape From Shading

Shape-from-shading determines the structure of the object surface from images observed through a camera, under differing illumination conditions by using its reflection properties [48]. 3- D information about a surface is produced by analyzing the image irradiance and the known position of the camera and the light sources. A set of surface normal of the surface elements is generated, from which a height field can be generated. More detailed analysis of the action of the lighting such as shadows, inter-reflections and highlights can be used to improve the overall accuracy of the result. The main advantage of shape-from-shading, is the simplicity of the equipment (a CCD camera and a few light sources), which provides an inexpensive set-up.

2.3.2.7 Active Stereo

Active stereo or photogrammetry uses two or more cameras to observe features on an object. If the same feature is observed by two cameras, then two lines of sight passing

through the feature point on each camera's image plane will intersect at a point on the object. Due to the perspective projection, which occurs in a camera, a point in an image corresponds to a line of points (vector) in 3D-space [49]. By taking the same point in a number of images, taken from known positions and intersecting their vectors, the point in 3D is found. One of the problems with photogrammetry is to find the correspondence between the different images, i.e. which points in this image correspond to points in the other images. As in the depth from defocus method, this approach has been explored as both a passive and an active sensing strategy. The active method operates by projecting light onto the object to avoid difficulties in discerning surface texture and in the passive method utilizes the ambient light as source of illumination onto the object [50].

2.3.2.8 Triangulation

Triangulation [51-69] is the most widely used technique for optical form measurements. Triangulation is a commonly used technique for determining spatial relations. Laser triangulation devices are commonly used for surface geometry inspection. Generally a simple structured light pattern as a dot or a line is first projected onto the surface; the light scattered is then collected by a linear or bi-directional array of sensors. Details of the optical triangulation system will be described in the next chapter.

Chapter Three

3 Operation Principle of the Surface Inspection System

3.1 Introduction

This chapter illustrates the basic principle operation of the laser based surface inspection system. The system was developed using the active optical triangulation method. Firstly the general theory of optical triangulation principle is discussed, this includes the basic principle, different triangulation configurations and the advantages and disadvantages of this principle. After this, the measurement principle for the present system is analyzed in detail. Finally, the theory regarding the measurement of the laser beam spot position on the imaging sensor is discussed.

3.2 Optical Triangulation

Triangulation is the most widely used technique for form measurements. It is one of the most common methods for acquiring range data. This method has been used in a variety of applications as its speed and accuracy has increased with the development of imaging sensors such as CCD's and lateral effect photodetectors. Because of its simplicity and robustness, optical triangulation has been recognized as the most common method of commercial three-dimensional sensing [66]. Five distinctly different triangulation methods exist:

1. Active triangulation with structured illumination,
2. Focus techniques,
3. Passive triangulation techniques on the basis of digital photogrammetry and stereoscopy,
4. Theodolite measuring systems, and
5. Shape from shading.

Here discussion will be limited to the active triangulation method.

3.2.1 Active Triangulation

An optical triangulation technique is illustrated by the simplified diagram shown in figure 3.1. A laser beam projects a spot of light onto a diffuse surface of an object and a lens collects part of the light scattered from this surface. If the object is displaced from its original position, the center of the image spot will also be displaced from its original position. Therefore, the displacement of the object can be determined by measuring the displacement of this spot center on the position sensor. By using a laser beam to scan the object, the object's shape can be determined with knowledge of the projection angle of this beam and the spot displacement on the position sensor.

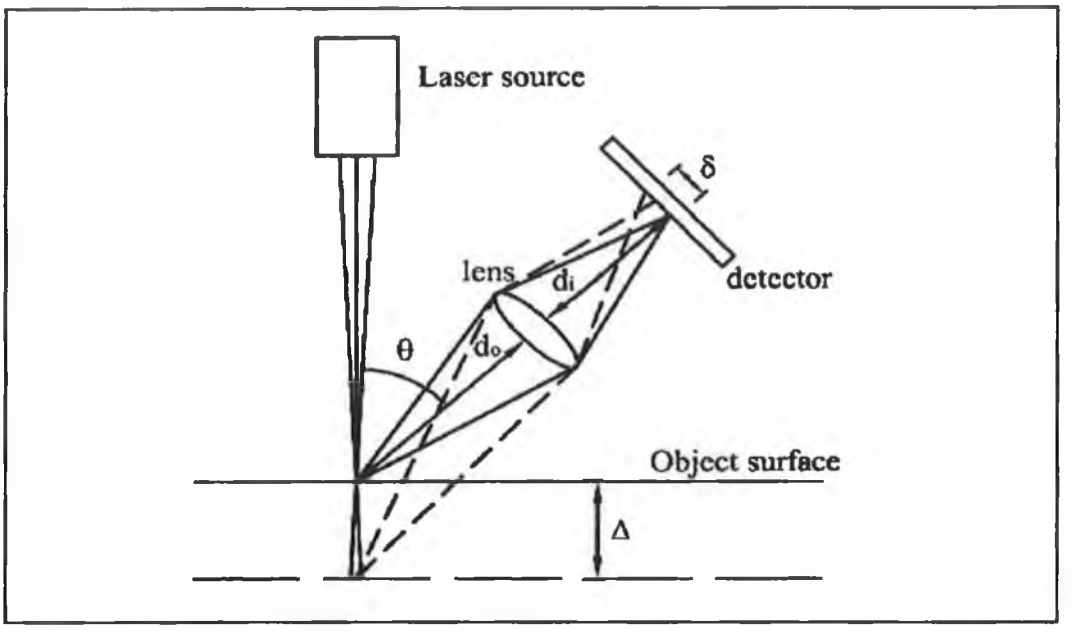

Figure 3.1: Optical triangulation technique [54].

In the figure the triangulation device is built with the detector surface perpendicular to the axis of the converging lens. Assuming the displacement, Δ, to be small and the angle, θ, to be constant as the surface is displaced, the image displacement, δ, in relation to Δ is

$$\delta = \Delta m \sin\theta \qquad 3.1$$

where $m = d_i / d_o$ is the magnification factor (see figure 3.1). Over a small range the system is linear and in some circumstances it may be useful to use it over that range, but often a larger range is required. In this case the configuration has the additional problem of requiring a large depth of field to keep the image in focus. Depth of field is defined as the distance over which the focused laser spot has a nearly constant diameter and thus constant irradiance. The triangulation system illustrated in figure 3.1 is not designed to keep the image in focus as it is displaced on the detector [6]. With an extended range, the camera will be out of focus at certain part of the range, or a large depth of focus will be required [51]. To keep the image in focus, the detector must be oriented at an angle, ϕ, to the lens axis as shown in the figure 3.2. Ji et al [54] derived a new relationship for the measured surface displacement.

$$\delta = \frac{d_i \sin\theta\Delta}{\Delta\sin(\theta+\phi)+d_o\sin\phi} \qquad 3.2$$

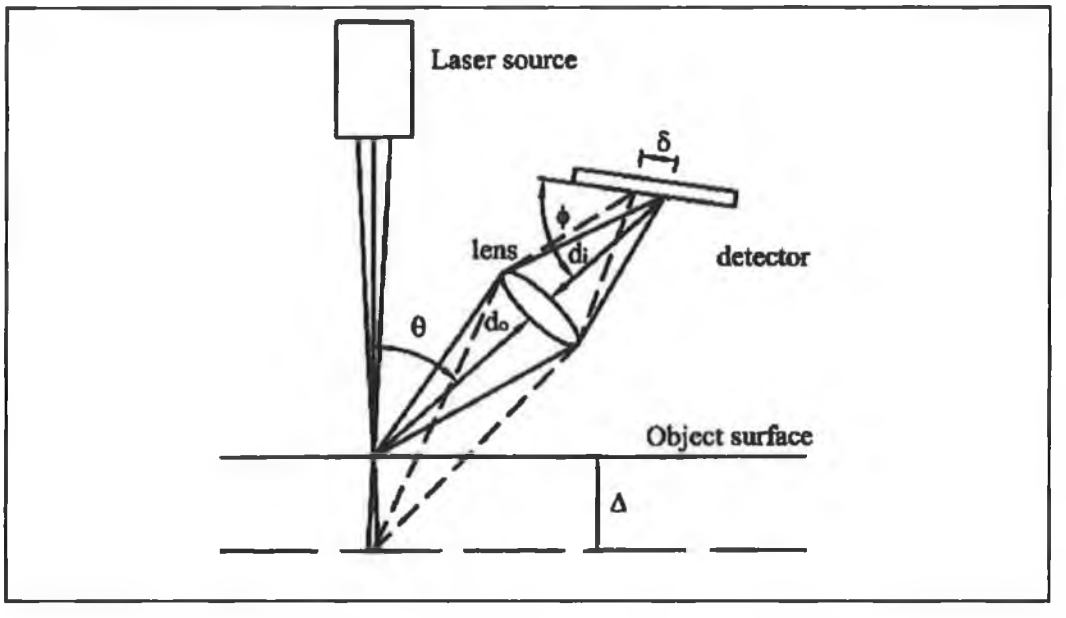

Figure 3.2: Triangulation technique with detector at an angle relative to the lens axis [54].

3.2.2 Triangulation Configuration

The variety of optical triangulation configurations differs primarily in the structure of the illuminant, the dimensionality of the sensor and scanning method. Different types of scanning methods have been discussed in chapter two.

The structure of the illuminant can take a variety of forms. In active triangulation, two types of illumination techniques can be used:

- Light beam technique, and
- Lightsheet technique.

In light beam technique a light beam forms a spot on a surface and provides a single range value. With lightsheet technique or 2-D laser triangulation, a laser beam is expanded via cylindrical lenses to a light plane. Figure 3.3 shows schematically a lightsheet triangulation technique and height profile generated on the array detector The cross section of the lightsheet and of a 3-D object forms a light strip (the height profile) that is imaged onto a 2-D detector. It limits scanning in one dimension.

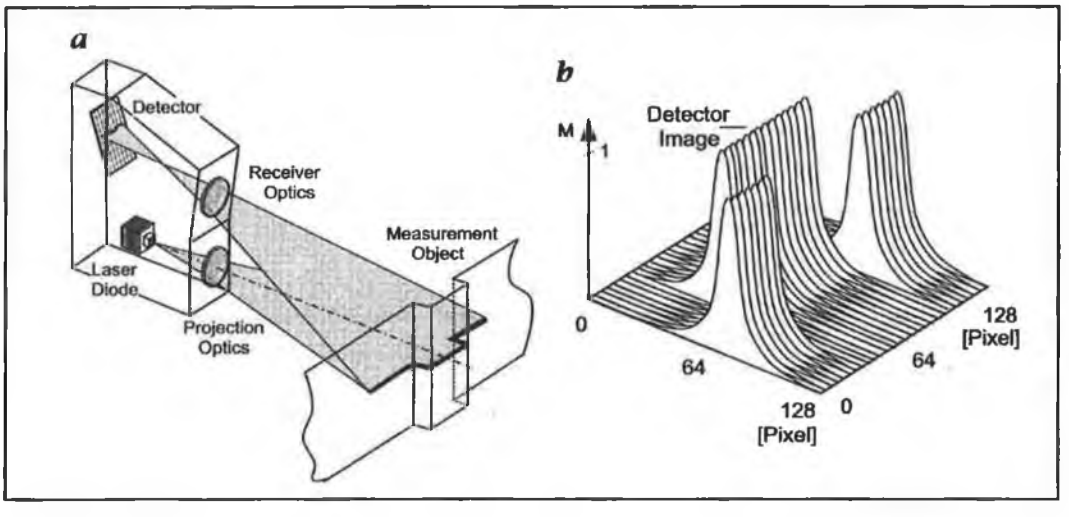

Figure 3.3: Lightsheet triangulation technique (a) schematic diagram (b) detector image [38].

Apart from the above two techniques researchers have also tried projecting multiple spots or multiple stripes onto an object for more parallelized shape acquisition.

Sensors for optical triangulation can be of different types. Sensor types depend upon the structure of illuminants. For single light beam producing laser, photodiodes or line sensors such as lateral effect photodetectors and linear array charge coupled device (CCD) are sufficient. Two-dimensional sensors can also be used for single beam laser. Two-dimensional sensors are mostly necessary for light strip and multi point systems. CCD and complementary metal oxide semiconductor (CMOS) camera fall into this category. Principles of the CCD and CMOS cameras are discussed in detail in chapter four.

3.2.3 Resolution of the Triangulation System

The resolution of the triangulation system depends upon a variety of parameters, including the laser beam spot size and the resolution of the micrometer stages. Some of the fundamental parameters of any imaging system include the field of view (FOV), working distance, depth of field (DOF) and the sensor size. FOV is the viewable area of the object under inspection. The maximum achievable resolution is the trade off between all of these parameters the most important of which are described below:

Spot Size

The projected spot size should be small to achieve a higher longitudinal resolution on the object. The spot size should not be larger than the feature to be measured. The image on the detector should also not be too large, for a better localization on the detector, i.e., for better depth resolution. A small spot size and image size requires high aperture projection. There is a limit in the laser beam spot size. The smallest achievable diameter is the diffracted limited spot. According to Raleigh's criterion [68], the minimum resolvable lateral shift of the laser beam spot in the scanning direction is half of its width.

Angle of Triangulation

Triangulation angle plays an important role in longitudinal resolution. But there must be a trade off between high longitudinal resolution and shadow effects [66]. The

triangulation technique shows severe shadow effect problems associated with the requirement of a large triangulation angle in order to get a reasonable longitudinal resolution. In laser triangulation, there are two shadow effects; (a) points on the surface that the projection beam cannot reach (shown by the shaded area on the left-hand side in figure 3.4); and (b) points on the surface that the sensor cannot detect (the shaded area on the right hand side). So triangulation angle should be as small as possible in order to avoid this. Use of the synchronized scanning principal [55-56] can help reducing the shadow effect while maintaining the desired resolution.

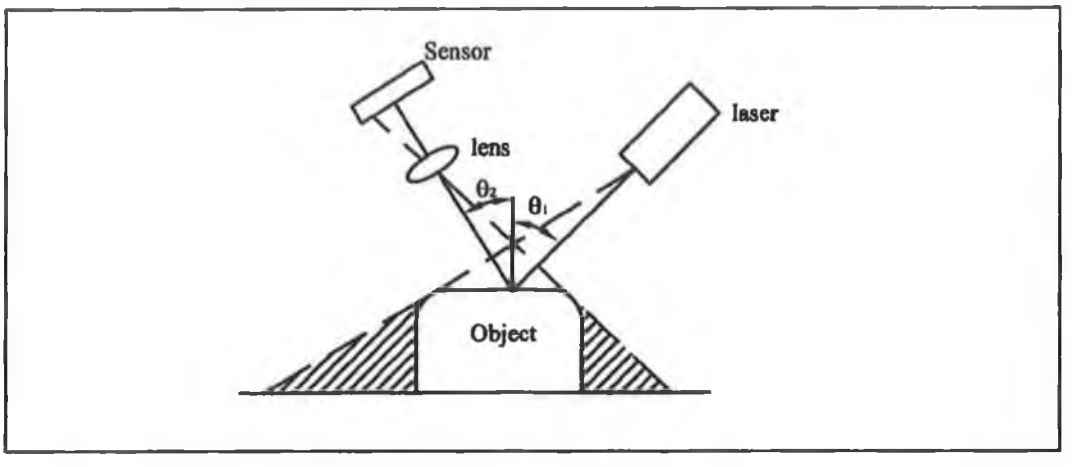

Figure 3.4: Shadow effects in laser triangulation system [66].

Speckle Noise

The uncertainty in distance measurement of optical triangulation sensors and other coherent sensors is limited by speckle noise [70-71]. Figure 3.5 shows speckle noise. Speckle arises when coherent laser illumination bounces off of a surface that is rough compared to the laser beam wavelength. The surface roughness introduces random variations in optical path lengths, causing a random interference pattern throughout space and at the sensor.

In triangulation systems, laser speckle affects the localization of the spot image and therefore some uncertainty is introduced into the measurement of the macroscopic distance. This uncertainty is a function of wavelength, observation aperture and speckle contrast in the spot image. Dorsch et al [63] calculated the depth resolution, δ_x, due to speckle:

$$\delta_z = \frac{\lambda}{2\pi \sin\theta \sin u_i} \qquad 3.3$$

where $\sin u_i$ and θ (see figure 3.1) are the aperture of the detector optics and the triangulation angle respectively and λ is the wavelength of the laser beam.

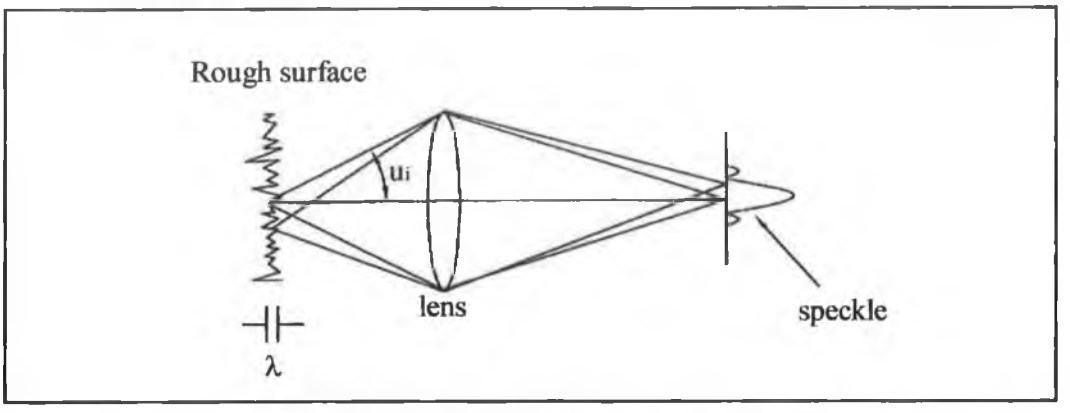

Figure 3.5: Laser speckle noise on an imaging system due to the surface roughness [96].

Depth resolution of the triangulation system depends on the angle between the illumination direction and the observation direction. With a large triangulation angle, a small depth variation is transformed into large lateral shift of the profile. So the depth resolution δz of the whole system is

$$\delta z = \frac{\delta x_c}{\tan\theta} \qquad 3.4$$

For a high depth resolution the sensor system must resolve the small shift, δx_c, of the profile. This small shift depends on the depth of field of the observing lens and on the resolution of the detector [68]. The resolution of a discrete detector array can be much better than that given by the pixel spacing. This is possible by using interpolation techniques.

3.2.4 Advantages and Disadvantages of Triangulation System

In terms of measuring range and measuring accuracy, optical triangulation systems suit industrial metrology. Triangulation measuring systems offer data acquisition rates of up to 10000 measurements per second with a significant accuracy [51]. When such a system is rotated about a central axis, it is possible to measure structures which are relatively large with reasonable speed and accuracy. It also serves as a probe for co-ordinate measuring machines (CMM) to replace customary contact probe and as a probe for dynamic inspection.

A disadvantage of the use of triangulation systems is that the measurement does not take place coaxial with the light source, leading to problems of shading and in the physical size of the measuring instrument. If the distance between the sensor and the light probe is reduced to minimize these problems then, the non-linearity in the triangulation geometry becomes a serious limitation. The light source used has to maintain a high signal to noise ratio at the detector compared to the ambient light reflection in the area of interest, and this can lead to problems of eye safety. Resolution of the triangulation system is limited up to certain extent, so is suitable for bounded situations where it is known that all objects of interest will fall within the range of the measuring equipment. The lens system and laser launching system may present problems in dirty environments with ensuring clear optical surfaces

3.3 Measurement Principle of the Inspection System

The basic block diagram of the sensor system developed in this work is shown in the figure 3.6. The sensor ascertains the presence of defects on the surface under test with respect to a reference surface. Defects on a surface could be of two types, lack of material or excess material. This sensor could be used to determine the defects of both types. The system can also produce the surface topography. By measuring the co-ordinates of the points on the surface, it is possible to map the whole surface.

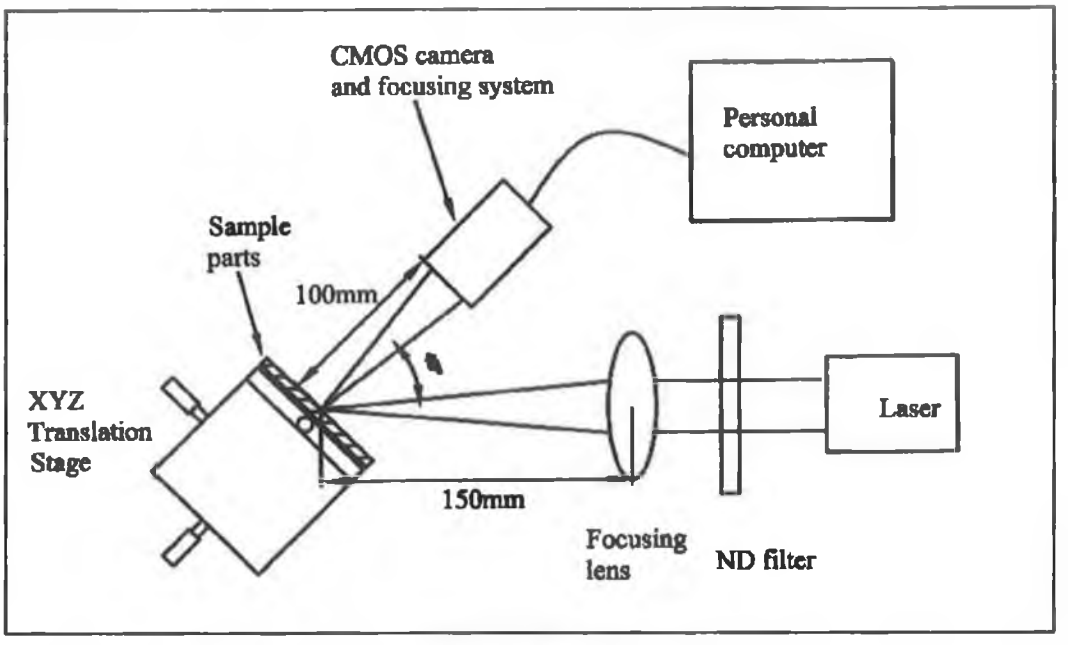

Figure 3.6: Block diagram of the surface defect inspection system.

A laser beam with a diffraction-limited spot from the laser diode was obliquely incident on the surface. It creates a bright spot on the surface by diffuse reflection. In this system the light beam was stationary and the surface was moved using an XYZ translation stage. The bright spot on the surface was imaged onto a Fuga 15 camera sensor and the image was stored for further processing. Processing of the acquired image provided information about the position of the laser beam spot on the surface, and the horizontal spot shift on the reference level was then computed. The distance between the surface and the reference level at each sampled point is then easily calculated [52-53].

Figure 3.7 illustrates the method used to determine the surface defects. Intersection of the laser beam with the surface creates a bright spot at position X_n, which is the real sampled surface point. P_n corresponds to the position on the surface when the laser beam intersects with the reference level. The lateral shift of the bright spot with respect to the reference level is δ_n. So the normal distance between the actual surface and the reference level is proportional to the lateral shift δ_n. The distance is described by the equation:

$$Z_n = \delta_n \cot \eta \qquad 3.5$$

where η is the angle of incidence of the laser beam

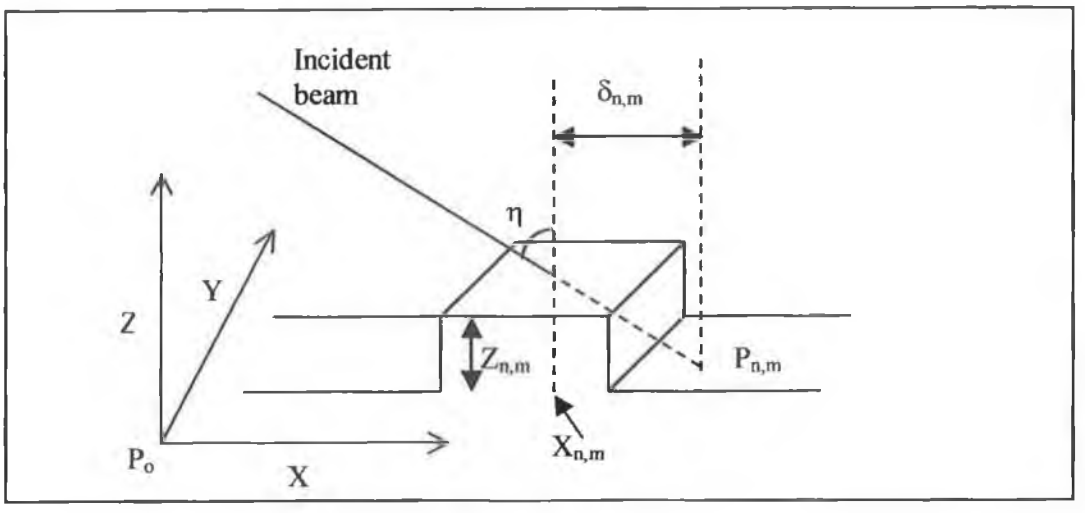

Figure 3.7: Basic principle. Intersection of the laser beam with the surface with defect causes a shift of the bright spot with respect to reference level [52-53].

Since in this system the laser beam was stationary, the surface was swept laterally by equal increments in the X-direction, Δ. The lateral shift of the bright spot on the surface was observed by the sensor. Only the lateral shift of the bright spot, δ_n, was measured and thus was processed later for the surface reconstruction. Figure 3.8 shows the lateral shift of the laser beam spot on the sensor. Lateral shift of the beam spot on the surface is thus determined by knowing the resolution of the sensor.

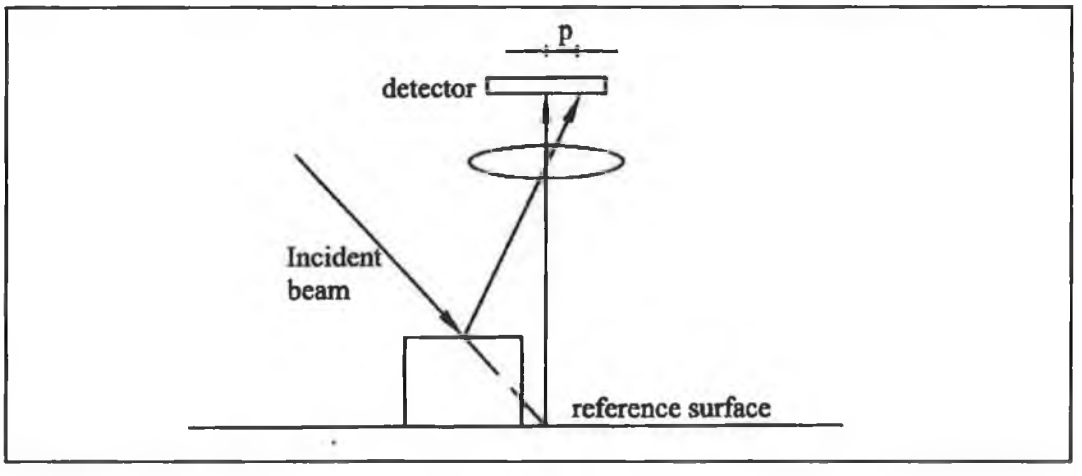

Figure 3.8. Lateral shift of the beam spot on the sensor in triangulation system with the shift of beam on the surface.

The resolution of the detector is the smallest resolvable increment of size or positional change in the object plane that can be fully detected from one pixel to the next. It is determined by dividing the field of view by the number of pixel elements in that direction. It is expressed as the amount of spacing in the object that corresponds to one pixel. For a 2-D sensor with NxN numbers of pixels and with the field of view, Δx, lateral resolution of the sensor is (see figure 3.9)

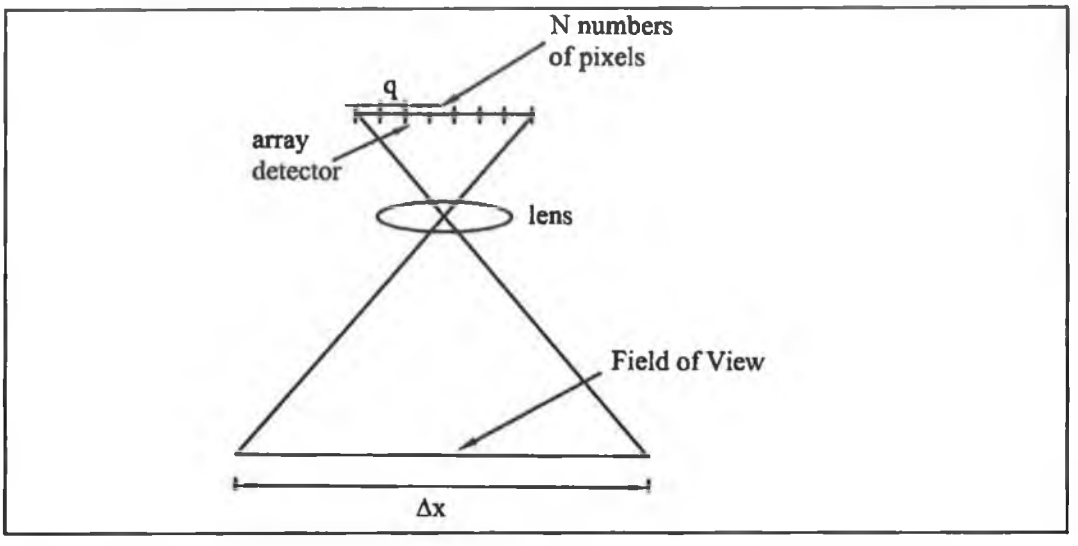

Figure 3.9: Measuring the field of view and the resolution of the array detector.

$$\delta_x = \Delta x / N \qquad 3.6$$

δ_x is defined as micrometer per pixel (μm/pixel). If q is the physical dimension of each pixel then magnification of the camera optical system is

$$M = q / \delta_x \qquad 3.7$$

from the figure 3.8 if p is the lateral shift of the beam on the detector in terms of number of pixels, then lateral shift of the beam spot on the surface is found as,

$$\delta_n = p\delta_x \qquad 3.8$$

Therefore,

$$\delta_n = p\left(q/M\right) \qquad 3.9$$

If P_o is the position at origin in the co-ordinate system of the surface (see figure 3.7) and n the increment number in the X, then the following equations can be obtained:

$P_o = n\Delta$, Known as the sampling position. 3.10

$X_n = n\Delta - \delta_n$, which is the X co-ordinate of the n^{th} real surface point. 3.11

Using equations 3.5 and 3.9, surface height at point X_n is found

$$Z_n = p\left(q/M\right)\cot\eta \qquad 3.12$$

In order to obtain a 3-D map of the surface, several profiles separated by a distance Φ in the Y-direction were taken. Thus the co-ordinates of the inspected surface points are

$$X_{n,m} = n\Delta - \delta_{n,m} \qquad 3.13$$

where m represents the number of increments in Y-direction.

$$Y_{n,m} = m\Phi \qquad 3.14$$

$$Z_{n,m} = \delta_{n,m}\cot\eta \qquad 3.15$$

3.3.1 Calibration

In order to measure the vertical displacement of the surface, Z_n, the system was calibrated. From equation 3.12 it is seen that the distance is proportional to the lateral shift of the beam spot. If the factor $\left(q/M\right)\cot\eta$ is determined, it is possible to get the

distance Z_n from equation 3.12. This factor is defined as the conversion factor for that system. The Conversion factor is dependent on the incidence angle, on the magnification of the reception optical system and the sensor dimension. The calibration for a given incidence angle is performed on a plane reference surface. The reference surface was moved along toward or away from the detector by a precise displacement. During calibration, for each vertical displacements of the reference surface, lateral shift of the bright spot was measured. Registrations of the lateral shift of the bright spot for each vertical displacement of surface yielded a linear trend between them. The linear fit of this trend determines the conversion factor of the system.

3.4 Determination of the Image Spot Location

In optical triangulation systems laser beam spot position on the target surface must be determined with great accuracy. The image on the array detectors provides the position of the spot on the surface to be scanned. Typically, a laser beam spot image has an approximately Gaussian shaped intensity distribution. This intensity distribution is influenced by the background, the distance of the target from the array detector camera, and the angle of inclination of the target to the camera. Variations influence the accuracy with which the detected image can be located.

Output of the pixelized array detector is composed of discrete voltages representing the amount of light on each element of light on each element of the array detector. A number of algorithms have been developed to compute the centroid of the laser beam image spot [72-77]. Five algorithms were described for determining the location of a laser strip in the images with subpixel accuracy, obtained by fitting a 1-D curve to a few pixels around the maximum of the strip cross-section, which should in theory be a gaussian distribution. The five-subpixel algorithms are the following

Gaussian approximation
Center of mass.
Linear interpolation.
Parabolic estimator.
Blais and Rioux detectors [75].

West et al. [72] investigated an algorithm to determine the centroid of the spot image where the intensity values are squared. This has the effect of giving more weight to the higher intensity levels which, are more precisely measured and, in a real image, less affected by background intensity variations. This centroid could not be expected to be correct when a small image covering a few pixels is used, because under these circumstances the calculated center will be incorrectly biased toward the highest intensity level, rather than to the center of a group of high intensity levels. The centroid co-ordinates are given by:

$$X = \frac{\sum_{j=1}^{n}\sum_{i=1}^{m} j.I^2_{ij}}{\sum_{j=1}^{n}\sum_{i=1}^{m} I^2_{ij}} \quad \text{and} \quad Y = \frac{\sum_{j=1}^{n}\sum_{i=1}^{m} i.I^2_{ij}}{\sum_{j=1}^{n}\sum_{i=1}^{m} I^2_{ij}} \qquad 3.16$$

A crucial component of accurate target co-ordinate determination is the determination of the center of the spot image to sub-pixel accuracy. One of the most common and intuitively acceptable definitions of the center of a target image is the position of its centroid. In order to determine the centroid of the image of the laser beam spot following equations were used in this work. In the simplest form, the position of the spot is determined by performing a weighted centroid on the array data of intensity value. The position of the centroid can be defined by co-ordinates relative to an arbitrary origin and arbitrary axis, but for convenience an origin and orthogonal axes are taken to coincide with a corner and the edges of the two dimensional array of pixels.

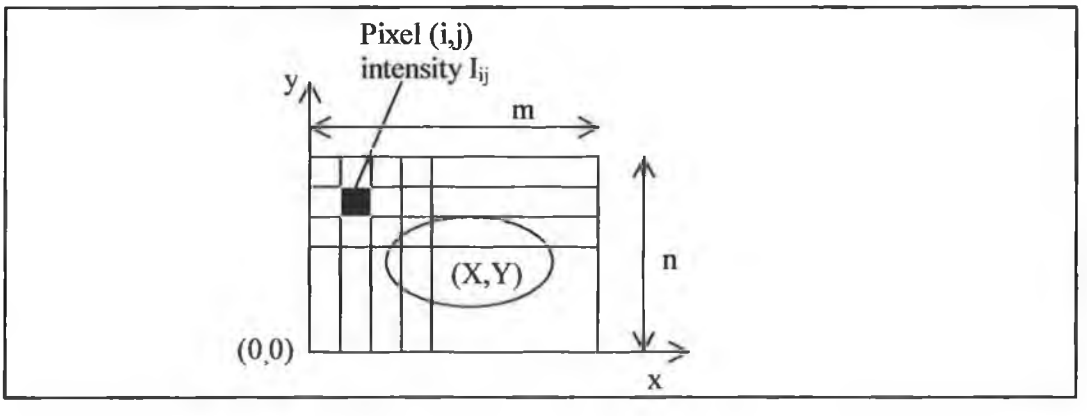

Figure 3.10: Laser beam spot position in an array detector.

Figure 3.10 illustrates the arrangement. The array of pixels has m pixels in the x direction and n in the y direction. The ellipse in the figure represents the laser beam spot enclosed within the image. If, for pixel (i, j) in the array the intensity level is I_{ij}, then the co-ordinates of the centroid are, if the factor at each pixel is taken to be proportional to the intensity level I_{ij}:

$$X = \frac{\sum_{j=1}^{n}\sum_{i=1}^{m} j.I_{ij}}{\sum_{j=1}^{n}\sum_{i=1}^{m} I_{ij}} \quad \text{and} \quad Y = \frac{\sum_{j=1}^{n}\sum_{i=1}^{m} i.I_{ij}}{\sum_{j=1}^{n}\sum_{i=1}^{m} I_{ij}} \qquad 3.17$$

The co-ordinates (X, Y) in equation 3.17 are relative to the array of pixels and defines the centroid in the image co-ordinate system. This equation yields the centroid of the spot position in pixels and allows the triangulation system to determine the location of the center of the spot to a fraction of pixel.

Significant processing was required before measuring the centroid of the image because of the presence of noise present in the image. Important sources of noises are the external illumination, laser speckle, laser focusing, laser power, object reflectivity, electromagnetic interference, signal quantization [76]. Some of the sources of noise have a multiplicative effect on the signal others have additive effect. By thresholding some of the noise can be removed. Thresholding is a technique used to selectively discard unwanted information. The threshold subtraction is base on the supposition that there will be always background noise in any digital image [78-79]. In the figure 3.11, the small intensity values in the pixels that are not part of the real spot will slightly shift the spot's calculated centroid. The horizontal line in the figure indicates where the threshold could be set to counteract the effect of noise.

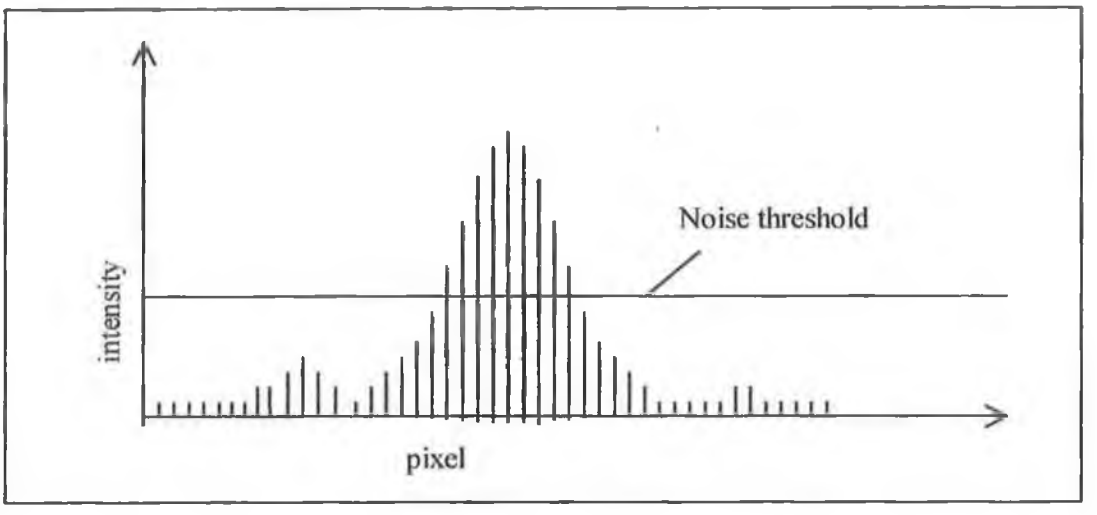

Figure 3.11: Setting threshold to eliminate noise

By setting the threshold above the noise, all pixel values equal to or less than the threshold value are set to zero before calculating the centroid [67]. This removes most of the optical and electronic noise from the image, ensuing that the resulting centroid calculation will not be biased.

Chapter Four

4 Design and Development of the Laser Based Inspection System

4.1 Introduction

In this chapter a detailed description of the design of the system developed in this work is outlined. The basic components are the light source, detection system, optical components the mechanical system and the image analysis software.

Figure 4.1 shows the optical set of the experiment. The laser diode module (CPS186) was used as the illumination source (appendix A). This module has a power of 4.5 mw and produces a laser light with a wavelength of 670nm. The beam spot size at the exit of the laser beam module is 4.4mm x 1.2mm. A laser beam mounting adapter (AD8F) was used for mounting the laser beam modules on the kinematic mount (KC1-T/M) as shown in appendix C1. Two angular controls of the kinematic mount provided an easy means of precisely directing the output of the laser diode module.

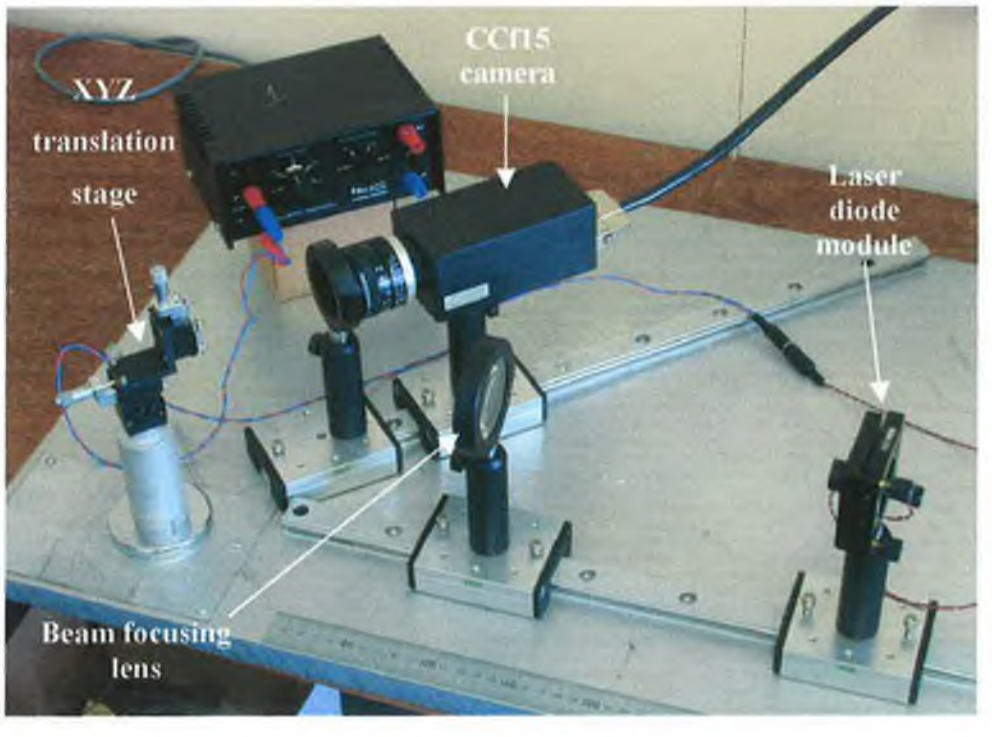

Figure 4.1: Photograph of the experimental inspection system setup.

A post (TR75/M), shown in appendix C2, held the laser diode as assembly a post holder (PH3/M), shown in appendix C3, held the post to the rail carrier. The rail carrier was placed onto the rail, which was secured to an aluminium metal sheet that worked as an optical bench. The rail carrier can slide anywhere along the rail.

A plano convex lens (PLCX-50.8-77.3-C) with 50 mm diameter and 150 mm FL was used as the focusing lens of the laser beam. The distance between the laser diode module and the lens depends upon laser beam spot size required. This distance was adjustable since rail carrier could be slid along the rail on the optical bench.

A camera (CCf15) was used to view the laser beam spot on the sample. The camera was mounted on a post and was placed on another rail system. An objective lens (L25F1.4) and another plano-convex lens (PLCX-38.1-51.5-C) were used as the imaging lenses for the camera.

4.2 Laser Diode Module

Properties and different types of lasers have been outlined in chapter two. A laser diode module is an effective laser source used in different applications. Laser diode modules include a semiconductor laser diode circuit, a driver circuit capable of operating reliably on unregulated low voltage DC input and a collimating lens matched to the laser diode. These are packaged in a rugged housing and provide continuous or pulsed laser output. Many of the modules will permit fine adjustment of the lens position to optimize the collimation or permit focusing to a point at a particular distance. Configuration of the laser diode module is shown in the figure 4.2.

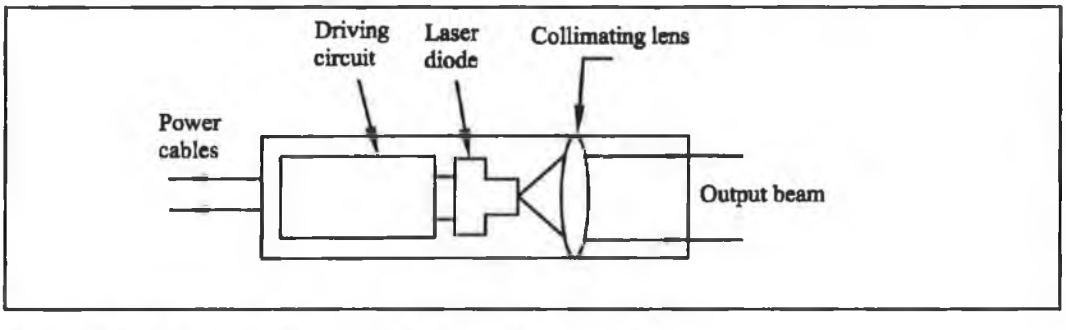

Figure 4.2: Schematic diagram of a laser diode module.

The main beam as it emerges from the laser diode is wedged shaped and highly divergent with a typical spread of 10 by 30 degrees. The beam emitted from the diode laser is characterized by its divergence. Diode lasers generally do not have ideal beam characteristics, but they are fairly easy to focus to the degree that the beam does not widen by more than a millimeter or two per meter. Because the highly divergent output of the laser diode is difficult to work with, the first task usually facing the designer of a laser-diode-based system is the specification of the collimating optics. Performance of the collimator determines spot size, beam divergence, resolution, etc. of the rest of the system, so it is imperative that the collimator quality be sufficient.

Collimating optics are necessary in order to obtain a beam spot. By placing a convex lens in front of the laser diode at a distance nearly equal to the lens's focal length the beam can be reformed. It gives a new wider initial width with a correspondingly lower divergence. In designing a high-quality collimator for laser-diode sources the first consideration is numerical aperture. The numerical aperture is a measure of the light gathering capacity of the lens system. Numerical aperture is the sine of the half angle of collection. For a beam with a Gaussian intensity profile, the $1/e^2$ irradiance point would be about 1.7 times the full width at half maximum (FWHM) of the beam intensity value and the collimator should be designed to collect a cone of light of the range of the divergence angle. The designer of a laser-diode collimating lens must balance the numerical aperture or collection angle against focal length, working distance and output beam diameter. Once collimated to this size, the beam can easily be focused by means of conventional optics if a smaller beam diameter is desired. The Smallest beam width is achieved at the exit of the laser beam module and the divergence is not apparent within the few meters of the lens. The beam shape at the exit of the laser diode module is elliptical.

Selecting a laser diode module is dependent on the types of applications for which it is being used. In measuring surface defects, it is required that the laser beam spot must be small enough to detect the defects with high precision. The laser beam spot of the laser diode module can be further focused using focusing optics. The important criteria in selecting a laser diode module are the following

- Laser diode power,

- Beam wavelength, and
- Divergence.

The estimation of the required laser power is an important step in the design process. The laser diode power range indicates the applications area of the laser diode. According to the power range of the laser diode it can be classified as high power or a low power laser. In surface inspection system development, a low power diode laser is required to measure surfaces with varying reflectance. To get maximum resolution from the imaging system, the beam spot size must be small. So wavelength of the laser diode is one of the important factor in choosing a laser diode module since the diffraction limited laser beam spot is a function of wavelength. Laser diode operating at a higher wavelength produces larger diffraction limited beam spot. Divergence of the laser beam must also be taken into consideration in the selection process, as the diffraction limited laser beam spot is also dependent on the divergence. A Single mode laser diode gives better beam quality than multi-mode ones. When choosing a laser diode module, the associated safety precautions should be considered. The hazards arising in their use vary widely because of the wide ranges possible for the wavelength, energy content and pulse characteristics of the laser beam. The laser system can present electrical, chemical and non-ionized radiation hazards. Radiation hazards are classified on a scale of 1 (safe) to 4 (dangerous).

Semiconductor laser diodes in general are easily damaged by overdriving and by electrical transients. The laser diode is highly susceptible to damage because of the high optical flux density passing through both facets while in operation. In case of overdriving or of transients the optical flux density can rise to unacceptable values, causing catastrophic failure or gradual damage of the laser diode facets. Current transients should therefore be carefully avoided since they may destroy the laser or substantially decrease the laser diode lifetime.

4.3 Optical Sensor System

Solid state optical sensors have found widespread use in a varied range of inspection systems. Consequently, the use of solid state sensors in the form of cameras is increasing rapidly. Until recently, most electronic cameras used charge-coupled

device (CCD) based image sensors [80]. CCD is a well known technology which has been developing for over 30 years now [81]. They have been developed for use in astronomical and everyday cameras, video camcorders and scanners. The basic concept of CCDs is a simple series connection of closely spaced Metal Oxide Semiconductor (MOS) capacitors, which form the pixels of the CCD. The CCD is a type of charge storage and transport device. The light is recorded as an electric charge in each MOS capacitor [82]. Under the application of a proper sequence of clock voltage pulses the charges on the first row of pixels are transferred to a read out register. From the register, the signals are then amplified and converted into digital format. Once the row has been read, its charges on the read-out register are deleted, and the next row enters the read-out register. The charges on each row are thus coupled on the row above and thus the name charge coupled devices. CCD cameras dominate vision applications because of their dynamic range, low fixed-pattern noise (FPN), and high sensitivity to light.

Recently, development of new types of sensor based on Complementary Metal Oxide Semiconductor (CMOS) technology has got much attention as an alternative to CCDs [83]. Image quality of these sensors is increasing rapidly, and at this moment, a performance similar to those of consumer CCDs can be reached. CMOS image devices are in some way very similar to CCDs. The main difference between the two technologies lies in the fact that in the CMOS it is possible to integrate a lot of functions into the sensor. In CCD technology it is much more complicated to integrate additional functionality into the sensor. By integrating camera functions into the sensor itself, it is possible to create a so-called camera on chip.

CMOS sensors have many advantages over its counterpart CCD sensors. There are some limitations for the use of CCD technology in vision tasks. CCD sensors use specialized fabrication that uses dedicated and costly manufacturing processes. In contrast, CMOS image sensors rely on standard manufacturing technology, which produces microprocessors and memory modules [84]. VLSI design for CMOS sensors enables necessary camera functions like noise cancellation, analog-to-digital conversion (ADC), correlated double sampling, timing control, gain control and digital signal processing (DSP) to be integrated onto one chip [85]. Such integration creates a compact, reliable and cost effective camera system. CMOS imagers require

only one supply voltage compared with the three or four that CCDs need. The active pixel architecture in CMOS imagers also consumes much less power than their CCD counterpart. Estimates of CMOS power consumption range from one-third to a hundred times less than that of CCDs. Since CCDs are essentially capacitive devices, it needs external control signals and large clock swings to achieve acceptable charge transfer efficiencies. In CMOS image sensors, both the photo-detector and the readout amplifier are part of each pixel. This allows the integrated charge to be converted into a voltage inside each pixel. CMOS image arrays also have the X-Y co-ordinate readout that the array architecture provides. So the pixels can be read out by the X-Y wires unlike using a charge domain shift register as in CCDs. Windowed readouts provide for electronic zoom functions, which offers much flexibility in applications that need image compression, motion detection and target tracking. In contrast to a CCD imager where a full frame must be read out, CMOS image sensors offer random access and random format generation by suitable pixel sequence readout. Active pixels in CMOS cameras can drive an image array's column buses at greater speed than is possible on CCDs.

There are two types of noise associate with the solid state image sensors: read (temporal) noise and fixed pattern noise (FPN). In CCD-based cameras, FPN is often small because the charge packet associated with each pixel's signal is converted to a voltage at one common output node. The temporal noise in CCD is dominated by either reset and white noise of the output amplifier, or the excess noise of the camera interface. CMOS imagers are fundamentally superior to CCDs with respect to temporal noise, because the amplifier at each pixel operates at much lower bandwidth than the output amplifier. But the fact that each pixel's photocharge is independently converted to a voltage is a drawback in CMOS imagers. The resulting FPN can limit imaging performance more than temporal noise. Hence more signal processing is required to limit FPN, which is achieved by the on-chip circuitry in CMOS sensors.

4.3.1 Fuga Image Sensor

CMOS pixel arrays form the core of a CMOS image sensor. CMOS pixel arrays are based on either active or passive pixels. Passive pixels use a simpler internal structure,

which does not amplify the photodiode's signal within each pixel. Active pixel sensors (APS) include amplification circuitry in each pixel.

The simplest CMOS imaging pixel is a passive pixel, which consists of a photodiode and an access transistor. The photo-generated charge is passively transferred from each pixel to downstream circuits. Signal processing for a passive pixel sensor is done in the support circuits which read each pixel, convert the charge to a signal voltage, amplify the resulting signal, suppress the temporal noise and cancel the support non-uniformity created by these circuits.

APS, on the other hand, incorporate transistors in each pixel to convert the photo-generated charge to a voltage, amplify the resulting signal and reduce noise. The Fuga image sensor is a CMOS active pixel sensor. The Fuga 15 is a 512 x 512 pixels addressable single chip imager with logarithmic response. This digital camera has an on-chip flash 8 bit ADC and automatic illumination control. It behaves like a 256 Kb ROM: after applying an X-Y (row and column) address (x-y position in matrix), the pixel intensity is returned in a digital word (8 bits).

A pixel of the Fuga CMOS active pixel sensor consists of one photodiode and three Metal Oxide Semiconductor Field Effect Transistor (MOSFET) as illustrated in the figure 4.3 [86-87]. The photocurrent generated by the photodiode goes through the transistor M1. Continuous conversion of a photocurrent to an output voltage can be achieved through a series resistor. As the pixel's photocurrent is low (fA to nA range), the value of the series resistance must be very high. In a MOS process, such resistance can only be realized as a MOSFET in resistor configuration. So transistor M1 acts as a non-linear resistor. Because the photocurrent is small, the transistor is in weak inversion and its gate-source voltage is proportional to the logarithm of the drain-source current (photocurrent). At the gate of transistor M2, a voltage is obtained which is proportional to the logarithm of the light intensity. M3 acts a switch, which is closed when the row is selected by the row addressing decoders. When M3 is closed, M2 acts a source follower and puts the voltage of the photodiode on the column read out bus. Unlike CCDs, Fuga sensor does not require any integration time. The sensor is read out constantly. Every pixel is a photodiode measuring an amount of light flux. The moment a pixel is addressed, the value readout is the instantaneous

measurement of that pixel. As the address pulse timing does not have to synchronize to some integration time, the imager is truly random addressable.

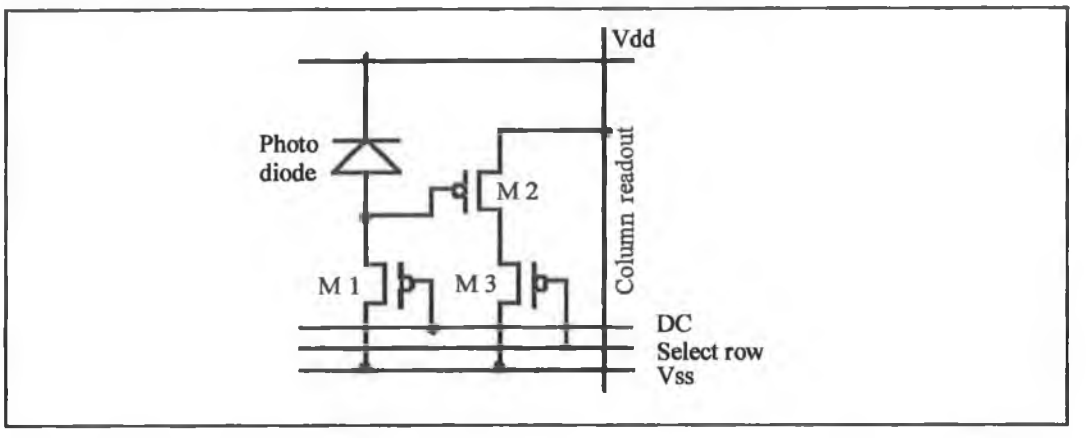

Figure 4.3: Schematic representation of the pixel structure [86].

4.3.2 Architecture of the Image Sensor

Figure 4.4 shows a photograph of the Fuga 15 image sensor chip. The imager itself contains an array of pixels, which are selected by address decoders. The architecture is given in figure 4.5. A row of pixels is selected, by latching in the row co-ordinate with the enable-y signal (E_y). The pixels of this row can be selected with the column multiplexer. This is an address decoder, which selects the column line, which is latched in through the enable-x signal (E_x).

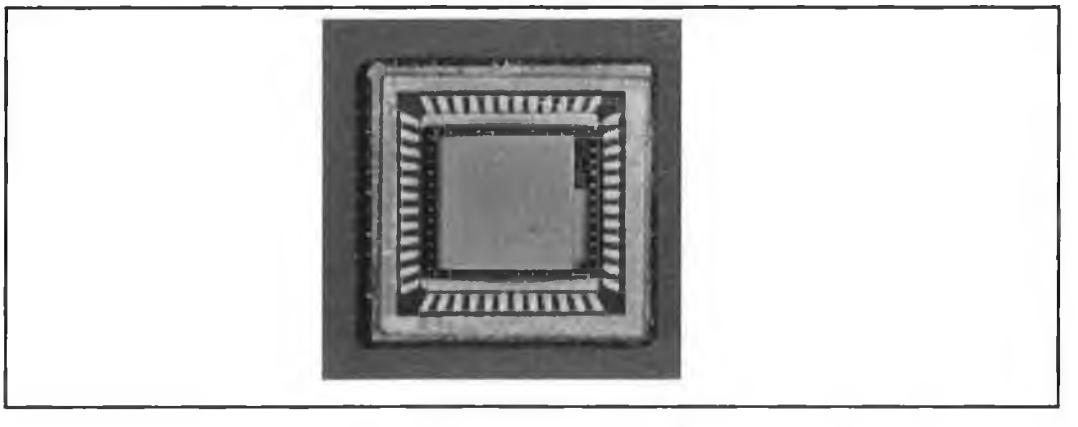

Figure 4.4: Photograph of the Fuga 15 image sensor

The analog signal of the selected pixel goes then through the output amplifier to the ADC. The ADC has a tristate output port, and it is read out when E_c is low. In this

way, the pixel address and the ADC output are placed on the same (bi-directional) bus. The task of the offset control circuit is to adjust output level of the pixels, which are read out to the middle of the ADC range. The entire dynamic range of the pixels can be mapped to the ADC input. The offset control circuit adjusts the offset level of the output amplifier so that the average analog output is always in the middle of the ADC range. It is essentially a low pass filter on the analog output stream. An 8-bit analogue to digital output is provided from the flash ADC. The timing signals for driving the shift registers and the digital output stage are provided externally.

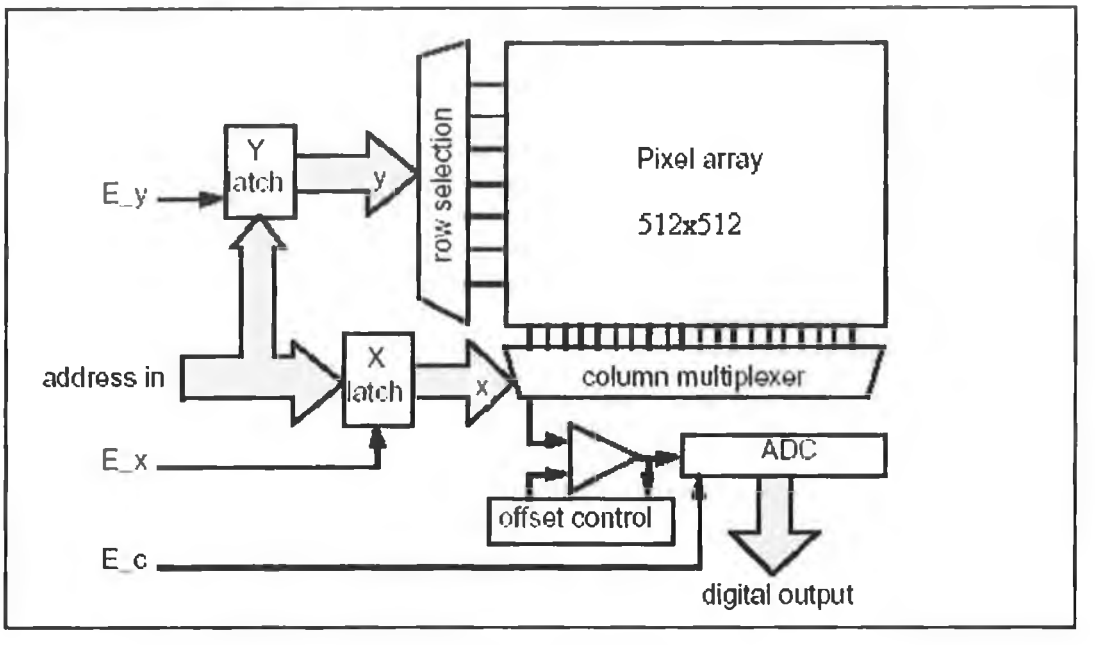

Figure 4.5: Architecture of the Fuga 15 image sensor.

4.3.3 Offset Correction

A consequence of the logarithmic photo response is a low output voltage range. The output voltage, typically 50mV per decade of light, is in the same range as the pixel offset non-uniformity. Therefore the raw images are almost useless. Calibration of this offset non-uniformity is mandatory.

Due to the nature of the active pixels, the non-uniformity (spatial noise, pixel-to-pixel offset, soft errors) is very high compared to the useful signal level. Three kinds of errors occur: missing pixels, missing rows and missing columns. Main cause of failure is apparently saturated pixels. If the calibration made is not made according to the

surrounding light levels, in some cases not all pixels respond equally to the change. In dark conditions, they can be viewed as white pixels (also called hot pixels). So, it is evident that due to the non-uniformity a raw image will show almost constant noise in the same conditions. Due to the large inherent non-uniformity, it is necessary to calibrate all pixels in order to obtain an image with acceptable quality. The non-uniformity noise is unique for every pixel; it can be used as a "fingerprint" to determine the origin of the image. Fixed pattern noise can be corrected with a first-order correction in a memory module. A pixel-per-pixel offset correction can be performed in hardware or in software. The most straightforward method for calibration is by software. The offset per pixel is stored in an array in main memory, and subtracted when the pixel is read. This offset can be obtained for example by reading a homogeneous white or grey image with a representative brightness level. Figure 4.6 (a) shows an image captured with the sensor without calibration. It is evident from the image is that the quality is poor and requires calibration in order to achieve a better image. Figure 4.6 (b) shows the calibration image, which is saved in the PCI-LVDS interface and carries out the calibration. Finally, figure 4.6 (c) shows the calibrated image with better quality with respect to the uncalibrated one.

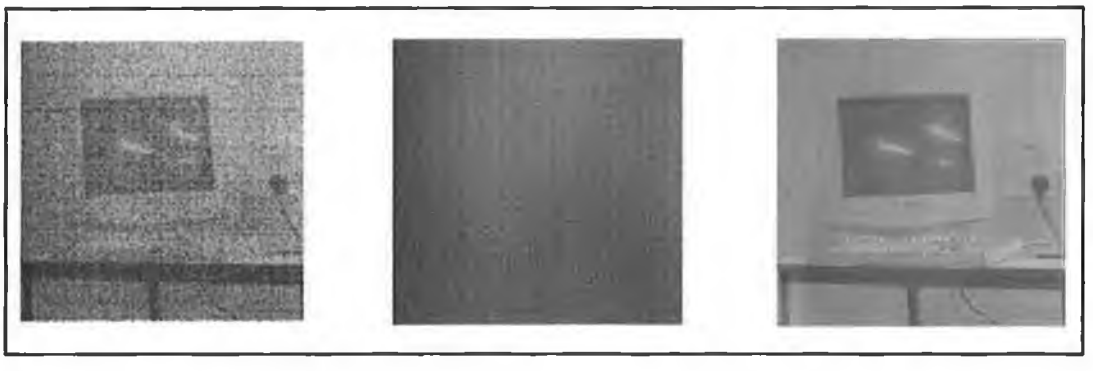

Figure 4.6: (a) image without calibration (b) calibration image (c) image after calibration

The disadvantage of this system is that the pixel access is somewhat slower due to additional memory accesses and calculations. For most applications, a first-order correction is satisfactory. In cases where the non-uniformity is to be expected between extreme light levels and temperature differences, a more advanced calibration is advised. If only a first-order calibration is performed, the image will show a small number of white pixels in dark conditions and black pixels in bright conditions. These

are not "dead" pixels, but rather the response curve of these pixels should be corrected to account for second order non-uniformity.

4.3.4 Interfacing

The real advantage of a random addressable camera is the possibility to examine parts of an image much faster than "real time", i.e. faster than the video frame rates of 50 Hz or 60 Hz. So a pixel-level interface to hardware devices as digital signal processor (DSP) or microprocessors are required. The interface of the Fuga 15 is suited for direct coupling to the data and address bus structure as found in DSPs or microprocessors. The Fuga pixel information is thus available in the address space of the processor. A fast PCI-LVDM is as the interface for the fast Fuga camera head. The PCI-LVDM is a powerful imaging interface between a C-Cam CMOS camera and an IBM compatible PC. The interface card has a flexible functionality and high speed data processing. The card is not restricted to a predefined image size. Any image size and ratio can be processed, even single, user-defined lines. It is designed for the latest generation CMOS cameras with special features. This PCI card is able to do some on board preprocessing. The PCI card runs as a slave card and it allows to read a window of interest of the Fuga camera, or to access individual pixels. The card performs the following functions:

- It generates the X- and Y- addresses of the pixels to read.
- It takes into account the horizontal and vertical delays when switching between pixels and lines.
- It stores calibration image.
- It corrects the grey values for fixed pattern noise, base on a calibration image.
- It controls the position of the ADC window with respect to the dynamic range of the sensor.
- It selects the active camera on a multi camera PCI interface.
- It reads the grey values of the pixels.

After initialization, the PCI card can run in two modes: either it reads a window of interest (WOI) or it reads a single pixel per command. In order to read a WOI, the card uses the coordinates of the window, the camera identification and the delay

values stored in its registers to generate the correct addresses with the required timing. The acquisition of a WOI is started by putting a command in the Control Register. To read only one pixel, the X- and Y- addresses are stored in the Direct_Pixel_Access register, which automatically triggers the read operation for the requested pixel. The Status Register contains information regarding the current operation of the card, and the Data Register contains the grey values read.

4.3.5 Features of the Fuga 15 Sensor

Pixel Speed

The pixel speed of Fuga 15 camera is limited. This is because all amplification is realized at the analog output of the sensor. The pixel readout speed of FUGA 15 with the PCI-LVDM card is more than 3.7 MHz for one camera head when the sensor is at its full window size (512x512 pixels). But displaying the image is somewhat slower to a speed of 2 MHz because of the speed limit of the VGA card of the computer connected to the Fuga 15 camera. It is necessary to block the display, and an increase of speed is seen from 500 kHz to about 1 MHz. The pixel speed can be increased by altering the rows and column delays.

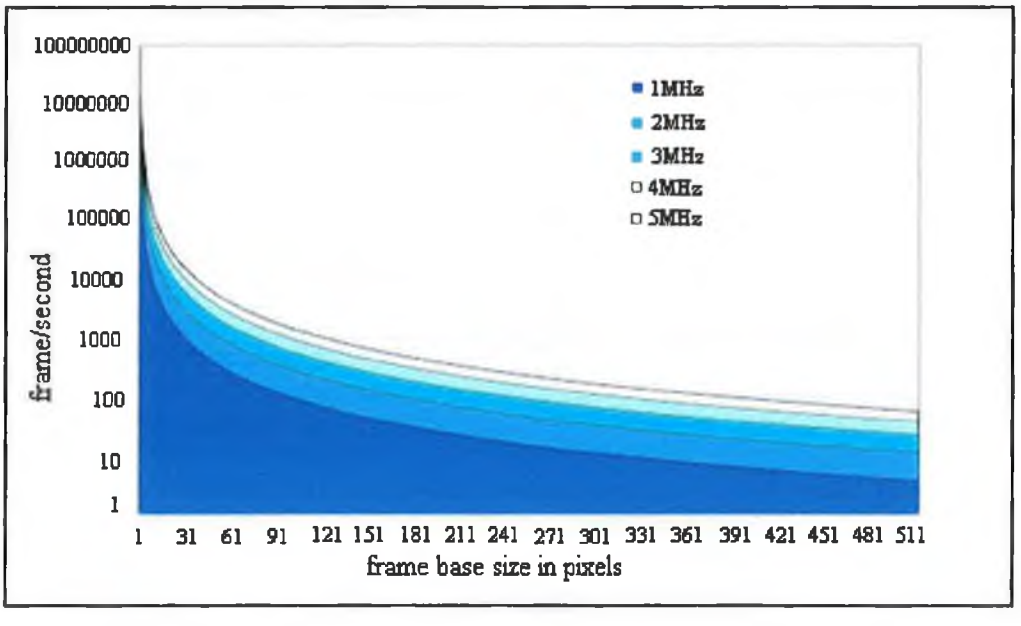

Figure 4.7: Frame speed of the Fuga 15 sensor at different WOI [88].

Random access to pixels makes it possible to achieve very high frame rates if the WOI is limited. As the WOI can be changed, also the frame speed can be changed. The speed curve in the figure 4.7 shows the raw camera frame speed as a function of size of the window of interest.

Sensitivity

The logarithmic response of the sensor results in an extended dynamic range of 120 dB (6 decades of light). Figure 4.8 shows the camera sensitivity curve displaying the dynamic response. The Fuga 15 sensor is specially designed for very high light levels. The ADC of this sensor is set to cover 4 decades of illumination.

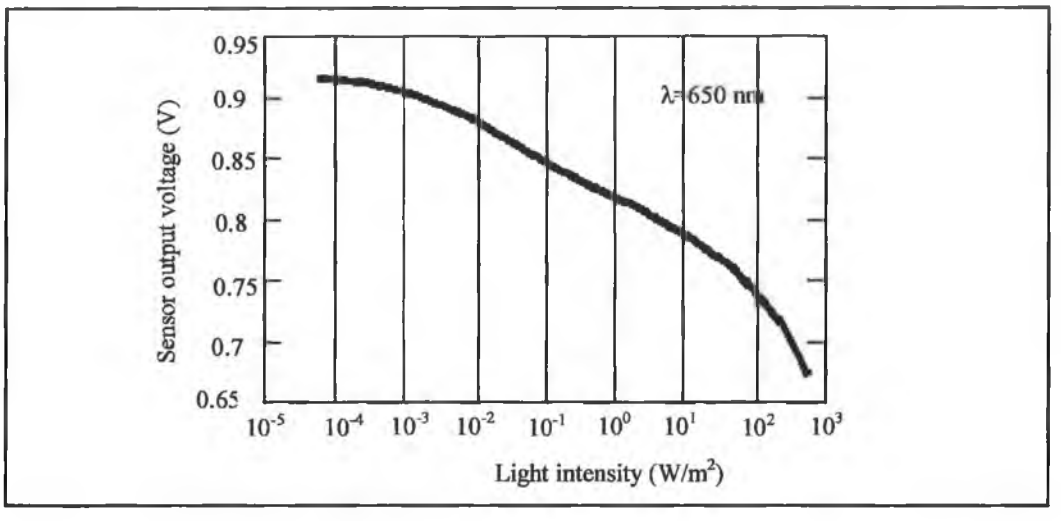

Figure 4.8: Response of the sensor with respect to the light intensity at the sensor level [89].

Automatic Illumination Control

As the ADC only cover 4 decades of illumination, its range can be shifted relative to the 6 decade range of the sensor. Automatic gain control ensures the average light intensity corresponds with the mid point of the ADC range.

Smear

Smear is a spurious signal seen more or less as a bright vertical column on the monitor. Fuga offers very low level of smear. For a background illumination of 110 fW/cm^2, visible smear appears (vertical white stripe) from a spot intensity of 8 mW/ cm^2 (wavelength=750nm).

Response Time

Figure 4.9 shows the spectral response curve. Ideally, the sensor should react instantaneously. But due to internal resistance and capacitance of the sensor, an effect of finite response time is noticed. From the spectral response curve of the Fuga sensor, it can be seen that not all parts of the spectrum have the same response. As the sensor is less sensitive in the area in and above the red spectrum than for the other colors (Fuga 15) the effect of response time will also be more visible in that region. From the figure it is seen that the spectral range of Fuga 15 sensor is between 400-1050 nm.

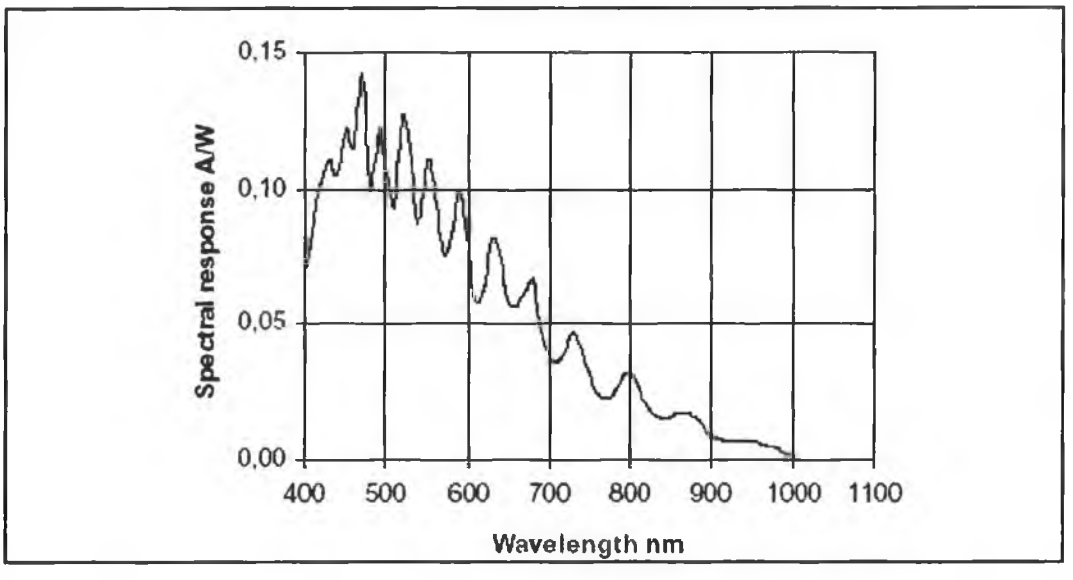

Figure 4.9: Spectral response of the Fuga 15 sensor [89].

The response time is a result of the non-integrating nature of the sensor. Less current is needed for bright illumination. The darker the pixel gets, the more current will flow though the pixel. It takes longer to change from a lower current level to a higher

current level than vice versa. The response time of the Fuga 15 + ADC combination is about 2.5 μs after changing the X-address. If the readout is too fast, a fixed pattern offset will appear. To solve it, optimized impedance, ADC, or an additional delay time must be included.

The time to reach equilibrium after changing the Y-address can be longer when capturing dark images. An additional waiting time may be needed in lower illumination conditions. If no sufficient waiting time is allowed, an band of apparently lighter pixels will appear at the left edge of every line.

Temperature can also have an effect on the response. The higher the temperature, the less sensitive a sensor will be. i.e. spectral response curve moves downwards at higher temperatures. The lower the response curve, the larger the time delay will be.

4.3.6 Software

The name of the camera used in this work is CCf15 that contains Fuga 15 as the image sensor. In order to operate the camera software is required and it is required that the PCI-LVDS interface is installed in the PCI slot of the PC. The software and the driver for the PCI-LVDS were provided by C-CAM Technologies to run the CCf15 camera. The software was originally written in Delphi4 Standard edition. The software demonstrates the use of the CCf15 camera in a Delphi environment The CCf15_mini_demo has been developed from a number of source files and with the help of CCf15.DLL file. The Dynamic Link Library (DLL) file is the link between the executable program and the driver.

The software is capable of operating the CCf15 camera with the PCI-LVDS interface. The PCI-LVDS card is able to operate an automatic gain camera and a controllable gain camera. A calibration routine is included in the program. The program calculates a calibration image from a sequence of 10 images. This gives a smoother calibration image with adjusted brightness. This image is automatically stored in the PCI-LVDS interface card. A video routine is used to display the image. The program detects the lazy pixels and corrects them. Lazy pixels are those pixels that are slow to respond to

the changes of the surrounding lighting level. In order to detect lazy pixels a histogram is made from the sample image. The centroid of the histogram is taken as reference. To distinguish lazy pixels from the surrounding area, a threshold above this centroid point is taken. The database formed with the "detect lazy pixel" routine is merged with the current calibration file and transferred to the PCI-LVDS interface. The program employs gamma correction to enhance contrast of the image. A complete 255 grey value scale is possible on the monitor. Figure 4.10 shows the complete window of the software. The program contains a list of menus and check boxes. Table 4.1 shows the lists of menu and sub menu.

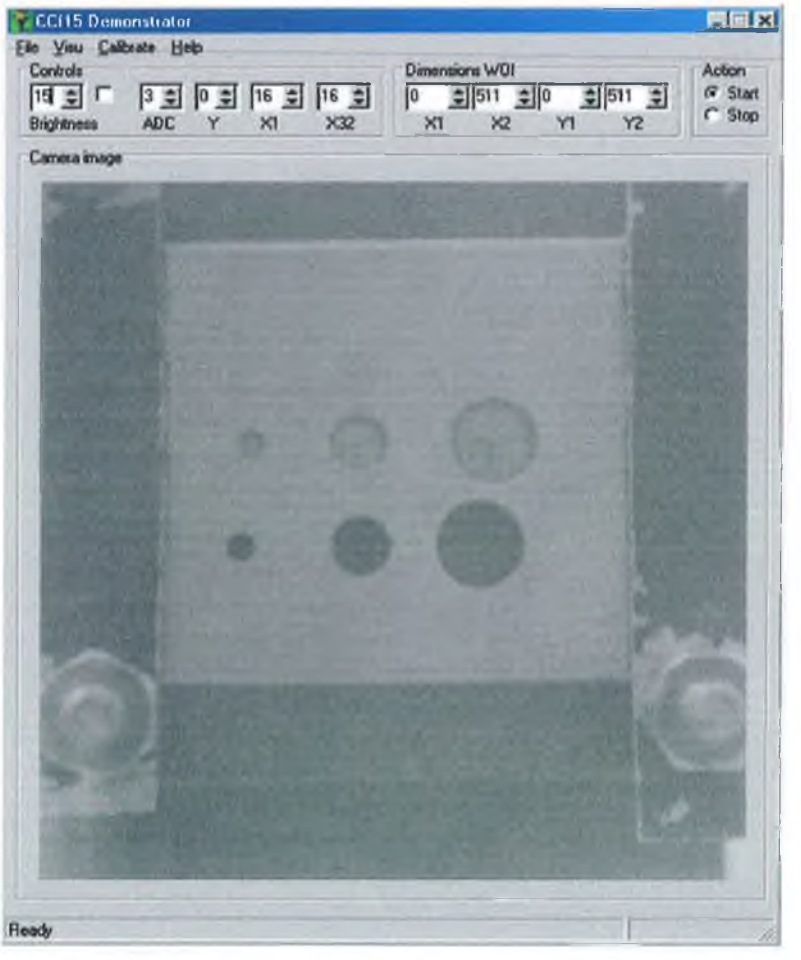

Figure 4.10: Window of the CCf15 camera software.

File	Visu	Calibrate	Control	Dimensions WOI	Action
Save image	Gamma Correction	Get new Calibration	Brightness	X1	Start
Exit	Automatic brightness	Save calibration	ADC delay	X2	Stop
		Load calibration	Y-delay	Y1	
		Current calibration	X1-delay	Y2	
		Detect lazy pixels	X32-delay		
		Lazy pixel Correction			
		Settings			

Table 4.1: List of menu and submenus.

This demonstration software allows the use of the PCI-LVDS card according to the following specifications:

- Starts and stops the camera.
- Read a frame of any size, choosing the size and position of the WOI
- Change reading time and ADC time.
- Read, save and load the calibration file.
- Show the current calibration files.
- Detect and correct the slow responding pixels.
- Controls brightness automatic and manually.
- Save the frame with the possibility to choose the file name and directory.
- Enhance the contrast by gamma correction.

4.4 Optical System.

In developing the inspection system, it is imperative to choose correct optical system to get best image of the beam spot on the surface. Design of the optical system is necessary in order to focus the laser beam to a smaller spot, filter the intensity of the laser beam to avoid the beam dispersion on the surface and to produce the correct image of the laser beam spot onto the sensor. Optical systems incorporating the inspection system are thus the laser beam focusing lens, filter and the camera optics.

4.4.1 Focusing Lens

The focusing lens is used to obtain a smaller laser beam spot on the object than at the exit of the laser diode module. Reshaping of the laser beam spot is necessary to get higher resolution from the system. It was seen in chapter two that the diffraction limited laser beam spot is a function of the focal length of the lens used. Smaller focal length results in a smaller diffraction limited spot. The focusing of a laser beam is trade off between beam diameter and depth of field. If the beam diameter were to be smaller, the depth of field would be smaller as well. Operating range of the system is determined by the depth of field. Smaller beam diameters increase the power density and are generally desirable for material processing applications.. Beam diameter and depth of field are related by the equation.

$$z = 0.32\pi w^2 / \lambda \qquad 4.1$$

where w is the beam diameter and λ is the wavelength of the laser beam. The depth of field, z, is defined by the distance where the beam diameter has increased by 5%. The selection of the lens is dependent on the objective of the application: whether a smaller beam diameter or large operating ranges is required. A plano-convex lens was used in this work for focusing the laser beam.

4.4.2 Attenuation Filter

Optical filters are used in many laser applications where accurate numerical measurements are needed. This requires that filter characteristics be accurately controlled and specified. Typical applications for filter involve improving contrast or

signal-to-noise ratio (imaging or non-imaging), isolating particular wavelengths and improving lens performance. Filters can be used to attenuate light either evenly or unevenly across certain portions of the spectrum.

Attenuation filters are used to reduce the intensity of a light beam. High quality attenuation filters are said to have a flat response. This means that they attenuate all wavelengths of light over their usable spectral range by the same amount. Attenuation filters are used to reduce the intensity of the light received by the imaging system. Attenuation of the laser beam is required to avoid dispersion of the beam on the surface where it is incident that could saturate of the sensor pixels.

Attenuation filters can be divided into two groups according to the mechanism used to reduce the beam power.

Geometrical Filters

Geometrical filters physically block a fraction of an aperture through which the light beam passes. If the beam is uniform in intensity across the aperture, then the percentage of the aperture area that is blocked is the percent reduction in beam power. Iris diaphragm is one example of a geometrical filter shown in figure 4.11. This iris or "stop" is used to reduce the aperture of a light beam. A stop is an opaque element with a roughly circular opening to permit the passage of light.

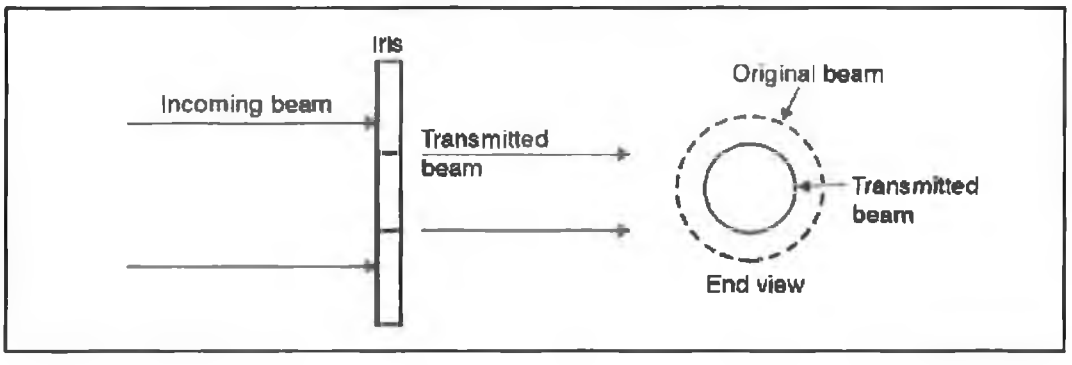

Figure 4.11: Iris diaphragm acts as a geometrical filter.

Neutral Density Filters

Neutral density filters are designed to reduce transmission evenly across a portion of the spectrum. There are two types: absorptive and reflective. In absorptive filter light is absorbed, while reflective filters reflect it away. The term "neutral" is designated because the absorption or the reflection characteristics of the filter are constant over a wide wavelength range.

4.4.3 Camera Optics

An imaging lens is needed to provide an accurate representation of the image to be captured. Light from the object passes through the lens and forms an image where the sensor is located. Lenses are classified by format, mounting, focal length and f-number. Lens format is the specification of the size of the image that the lens can produce. The measurement of a lens format is related to the diagonal size of the image sensor. The lens is designed to mount into a standard fixture that surrounds the image sensor and there are several standards for CMOS camera systems. These include C-mount, CS- mount and S-mount. The focal length indicates the magnification obtained from a lens for a given imaging condition. F-number is a measure of the light gathering ability of a lens; more precisely it is the ratio of the lens's focal length to its aperture (focal ratio). The f-number increases as the lens aperture is closed. Smaller f-number let in more light. Closing the aperture also increase the depth of field of the system.

The CCf15 camera is mounted with a C-mount lens holder. It is defined with the thread of 1" (25.4 mm) in diameter and 32 threads/inch, and the back flange-to-CMOS sensor distance of 17.526 mm (0.69"). Back flange is defined as the distance from the mount reference plane to the image plane. The C-mount lens holder acts an interface with different standard optics.

Instead of a C-mount lens an objective lens was mounted on the C-mount of the CCf15 camera. An objective lens is required when the camera-object distance for the required magnification is shorter than the focus range and when the camera is positioned closer to the object. The objective lens is a lens system, which is typically

constructed from a series of individual spherical lenses and stops centered on a common axis [90]. The objective lens has a thread attached to fit into the C-mount lens holder. The element that most limits the angular spread of the bundle of rays that will pass unobstructed through the system from the axial point on the image plane is termed as the aperture stop. Consequently it reduces the transmitted beam power. The size of the aperture stop in a camera is set through the use of an adjustable diaphragm, and serves to provide control over the quantity of light striking the sensor plane and the depth of field in the image. Figure 4.12 shows the profile view of the objective lens system. The diaphragm, drawn in solid black, acts as the aperture stop for the point x on the axis at the film plane. An Electrophysics L25F1.4 objective lens system was used in this project. The effective focal length of this objective lens is 25mm.

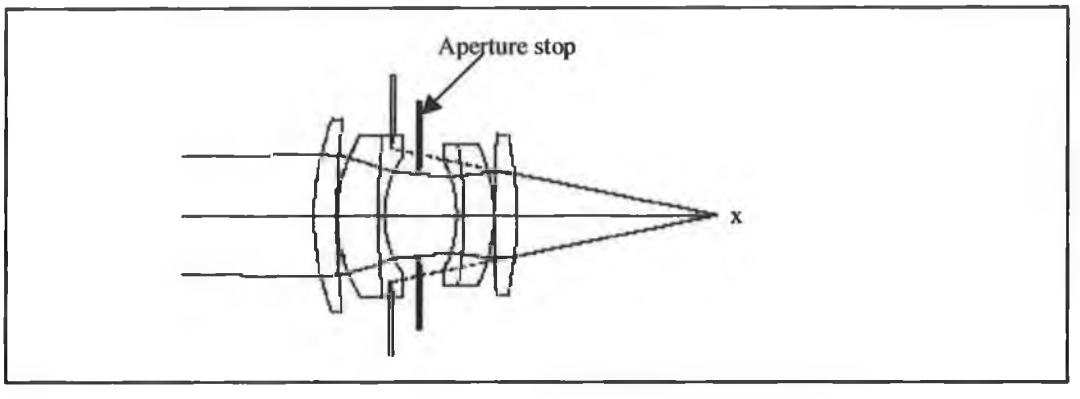

Figure 4.12: The objective lens system with diaphragm acting as aperture stop [90].

4.5 Mechanical System

The mechanical systems required to develop the inspection system consists of a translation stage, kinematic mounts, posts, post holders and rail carriers.

4.5.1 Translation Stage

A translation stage was required in order to obtain three-dimensional motion of the surface to be inspected. The translation stage consists of three micrometer driven stages in X, Y and Z axis directions. The X and Z stages are mounted on top of each other oriented perpendicularly. The Y stage is mounted vertically on the X and Z stages with the help of an angle bracket. The bottom stage is mounted on an

aluminum base plate. Each stage has travel length of 6.6 mm. These micrometers have sensitivity of 1 μm and the vernier divisions are of the order of 10 μm. The stages include position-locking features.

4.5.2 Kinematic Mount

Stable mountings and positioning are required to build optical systems. Kinematic mounts offer simple and economical positioning of the optical system. A mount is said to be kinematic when the number of degrees of freedom (axes of free motion) and the number physical constraints applied to the mount total three translations and three rotations with respect to some arbitrary fixed co-ordinate system. The advantages of a kinematic mount are increased stability, distortion free optical mounting, and in the case of a kinematic base, repeatable re-positioning. A Thorlabs [91] kinematic mount KC1-T was used in developing the present system. Features of this kinematic mount are:

- ± 5 ° Angular Translation
- ± 3mm Linear Translation
- Flexure locking mechanisms allow independent locking of all 3 adjusters

The kinematic mount is used in this system to mount the laser diode. An adapter was used for mounting the laser modules in the kinematic mount. The two angular controls of the kinematic mount provide an easy means of precisely directing the output of the module.

4.5.3 Posts and Post Holder

Posts and post holders are the most commonly used devices for mounting optical component holders. They permit a significant amount of vertical and angular adjustment for coarse alignment. Thorlabs [91] TR75/M posts were used in this system. One end of the post has a 1.4"-20 (M6) tapped hole, the other end has a removable #8-32 (M4) threaded stud. Optical component holders were mounted on the post by the removable M4 threaded stud. Thorlabs post holder PH3/M was used to

hold the posts. It is a tube where the post can slide inside it to make required adjustment. A spring-loaded plunger within the brass thumbscrew was used to hold the steel post firmly within the post holder prior to final tightening. This allows one-handed positioning of post mounted device. Posts and post holders were used to mount the kinematic mount, lenses and the camera in the present system in order to provide a perfect alignment among all the optical components.

4.5.4 Rails and Rail Carriers

Rail systems were used to obtain a good lateral alignment of the optical components mounted on the rail carriers. The rail's dovetail profile and snap-on carrier design [91] allowed for the easy insertion and removal of optical components onto the rail systems. The rail carrier contains a number of small metallic bearings at its inner side that allowed the sliding on the rail. It also has a number of tapped holes (M4). Post holders were bolted to the rail carrier from underneath. The rail carrier holding the optical components could be moved along the rail to provide distance adjustment between the optical components. The rail carrier was held tight to the rail by a grabscrew. A number of mounting holes and slots were provided to achieve flexibility when building the optical systems. The rails were bolted to the aluminum plate used as optical bench.

4.6 Software Design and Development

Software was developed for this project which was intended for the processing and analysis of the images captured by the inspection system. The programs developed were split up into three different parts according to their objectives. The first set of programs was used to read the image files from the camera and converts them into text format. The second set of programs operated on the text file to determine the centroid location of the laser beam spot. Once the centroid locations were determined, another set of program was used to perform the distance measurement calculation.

The data analysis and the program development were performed using National Instruments LabVIEW software [92]. LabVIEW is specifically designed to quickly implement a computer-controlled data gathering and analysis system, which can be

extensively customized to suit user requirements. LabVIEW is an entirely graphical language, which uses graphical programming language, G, to create programs in block diagram form. LabVIEW includes an extensive library of functions and development tools designed specifically for data acquisition and instrument control. LabVIEW programs are known as virtual instruments (VIs) because they imitate real instruments. VIs have three parts: the front panel, the block diagram and the icon/connector. The front panel is the graphical user interface (GUI) of a VI and the block diagram is a pictorial description or representation of the program.

4.6.1 Bitmap Image File to Text File Conversion Algorithm

Images captured by the CCf15 camera were stored in a bitmap (BMP) file format [93]. Bitmap images, also known as raster images, are made up of pixels in a grid. Pixels are picture elements; tiny dots of individual color. Every bitmap image contains a fixed number of pixels, measured in pixel height and pixel width (the number of pixels displayed along the height and width of the image, respectively). The total number of pixels determines the file size, or the amount of data in the image. Windows bitmap files are stored in a device-independent bitmap (DIB) format that allows Windows to display the bitmap on any type of display device. The default filename extension of a Windows DIB file is .BMP.

Each bitmap file contains a bitmap-file header (BITMAPFILEHEADER), a bitmap-information header (BITMAPINFOHEADER), a color table, and an array of bytes that defines the bitmap bits. The file has the following structure:

```
BITMAPFILEHEADER bmfh;
BITMAPINFOHEADER bmih;
RGBQUAD          aColors;
BYTE             aBitmapBits;
```

The bitmap-file header contains information about the type, size, and layout of a device-independent bitmap file. The header is defined as a BITMAPFILEHEADER structure.

The bitmap-information header, defined as a BITMAPINFOHEADER structure, specifies the dimensions, compression type, and color format for the bitmap. BITMAPINFOHEADER structure determines the number of bits that define each pixel and the maximum number of colors in the bitmap. The color table, defined as an array of RGBQUAD structures, contains as many elements as there are colors in the bitmap. The color table is not present for bitmaps with 24 color bits because each pixel is represented by 24-bit red-green-blue (RGB) values in the actual bitmap data area.

The bitmap bits consist of an array of BYTE values representing consecutive rows, or "scan lines," of the bitmap. Each scan line consists of consecutive bytes representing the pixels in the scan line, in left-to-right order. The number of bytes representing a scan line depends on the color format and the width, in pixels, of the bitmap. If necessary, a scan line must be zero-padded to end on a 32-bit boundary. The scan lines in the bitmap are stored from bottom up. This means that the first byte in the array represents the pixels in the lower-left corner of the bitmap and the last byte represents the pixels in the upper-right corner.

In order to analyze the image, it was required to convert the bitmap image format into text format. Pixels in the bitmap image are held as an array of numbers ranging from 0 to 255 known as grayscale values. Each pixel in a gray-scale image has a brightness value between 0 to 255, where 0 represents black and 255 represents white. If each pixel voltage is converted to an 8-bit digital word, the result is an array of words ranging in intensity from 0 to 255. So conversion of the bitmap format to text format renders an array of grayscale values. The region where the laser beam spot shun on the surface was represented by higher intensity values in contrast to other regions in the surface. The number of elements in the array was determined by the number of pixels selected when choosing the window of interest (WOI).

In order to read a bitmap file it was required to know the header information of the bitmap image. Figure 4.13 shows the block diagram of a program that provided the header information of the bitmap image. LabVIEW identifies an open file by associating with a function called refnum. File refnums identify each open file while operations are performed on it. The program read a bitmap file specified by a refnum

and extracted the header information of the images from the BITMAPINFOHEADER structure. This information included the height and width of the image in terms of number of pixels, bit depth and padded width. This program also read the color table. Knowledge about the height and width are required in order to determine the number of pixels present in the image.

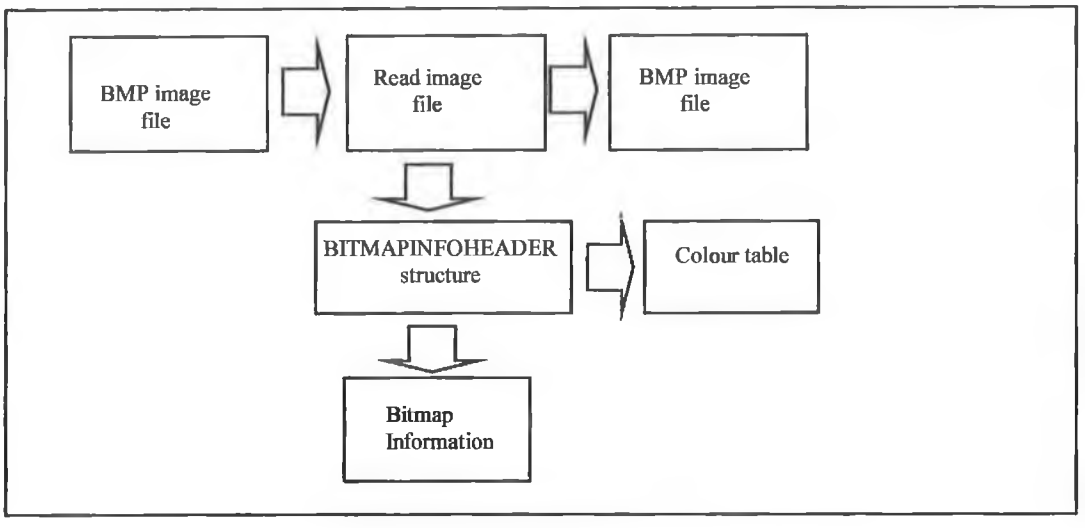

Figure 4.13: Block diagram of the program written to read the bitmap header information.

Figure 4.14 shows the block diagram of the program that read the bitmap file using the header information. This program opened the image file from the path specified and created a refnum that was read. This program first generated the one-dimensional arrays of bytes of the bitmap file. Another VI took the raw BMP data and unpacked its pixel values so that each pixel was represented by an element in a 2D array of bytes. The bitmap image file was then converted to text format in 2D array of bytes.

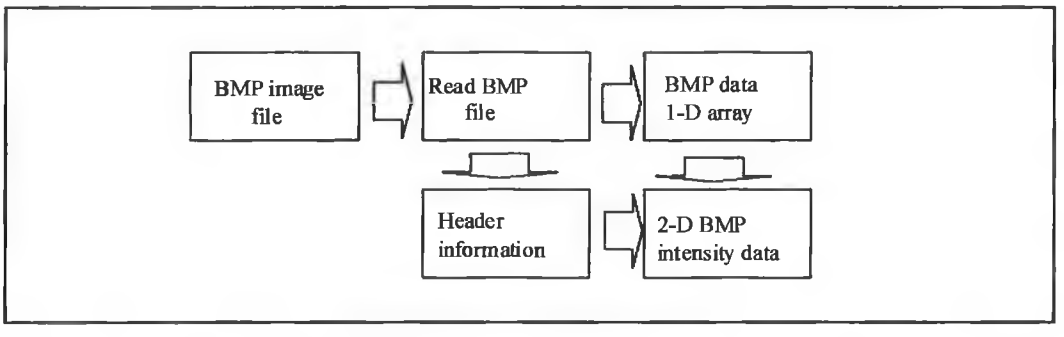

Figure 4.14: Block diagram of the program to convert BMP image data to BMP intensity data.

4.6.2 Image Spot Centroid Location Algorithm

The method to measure the laser beam spot position on the sensor was described in section 3.4. The block diagram of the program to compute the centroid is shown in the figure 4.15. This program read a BMP image file and generated an array of intensity data of the pixels using the program mentioned in figure 4.14. The array of intensity data was then analyzed to carry out the calculation for determining the centroid location of the laser beam spot in the array. A Threshold value is set to discard the noise level before the centroid calculation has been made. Centroid position of the laser beam spot image was expressed by the X and Y co-ordinates in terms of number of pixels from any arbitrary position.

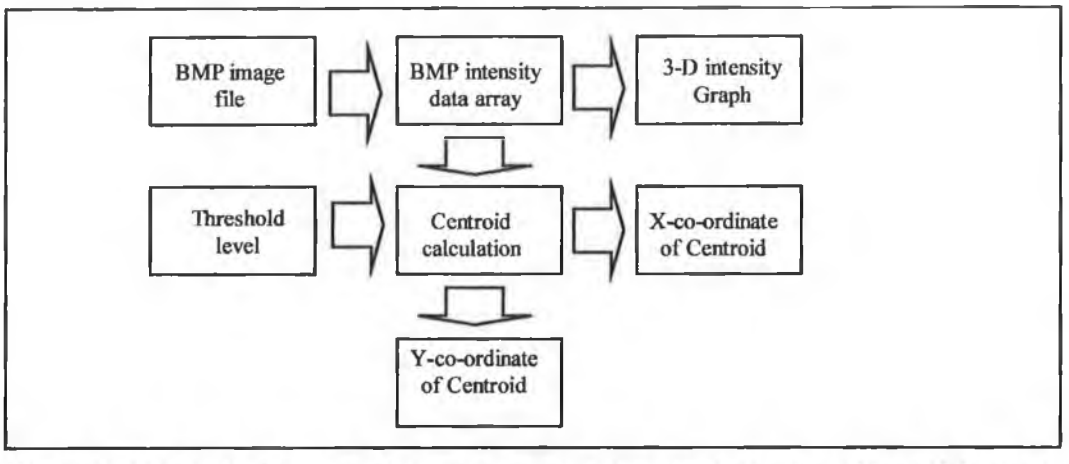

Figure 4.15: Block diagram of the program to compute centroid position of the laser spot on the image.

4.6.3 Algorithm to Detect Surface Defects

This part of the software development dealt with the implementation of the triangulation method in order to perform surface profile measurement. In order to perform this, images of the surface were captured at known positions. For 2-D surface reconstruction, images were taken at a constant distance apart in the X-direction (see figure 3.7). This was achieved by moving the X-stage, which held the sample, by this constant distance and recording the image at each location. These images were saved to separate files within the same directory. These image files were then read and analyzed to reconstruct the 2-D surface according to the program shown in figure 4.16. Initially, the centroid position of the first image, which was taken on the

reference plane, was calculated and set as the reference centroid. A program loop was then executed until all the files had been read and analyzed and an array of laser beam centroid positions was generated. The laser beam spot shift with respect to the reference surface was calculated by subtracting the array elements from the reference centroid. A calibration factor (see section 3.3.1) is than applied on the array of beam shift values to obtain the depth value array, which were then written to the spreadsheet files. X-axis values corresponding to the depth value (Z-axis) were calculated also from the array of beam shift values, "camera resolution" and "X-stage step size" and were written to the spreadsheet file.

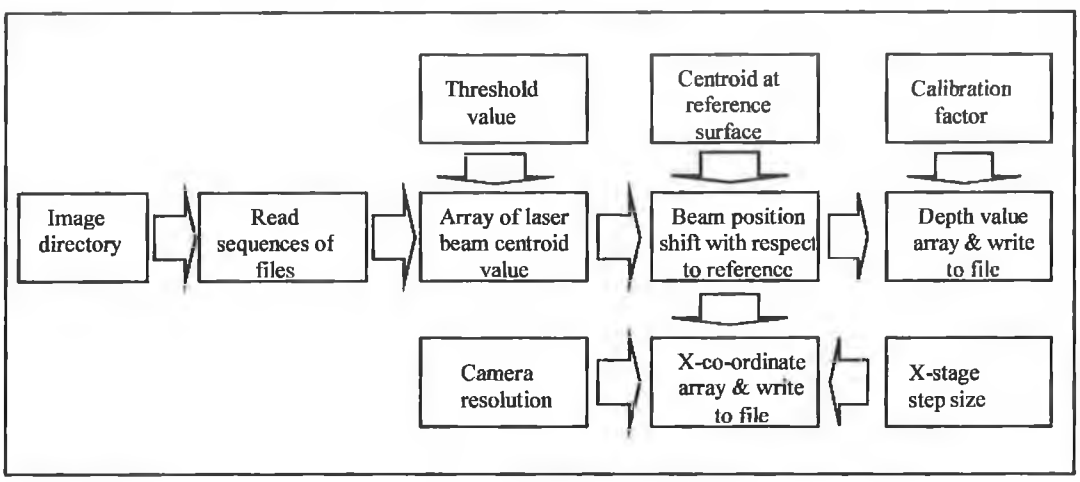

Figure 4.16: Block diagram of the program to measure displacement characteristics.

Figure 4.17 shows the block diagram of the program that generated the three-dimensional surface map of the scanned surface. The algorithm was almost the same as the 2-D surface reconstruction algorithm. In order to generate a 3-D surface map, the program created three 2-D arrays that specified the X, Y and Z planes. The size of these arrays were determined by the number of scans in X and Y direction. Data values in the Z-axis array were the depth values of the surface being scanned and were corresponded to the X and Y coordinates in order to create the 3-D surface map. Data elements in the X-axis and Y-axis arrays were scan positions along X direction and Y direction respectively. The principle to measure the X-axis values and Y-axis values are described in equations 3.13, 3.14 and 3.15.

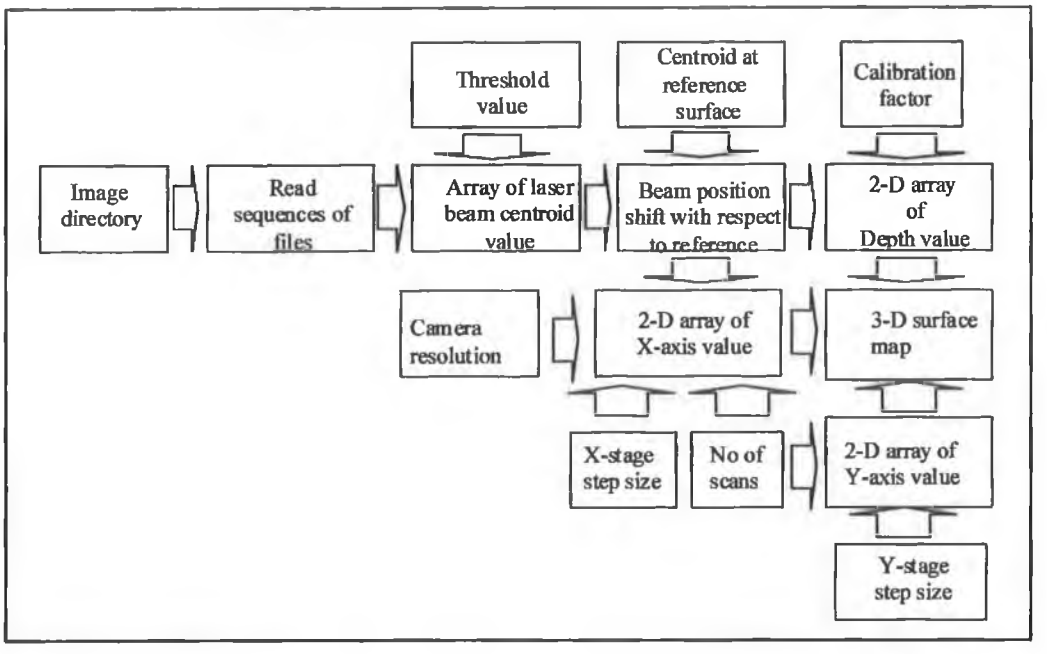

Figure 4.17: Block diagram of the program to generate 3-dimensional surface maps.

Chapter Five

5 Experimental Results

5.1 Introduction

In this chapter results obtained are outlined. Prior to performing experiments to measure surface defects, experiments were carried out to measure the characteristics of the inspection system and the reflectance properties of the different test samples. So the chapter has been divided in various sections.

Measured surface reflectance from the different material samples is presented in section 5.2. Section 5.3 presents the results from the system calibration. Laser beam spot width measurements are shown in section 5.4. Section 5.5 describes the measurement procedure. Finally, in sections 5.6 and 5.7 the results of measured surface details are presented.

5.2 Reflectance Property of the Sample Surfaces

The reflectance of four different sample materials, anodized aluminum, brass, aluminum and stainless steel, were measured. The brass, aluminum and stainless steel samples are shown in the figure 5.1. The reflectance of anodized aluminum from which the XYZ translation stage was made was also measured.

When the laser beam was incident on the surface, it created a bright spot. The CCf15 camera viewed the spot and was used to capture its image in a window of interest (WOI) size of 40x32 pixels. The brightness of the beam spot on the surface was dependent upon the reflectance of the surface and the camera lens aperture. Images of the surfaces were represented by the gray scale intensity values ranging from 0 to 255. Since different sample materials have different reflectivity, the gray scale intensity values of the surfaces were different for different sample materials.

When the laser beam was incident on a surface with a high background brightness value, the contrast between the background surface and the laser spot image was

greatly reduced. The measured intensity of the laser beam was added to the background intensity of the surface. Pixel saturation occurred for intensity values greater than 255.

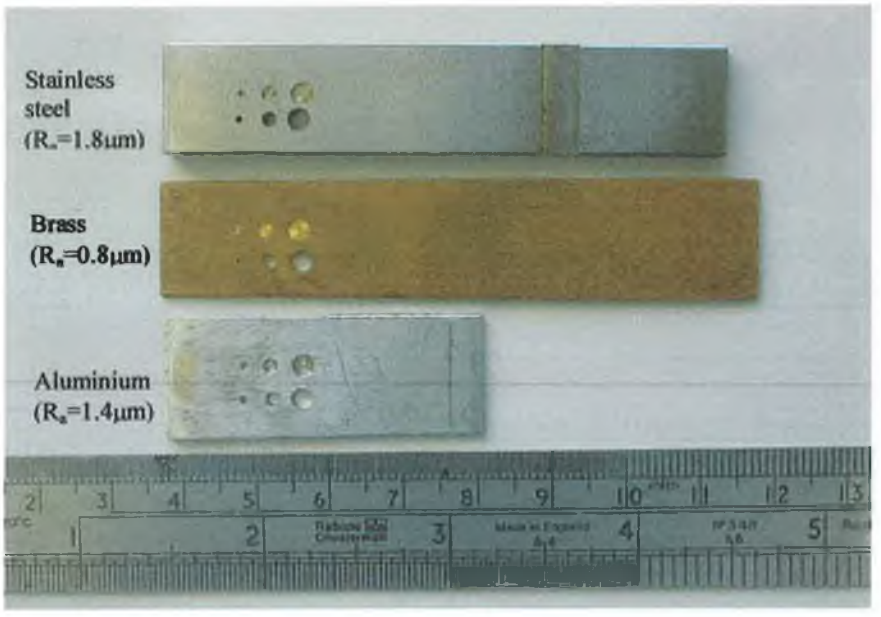

Figure 5.1: Photograph of the sample surfaces.

Gaussian intensity values recorded for the different samples and aperture openings are shown in figures 5.2 to 5.17. Four different materials at four different aperture values of 16,11,8 & 5.6 were used in this experiment.

Figures 5.2 to 5.5 show the beam intensity profile of the laser spot image on an anodized aluminum surface. Figure 5.2 shows the intensity profile with a camera lens aperture 16. The grayscale value of the background surface was between 100-110. Figure 5.3 shows the intensity graph for a lens aperture of 11 and the background grayscale intensity was around 120. Figure 5.4 and figure 5.5 show the intensity graph for aperture of 8 and 5.6 respectively. Background intensities for these settings were found to be about 120 and 130 respectively. The maximum intensity was found to be less than 250 and there was no saturation of the pixels. In the figures 5.2 and 5.3, the intensity profile of the laser beam spot on the anodized aluminum are quite narrow. Intensity profiles of background surfaces vary for the different aperture values. Comparing these figures to figures 5.4 and 5.5, the aperture values decreased and the amount of light passing through the imaging lens increased. The laser spot on the

surface was therefore seen to be brighter and the intensities of the anodized surfaces also increased.

It was seen for all samples that the background intensity values of the surface increased as the aperture of the camera lens were increased from 16 to 5.6. Background intensity values were also seen to increase as the aperture of the camera lens was increased and pixel saturation occurred which could be seen from the graphs in that the peaks of the gaussian intensity profiles are flat. Since the background intensity level increases at higher apertures of the camera lens, the beam spot size was wider, which was the result of the pixel saturation.

Figure 5.6-5.9 show the intensity graphs of the aluminum surface. Figure 5.6 shows the intensity profile of the laser beam spot on the aluminum surfaces at an aperture of 16. From this figure it could be seen that the laser beam spot on the surface spread across the aluminum surface. This graph almost displays the whole gaussian profile and has a small amount of truncation. In figures 5.7-5.9, as the aperture value decreased, intensity of the laser spot on the surface increased and the laser beam spot spreading is more evident on the surface and the peak of the gaussian profile became more truncated. In figure 5.9, peak of the gaussian profile is almost flat.

Figure 5.10-5.13 show the intensity graphs measured from the brass sample surface. As the aperture values change from 16 to 5.6, truncation of the peak of the gaussian profile due to the saturation of pixels is also noticeable, but not to the same extent as was seen for the aluminum surface. Intensities of the surface again increased as the aperture value increased.

Figure 5.14-5.17 show the intensity profiles of stainless steel at different aperture values. The peaks of the gaussian profile are found to be narrow in figure 5.14, 5.15 and 5.16. However, a small amount of truncation of the profile can be seen in figure 5.17. Table 5.1 shows a comparison of the different sample material intensity readings for different camera lens apertures.

Camera aperture	Average Intensity value of Anodized aluminum surface	Average Intensity value of aluminum surface	Average Intensity value of brass surface	Average Intensity value of stain less steel surface
16	100	135	110	85
11	105	150	120	100
8	110	160	130	110
5.6	125	175	150	130

Table 5.1: Comparison of brightness values of different sample materials.

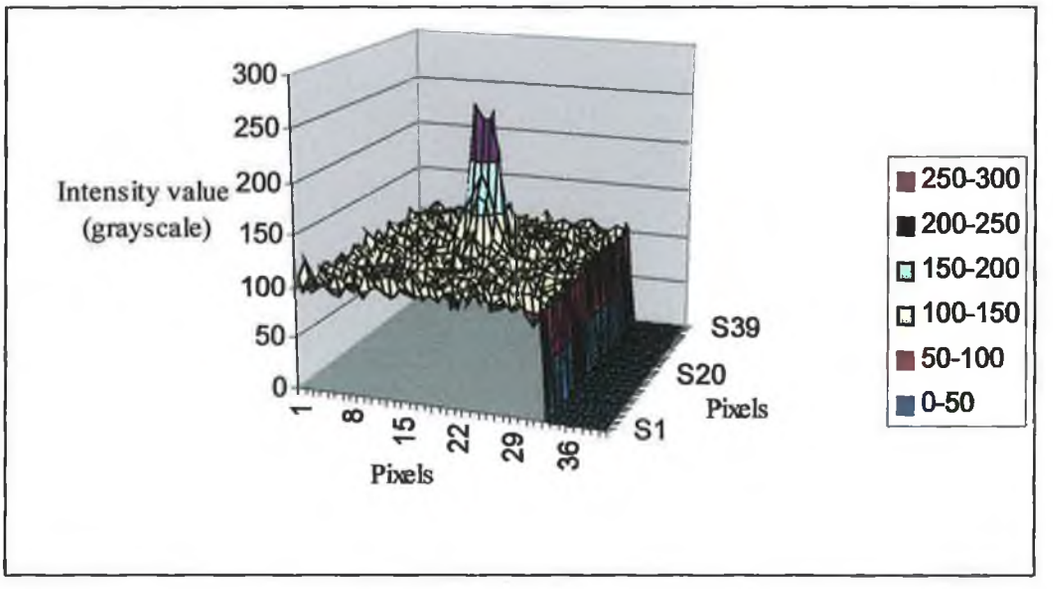

Figure 5.3: Graph of laser spot beam intensity on anodized aluminum surface as captured by camera with aperture 11

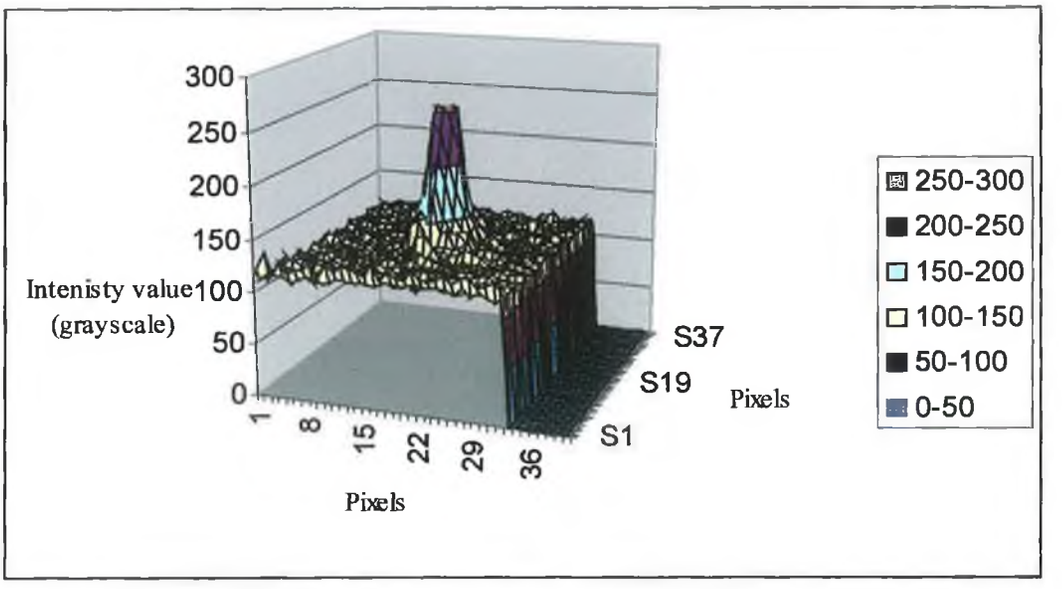

Figure 5.4: Graph of laser spot beam intensity on anodized aluminum surface as captured by camera with aperture 8.

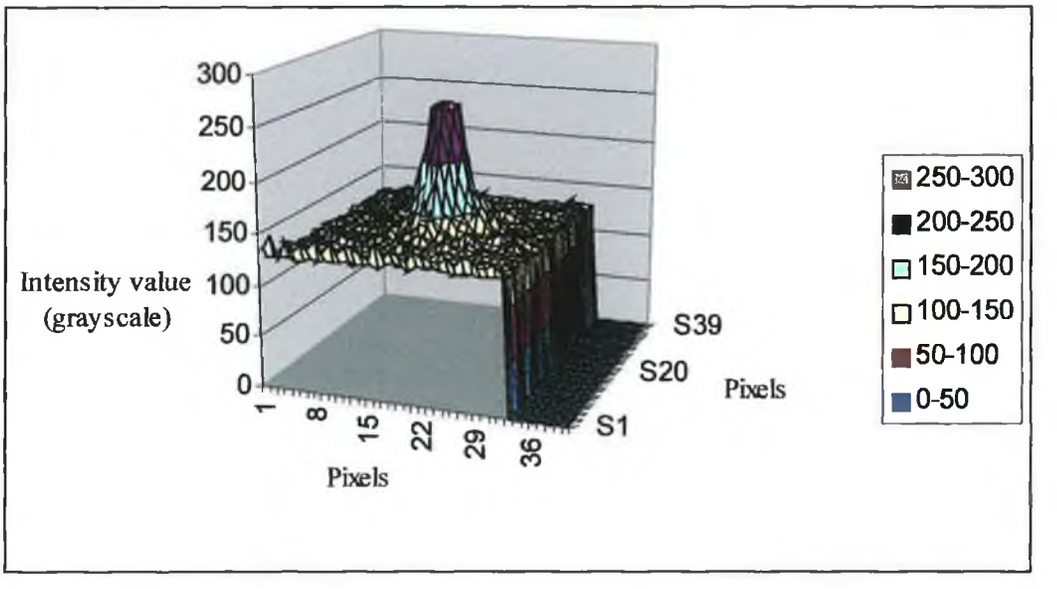

Figure 5.5: Graph of laser spot beam intensity on anodized aluminum surface as captured by camera with aperture 5.6.

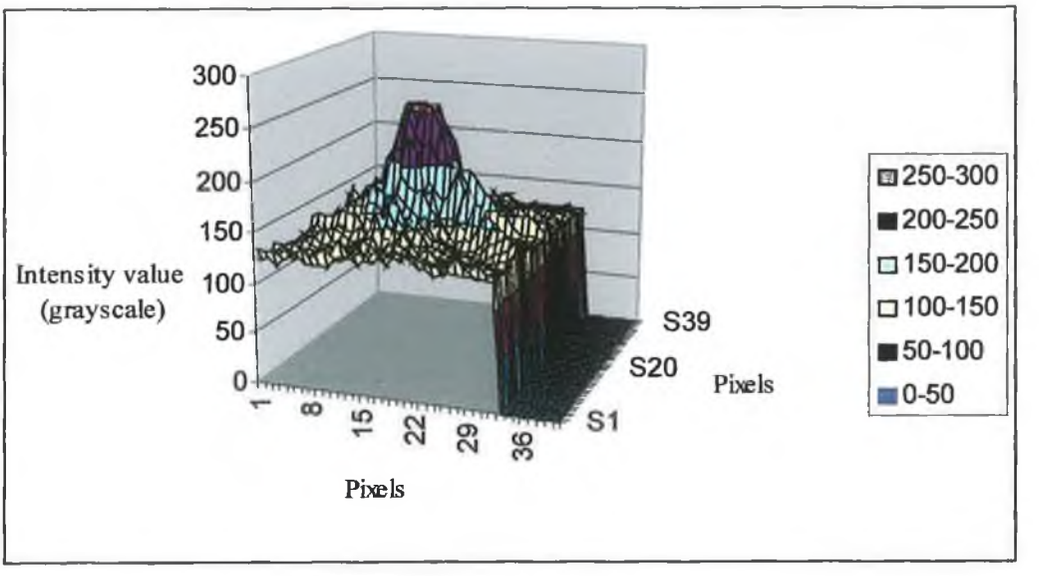

Figure 5.6: Graph of laser spot beam intensity on aluminum surface as captured by camera with aperture 16

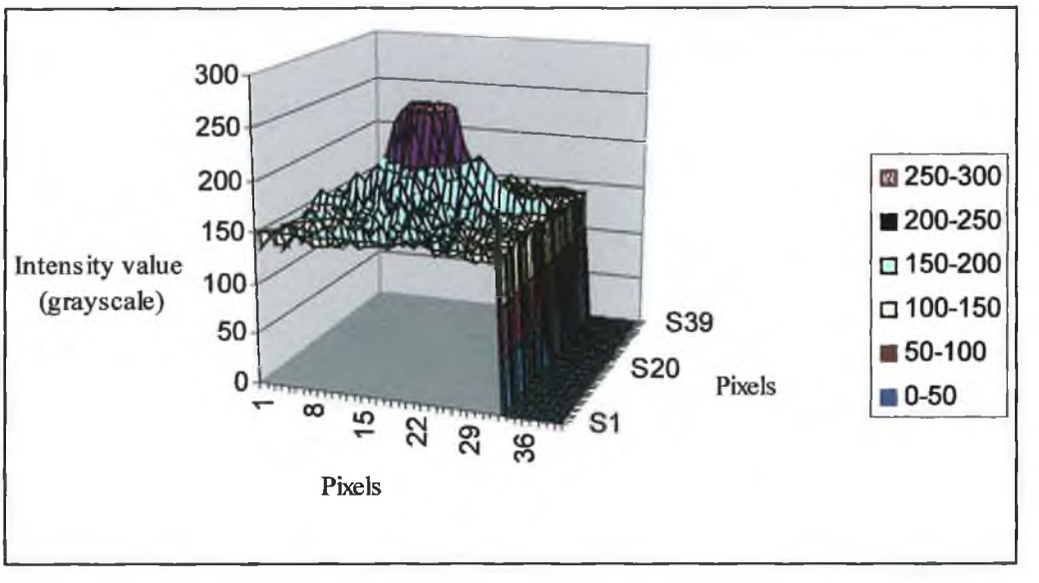

Figure 5.7: Graph of laser spot beam intensity on aluminum surface as captured by camera with aperture 11.

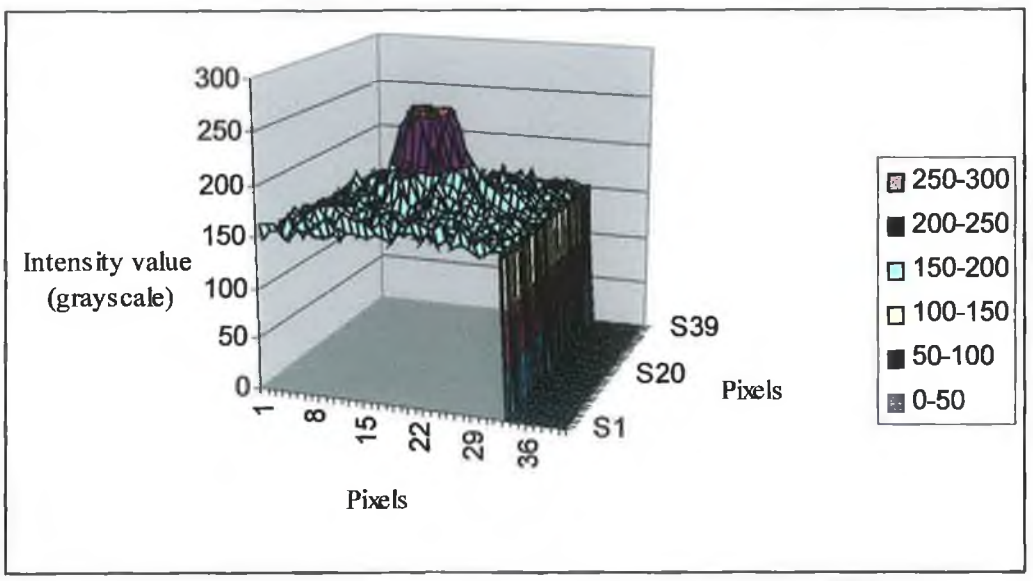

Figure 5.8: Graph of laser spot beam intensity on aluminum surface as captured by camera with aperture 8

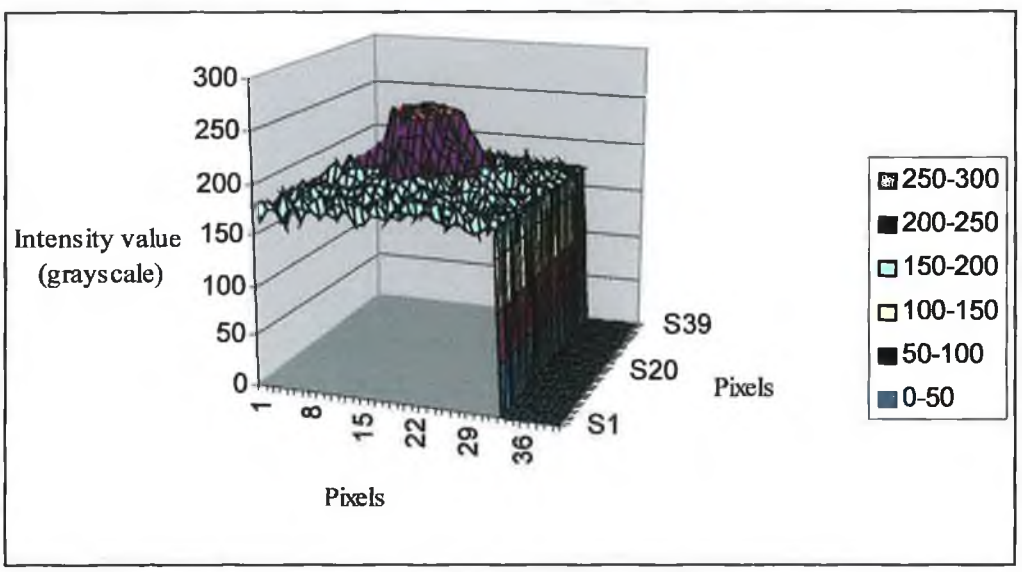

Figure 5.9: Graph of laser spot beam intensity on anodized aluminum surface as captured by camera with aperture 5.6.

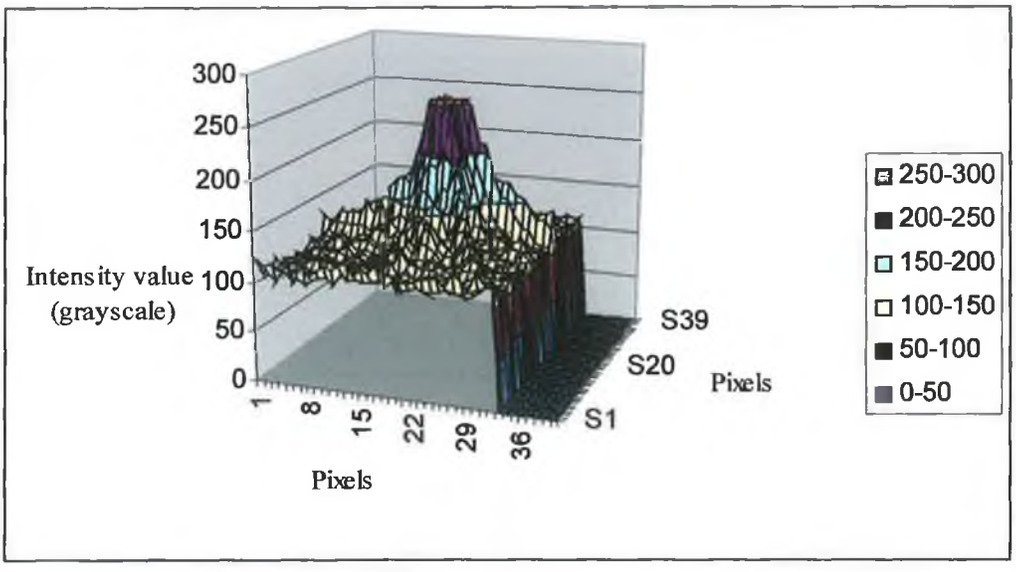

Figure 5.10: Graph of laser spot beam intensity on brass surface as captured by camera with aperture 16.

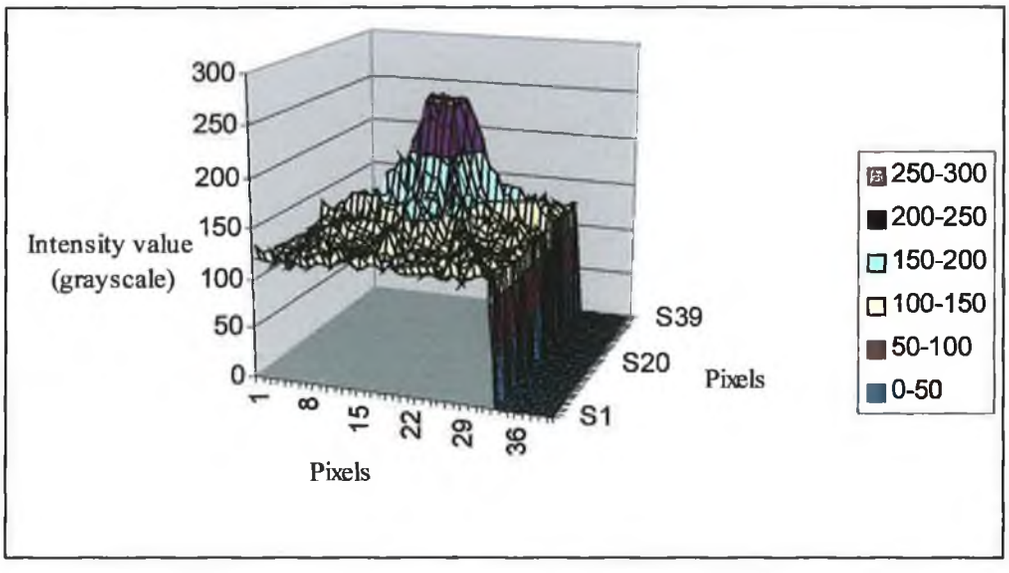

Figure 5.11: Graph of laser spot beam intensity on brass surface as captured by camera with aperture 11.

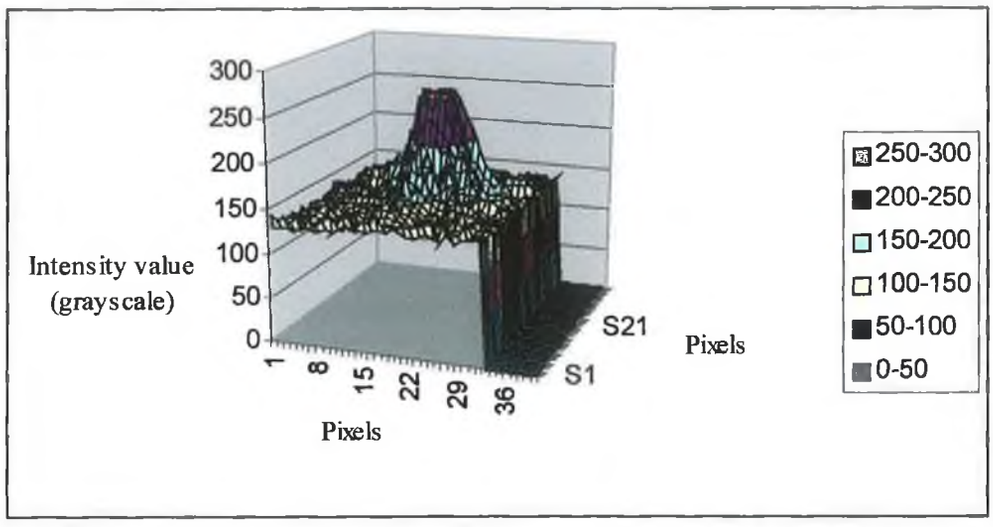

Figure 5.12: Graph of laser spot beam intensity on brass surface as captured by camera with aperture 8.

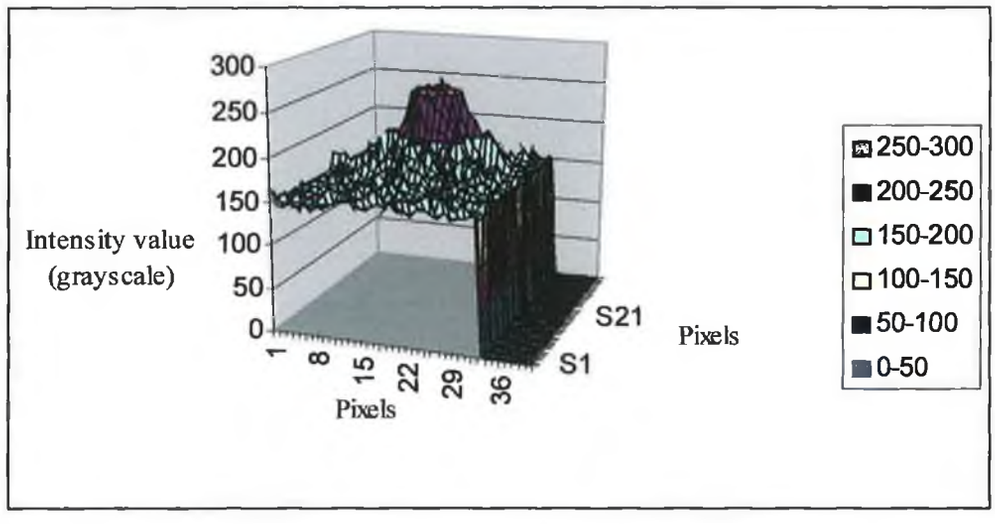

Figure 5.13: Graph of laser spot beam intensity on brass surface as captured by camera with aperture 5.6.

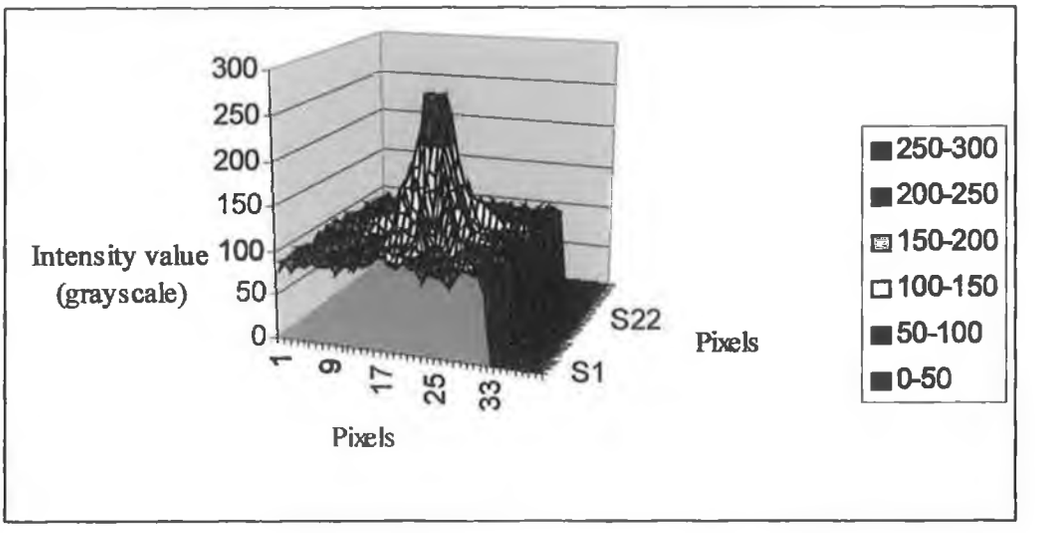

Figure 5.14: Graph of laser spot beam intensity on stainless steel as captured by camera with aperture 16.

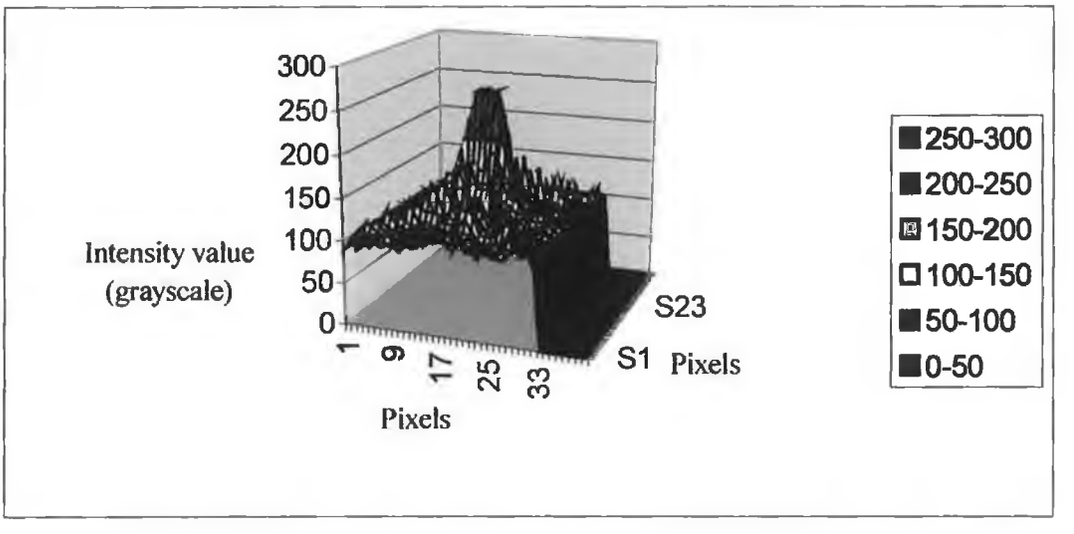

Figure 5.15: Graph of laser spot beam intensity on stainless steel as captured by camera with aperture 11.

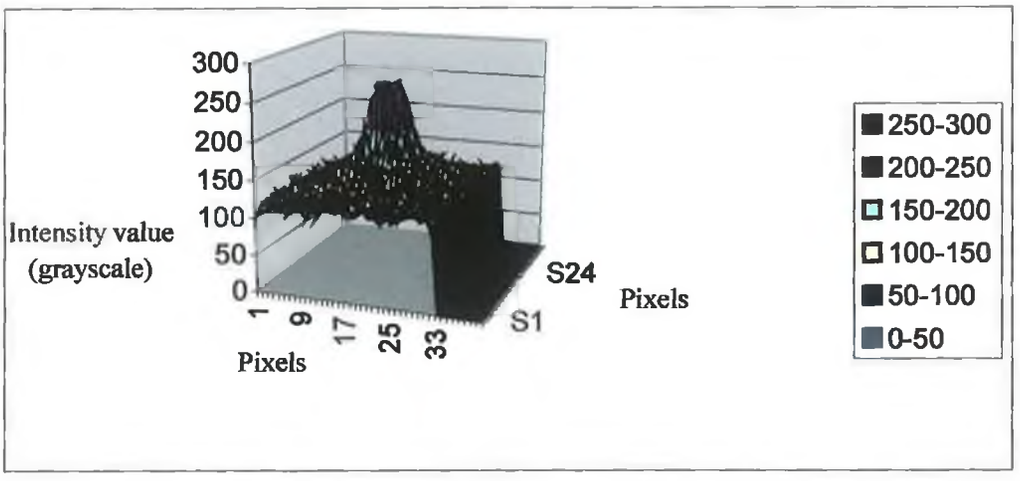

Figure 5.16: Graph of laser spot beam intensity on stainless steel as captured by camera with aperture 8.

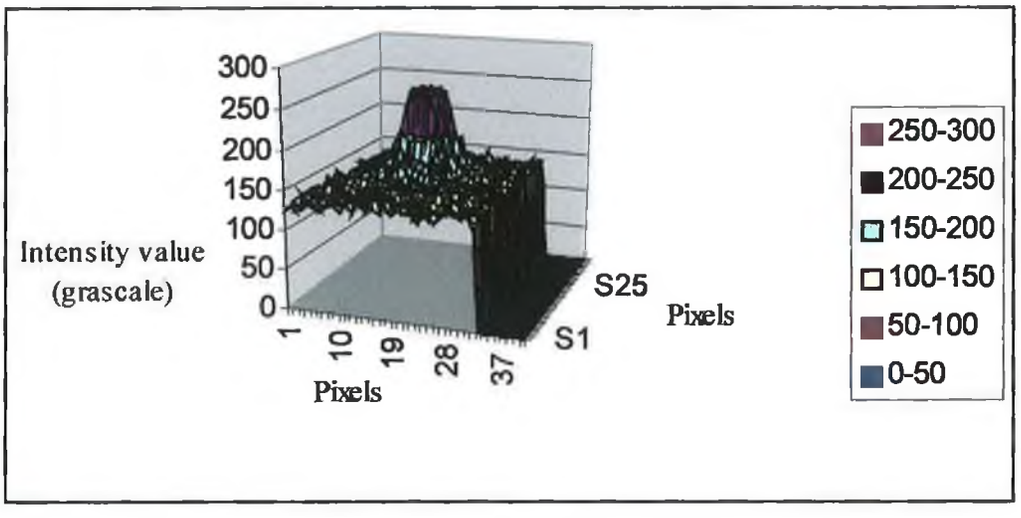

Figure 5.17: Graph of laser spot beam intensity on stainless steel as captured by camera with aperture 5.6.

5.3 Laser Inspection System Calibration

Calibration of the inspection system was required in order to obtain a conversion factor that would determine the vertical dimension of the measured surface resulting from a lateral shift of the laser beam spot as detected by the sensor. The procedure for the system calibration was described in section 3.3.1. The laser beam was incident on the sample held on the X-Y-Z translation stage and the sample was moved along the Z-axis by a constant known increment in order to simulate vertical shift of the sample surface. Image of the spot was recorded every time the Z stage was incremented. The lateral shift of the beam spot on the sensor was recorded every time as the Z stage was incremented.

Four different sets of image files were generated for different increment values of 50μm, 70μm, 100μm and 150μm. These images were then analyzed by the software. While analyzing the files with the software, different threshold values (see section 3.4) were employed in order to eliminate the noises. Threshold values 130, 135, 140, 150, 155 were chosen for suppressing the noise level from the images. Displacement characteristic recorded for different sets of threshold values and Z-stage increment values are shown in figures 5.18-5.27. These graphs illustrate the beam spot shift as seen by the sensor in terms of number of pixels at each vertical displacement. A linear curve fit to the data was employed on each graph from where the conversion factors were obtained. In the figures 5.18-5.21, vertical displacement characteristics are observed for increments of 50μm. It can be seen from these graphs that the laser beam spot does not shift linearly with the fixed 50μm displacement of the surface along the vertical direction. As the threshold value to eliminate the noise level was increased, the curve got much smoother and the values of the conversion factor obtained from the curves decreased. Figure 5.22 shows the vertical displacement characteristic curve for the surface displacement increment of 70μm and threshold value of 135. In the figure 5.23-5.27, the displacement characteristic curves, which have the increment values of 100μm and 150μm respectively, were found to be much smoother. Conversion factors obtained from these results are presented in the table 5.2.

Z-stage increment (μm)	threshold value	Conversion factor (μm /pixel)
50	130	47.17
50	135	46.21
50	140	44.70
50	150	43.93
70	135	44.14
100	130	46.99
100	150	44.33
150	130	55.29
150	150	44.96
150	155	42.47

Table 5.2: Conversion factors at different vertical stage increments and different filter values.

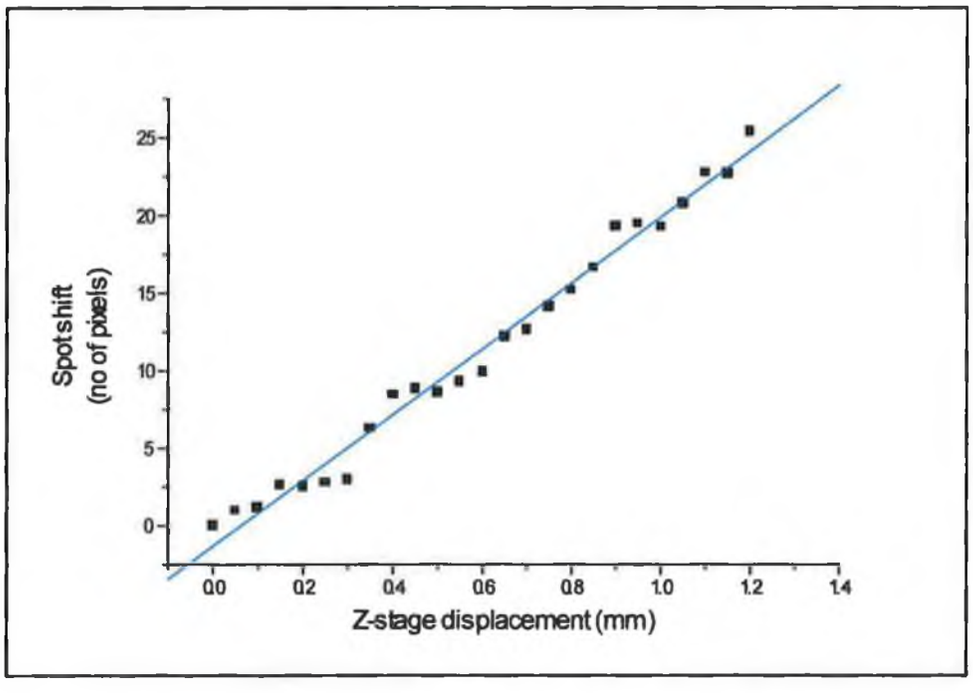

Figure 5.18. Displacement characteristics for Z stage increment of 50μm and a threshold value of 130.

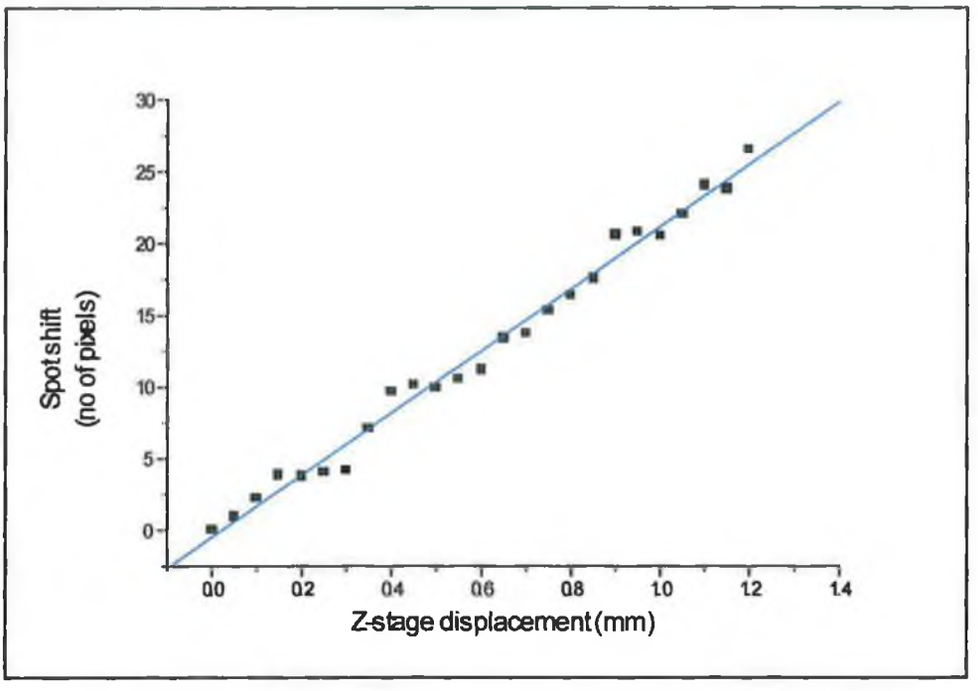

Figure 5.19. Displacement characteristics for Z stage increment of 50μm and a threshold value of 135.

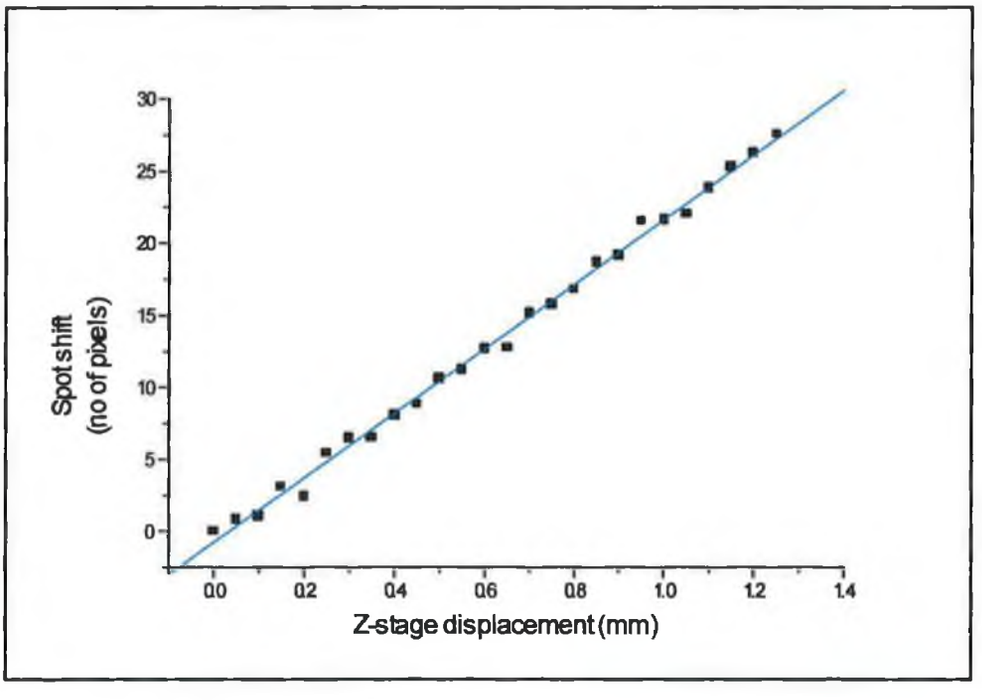

Figure 5.20. Displacement characteristics for Z stage increment of 50μm and a threshold value of 140.

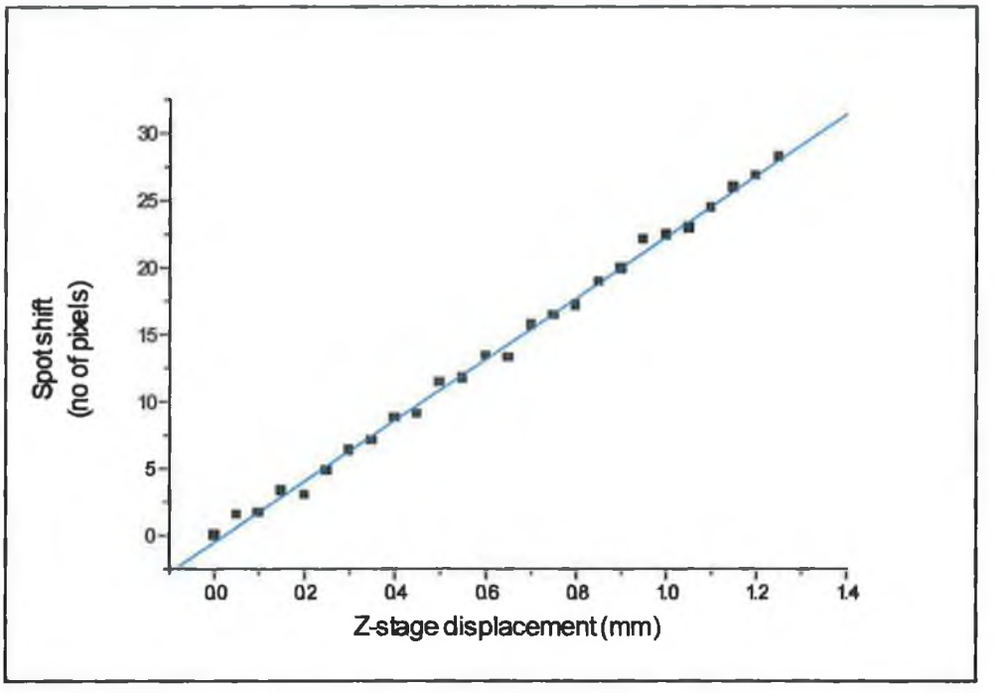

Figure 5.21. Displacement characteristics for Z stage increment of 50μm and a threshold value of 150.

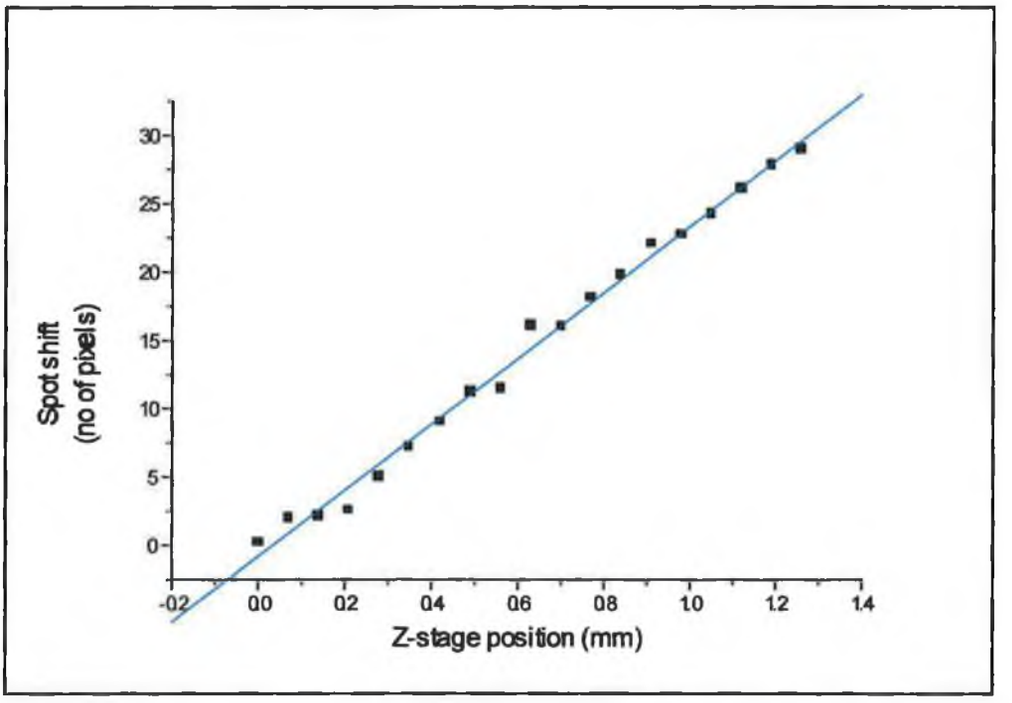

Figure 5.22. Displacement characteristics for Z stage increment of 70μm and a threshold value of 135.

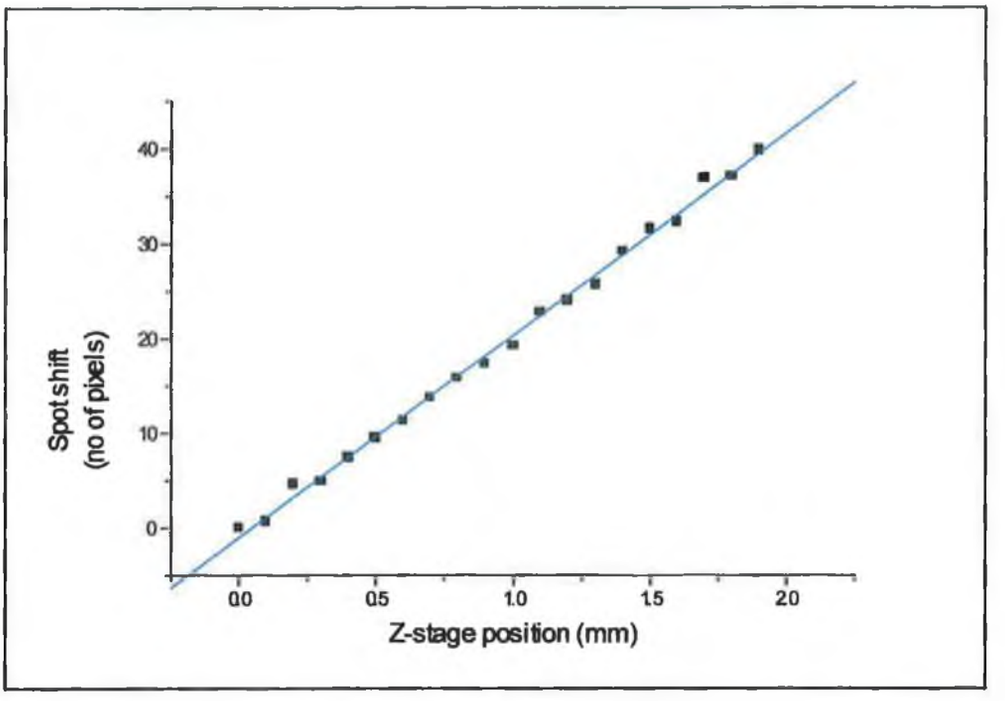

Figure 5.23. Displacement characteristics for Z stage increment of 100μm and a threshold value of 130.

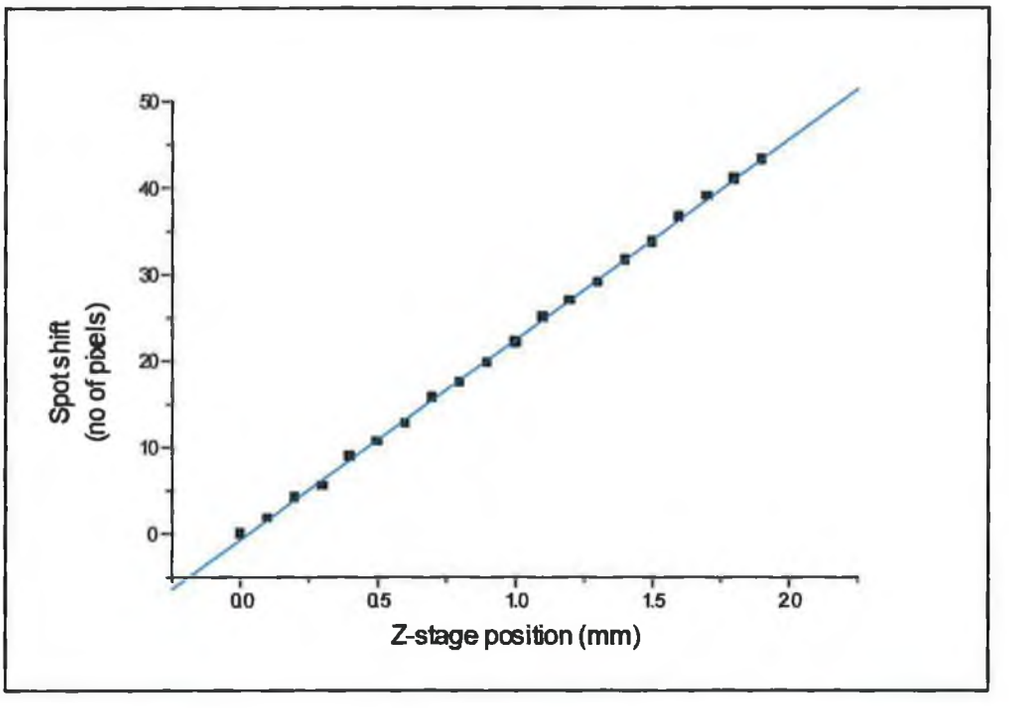

Figure 5.24. Displacement characteristics for Z stage increment of 100μm and a threshold value of 150.

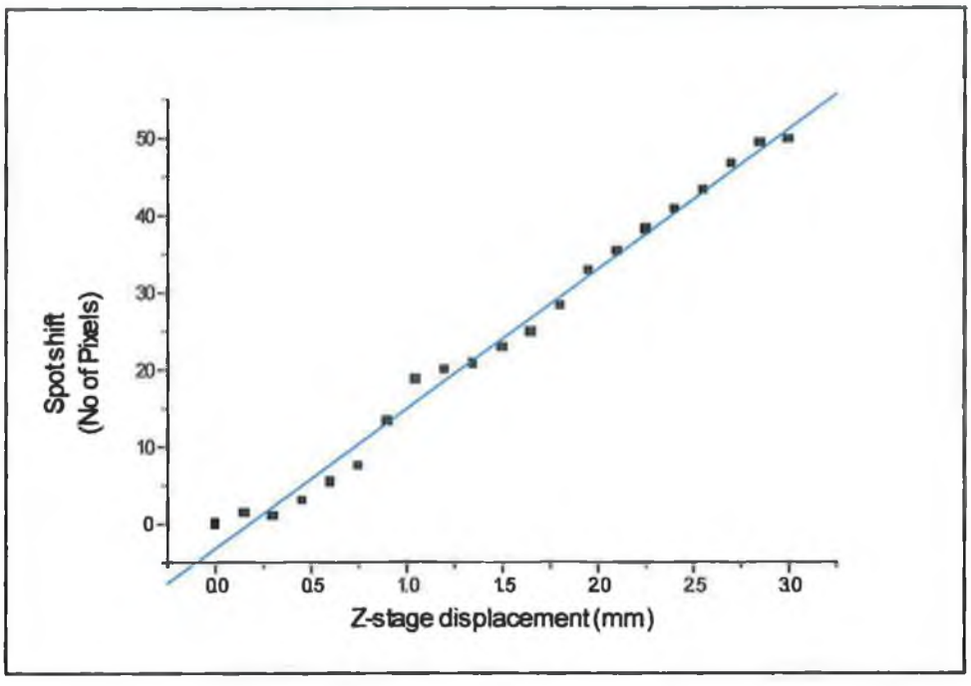

Figure 5.25. Displacement characteristics for Z stage increment of 150μm and a threshold value of 130.

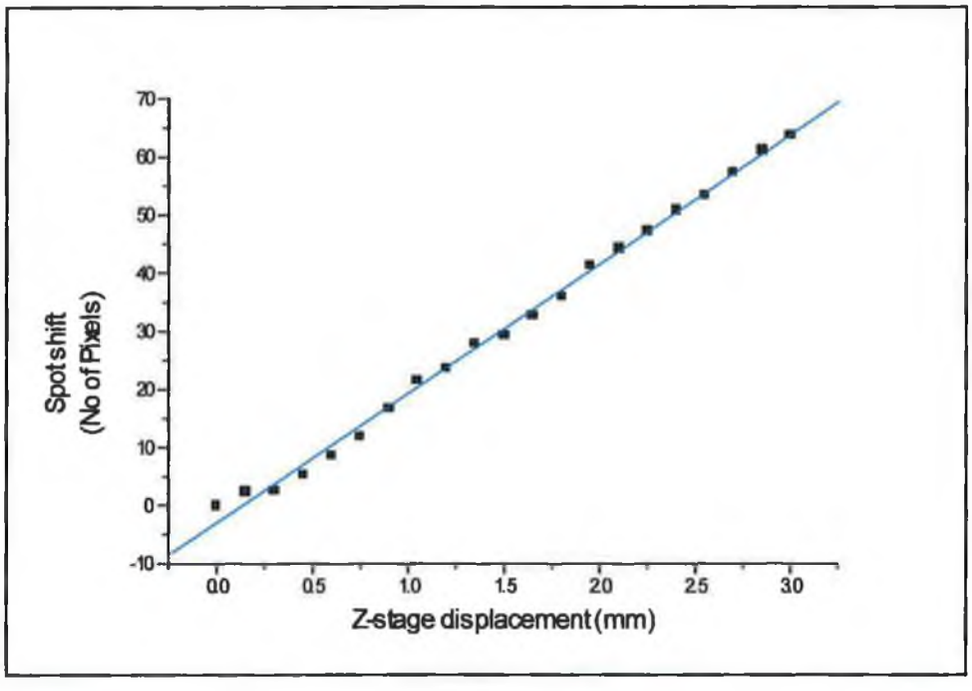

Figure 5.26. Displacement characteristics for Z stage increment of 150μm and a threshold value of 150.

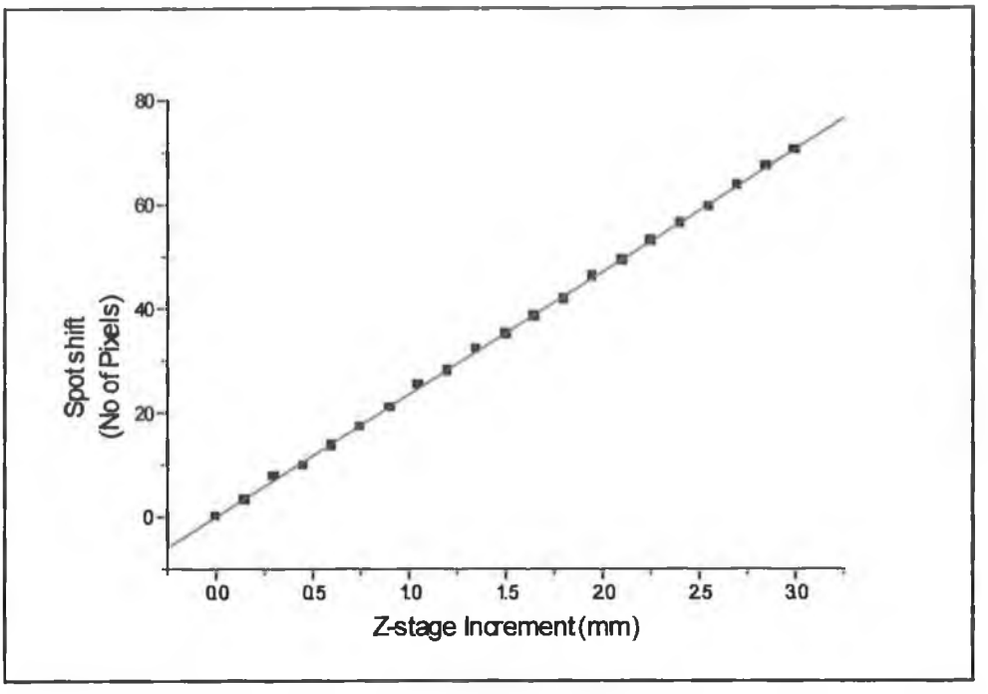

Figure 5.27. Displacement characteristics for Z stage increment of 150μm and a threshold value of 155.

5.4 Laser Beam Spot Size Determination

Figures 5.29 to 5.31 show the results of the experiments carried out to measure the laser beam spot width. This experiment was intended to determine the lateral resolution of the system. In section 3.2.3, it was defined that the systems lateral resolution is the measure of the beam spot size. The experiment follows the knife-edge method [94] for laser beam width determination. The sample for this experiment was prepared by removing material from the stainless steel plate so as to create two different surface levels. A sharp vertical edge was thereby formed between the two levels. The laser beam was swept across the sample by an increment of 10μm along X-axis direction.

Figure 5.28 shows the measurement procedure. The laser beam fell obliquely onto the higher surface level and after being reflected off the surface was detected by the camera (figure 5.28 (a)). The one dimensional centroid position of the reflected laser

beam was calculated in terms of the number of pixels from any arbitrary position of the array sensor. The centroid position is shown in this figure with a dot.

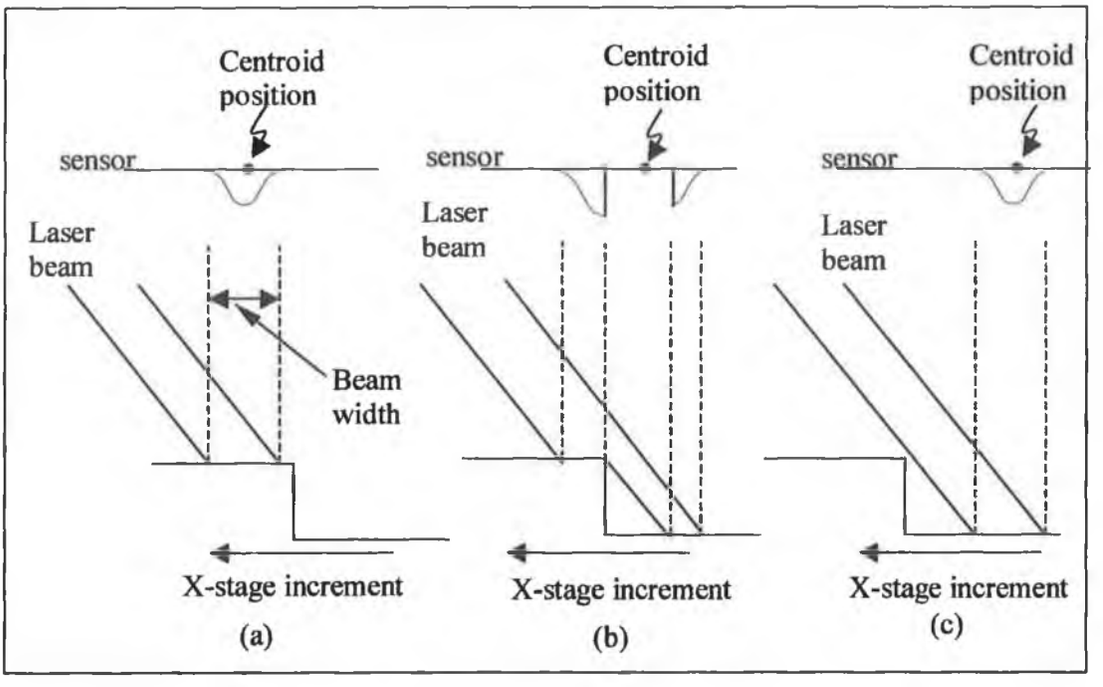

Figure 5.28: Laser beam spot on (a) the higher surface level (b) both surface levels and (c) the lower surface level.

In figure 5.28 (b), when the X-stage was incremented, the laser beam spot swept across the surface and fell on both the surface levels as the beam split up. Beam centroid position was shifted with respect to the figure 5.28 (a). In figure 5.28 (c) laser beam spot fell completely on the lower surface level and the centroid position shifted further along the sensor to the right. So as long as the laser beam fell on any of the surface levels, the centroid position was fixed on the sensor for that surface level and a transition occurred when it went from one level to another. It was required to move the translation stage, at least, a distance equal to the beam width to enable the laser beam fell completely from one level to another level. This increment was recorded as the beam width of the laser spot onto the surface.

The following three graphs (figure 5.29-5.31) were taken from three experiments at different positions in the sample. The square points were from the original data values and the circular points were obtained by smoothing the original data values using three-point averaging. In figure 5.29, on the left side of the curve, as long as the laser

beam spot fell on the higher surface level, the centroid position value remained almost constant. However, the centroid position values from the other surface level are not constant. Instead centroid positions were shifting slightly as the X-stage incremented. In these figures, two vertical lines are drawn to roughly show the beam spot width. The vertical line on the left in the figures marks the position of the edge of the knife where the laser beam spot just started to split on it. The vertical line on the right indicates that the laser beam spot has just past the knife-edge completely.

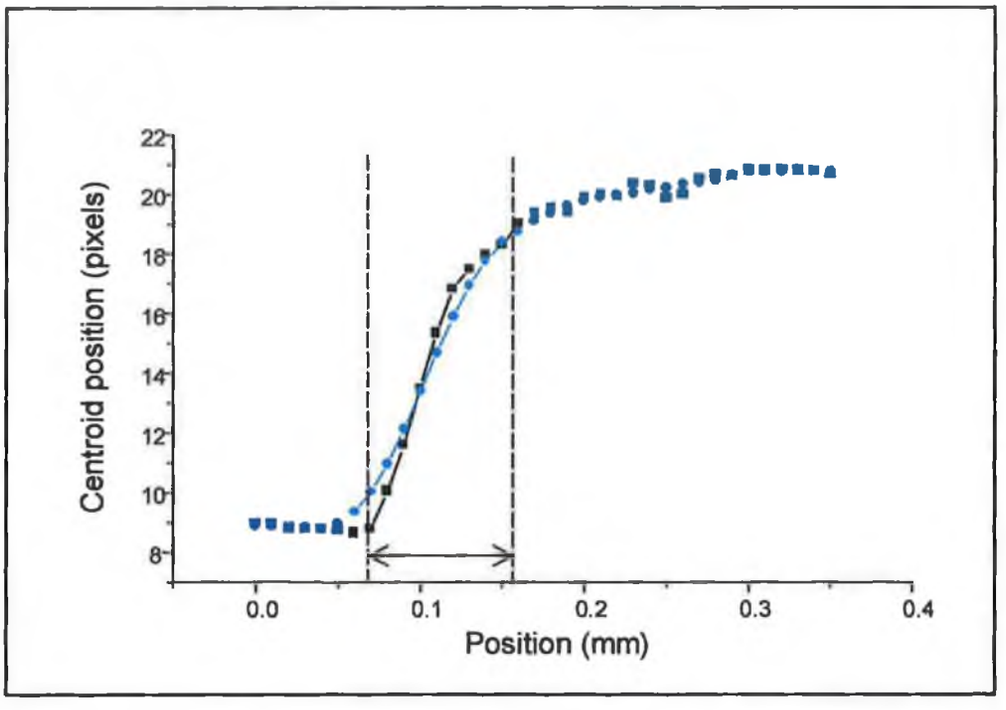

Figure 5.29: Graph of the 1-D centroid positions obtained when scanning across a knife-edge with two surface levels.

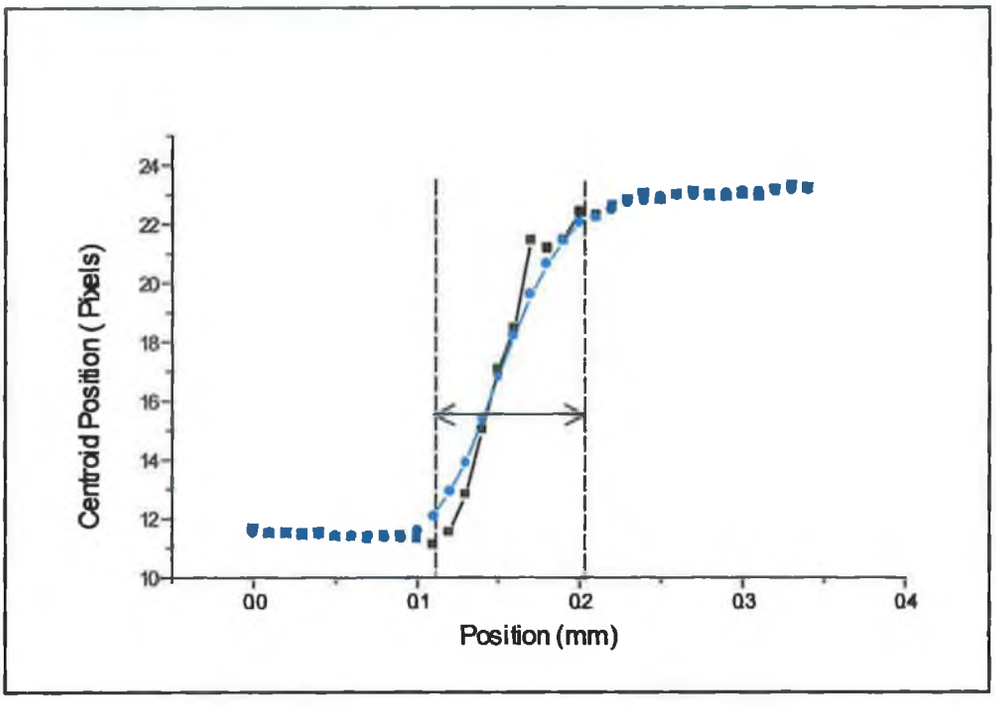

Figure 5.30: Graph of the 1-D centroid positions obtained when scanning across a knife-edge with two surface levels.

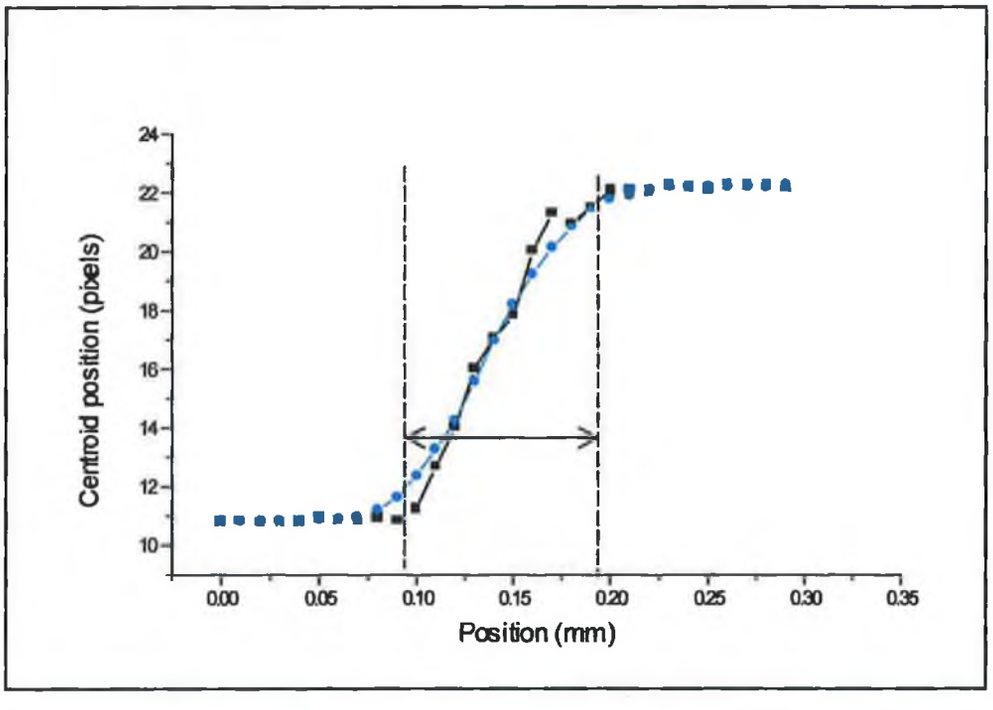

Figure 5.31: Graph of the 1-D centroid positions obtained when scanning across a knife-edge with two surface levels.

5.5 Scanning Procedure

The scanning procedure of the sample surface using the developed inspection system is explained in figure 5.32. In order to carry out the scanning of the sample surface, initially the relevant sample part was mounted on the XYZ translation stage and was held tight against the faceplate of the translation stage. The particular area on the plate to be scanned was positioned carefully so that the laser beam was incident at the starting position of the area. Scanning was initially performed by incrementing the X-translation stage by a particular step size while keeping the Y and Z stage position constant. Every time the X-stage was displaced, the image of the surface was recorded and saved. Once the displacements along X direction were finished, the sample part was brought back to the position from where the scanning had been started. Then the Y-stage was incremented by a certain step size and the next X direction scan started. As seen in the figure the scanning was performed always in one direction.

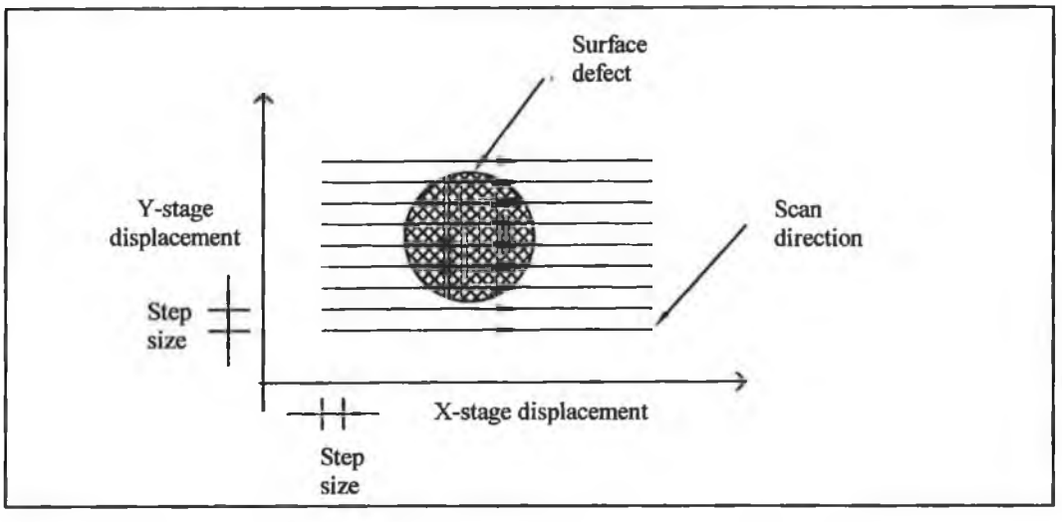

Figure 5.32: Scanning procedure of the sample surface.

5.6 Preliminary Scan Results

Preliminary scanning was performed to observe the performance of the inspection system with surface defects of known sizes and shapes. Three different materials with three blind holes of different size (1mm, 2mm, and 3mm) and hole depths of about 0.6 mm were used as sample parts (see figure 5.1). The developed laser inspection system was used to scan the blind holes on plates of the following materials: brass, stainless

steel and aluminium. The following two sections describe the results for two-dimensional and three-dimensional scanning of surfaces of the materials used.

5.6.1 Two Dimension Surface Scan Results

Figures 5.33 to 5.44 show the results obtained from the scanning the different sample surfaces in one dimension. These graphs show vertical (Z-axis) and lateral (X-axis) displacement characteristics of the sample parts along the direction of scan (X-axis). Scanning in one dimension generates height values for the corresponding X co-ordinates. These results were obtained using the software whose block diagram was shown in figure 4.16. The graphs here show the results for scanning the plain surface with no defects as well as blind holes taken here to represent defects.

In these graphs (figure 5.33-5.44), the Y-axis illustrates the depth measurement in millimeters and the X-axis shows the amount of displacements in millimeters. Scanning was done in steps of 100μm. Each graph measures the depth of each hole and the width of the hole in millimeter. For the same hole on the sample plate the overall depth measurement across that hole could be obtained from any of the graphs. However, for the scan to inform as to the diameter of the hole, the scan must be taken across the center of the hole. Therefore, scans taken across different sectors of the circle that did not pass through the center resulted in hole sizes that are smaller than the actual diameter.

In the figures 5.33, 5.37 and 5.41, two-dimensional scan results obtained from the defect free plane surfaces of aluminum, stainless steel and brass respectively. It could be seen that the height measurement points increase on the right side of the graph. This tilt indicates a small amount of tilt of the XYZ translation stage on which the sample parts were mounted.

In the graphs obtained by scanning across the holes of different sizes on different sample materials, it can be clearly observed that the diameters of the holes decrease gradually from the open end of the holes to the base surface. The reason for the hole diameter variations is due to the shadow affect of the triangulation system and is

discussed in detail in chapter six. Actual diameter of each hole from the graph can be determined by measuring the width of the two vertical lines as shown in these figures. In these figures, the diameters of the hole are slightly less than the actual diameters of the holes as the scans were performed not exactly along a diameter of the holes.

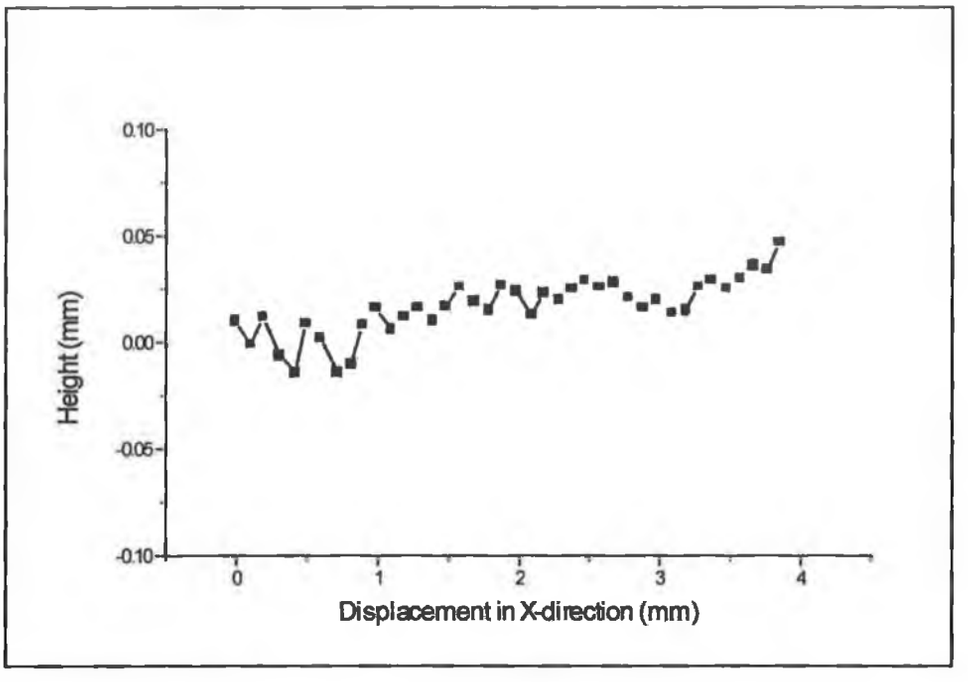

Figure 5.33: Graph of results for scanning aluminum sample without any defects.

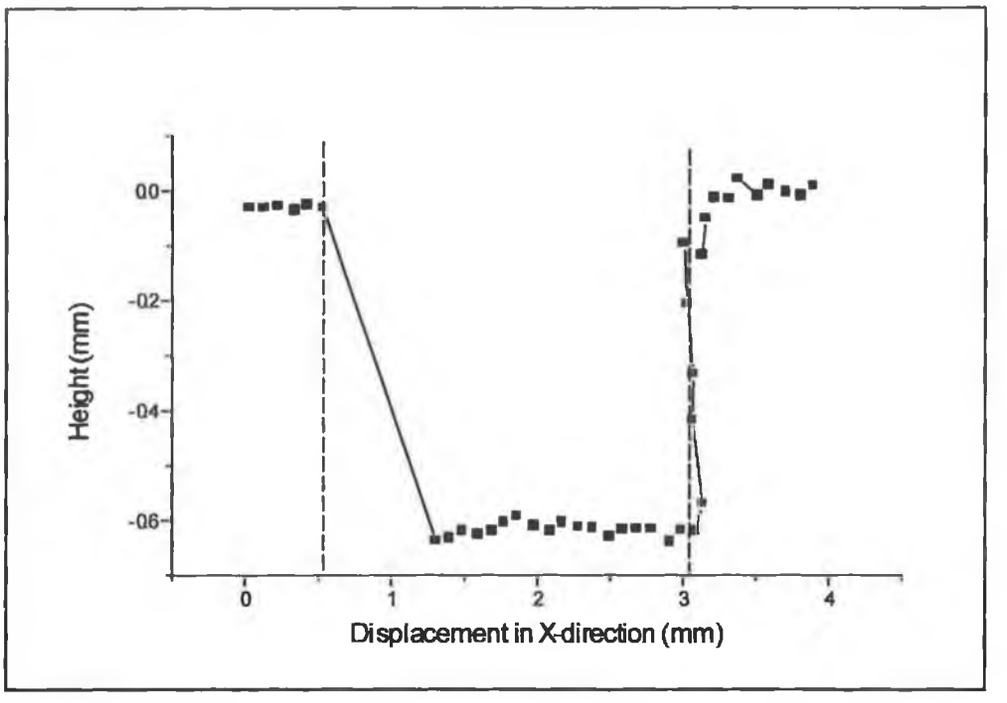

Figure 5.34: Graph of results for scanning aluminum surface with the biggest blind hole. (diameter 3 mm, depth 0.6 mm)

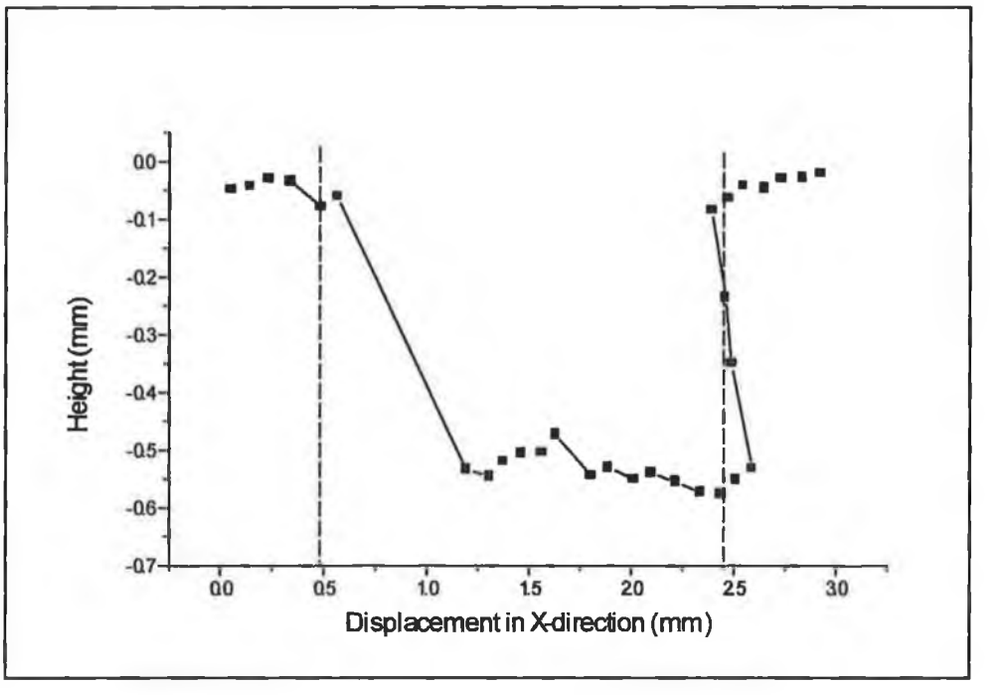

Figure 5.35: Graph of results for scanning aluminum surface with the medium size blind hole. (diameter 2 mm, depth 0.6 mm)

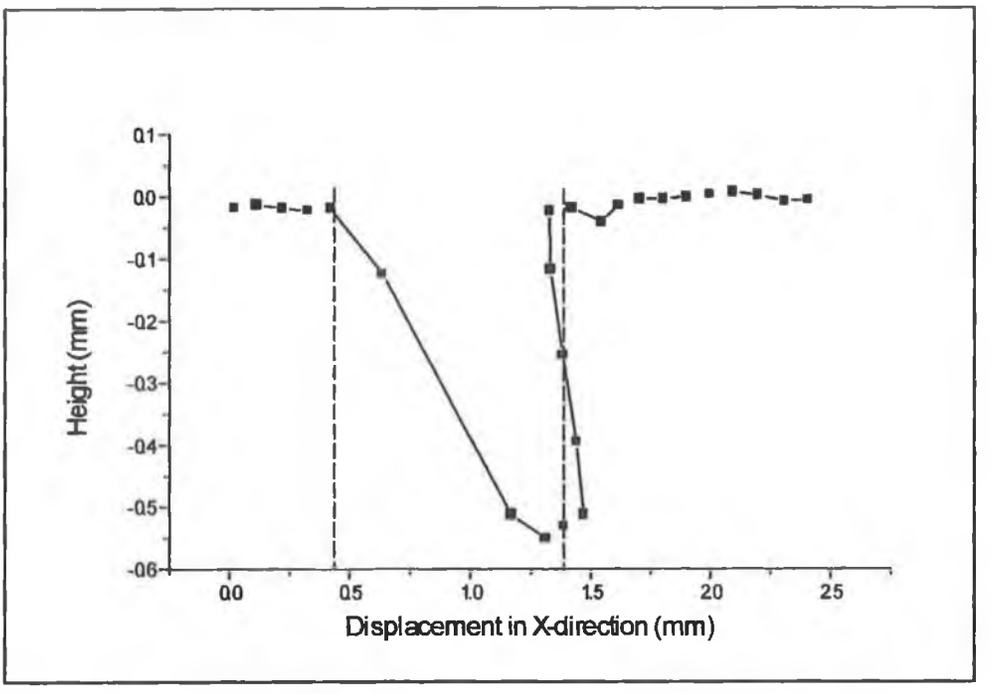

Figure 5.36: Graph of results for scanning aluminum surface with the smallest blind hole. (diameter 1 mm, depth 0.6 mm)

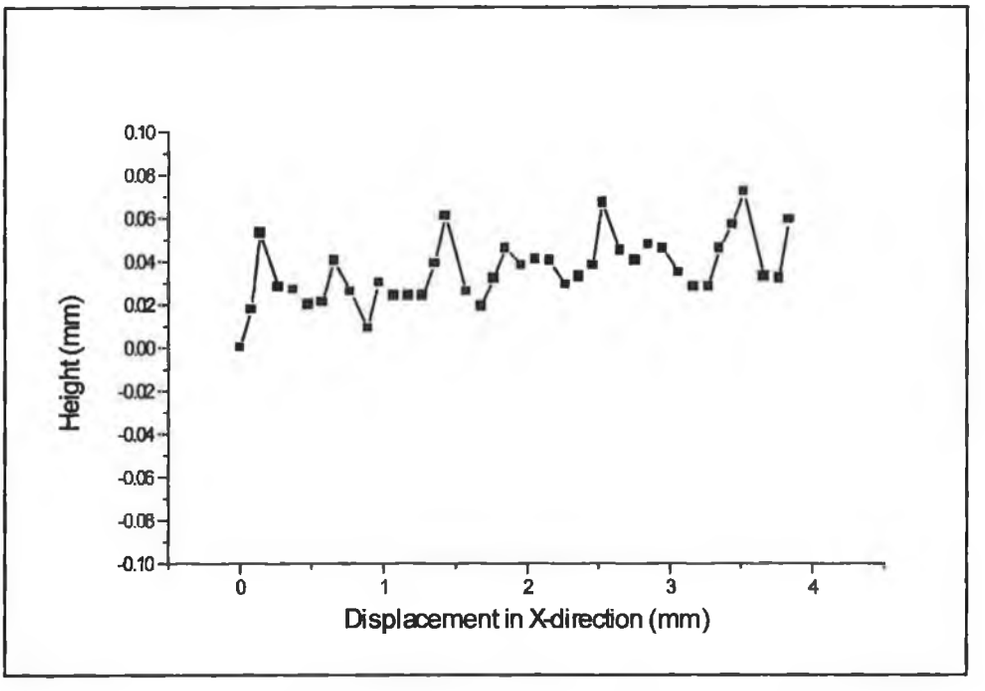

Figure 5.37: Graph of results for scanning stainless steel surface without any defects.

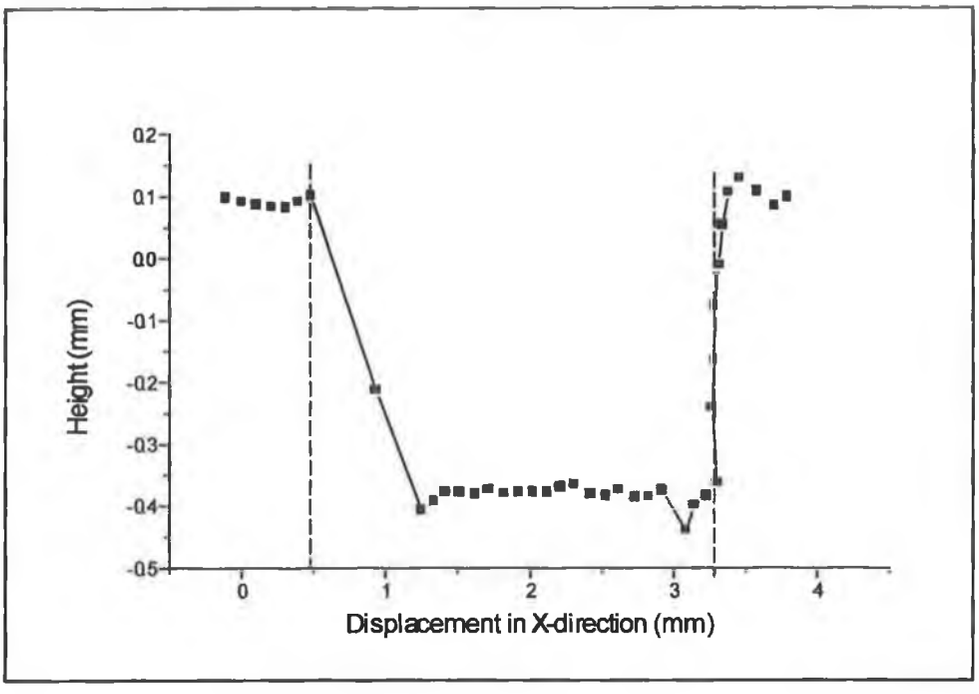

Figure 5.38: Graph of results for scanning stainless steel surface with the biggest blind hole. (diameter 3 mm, depth 0.6 mm)

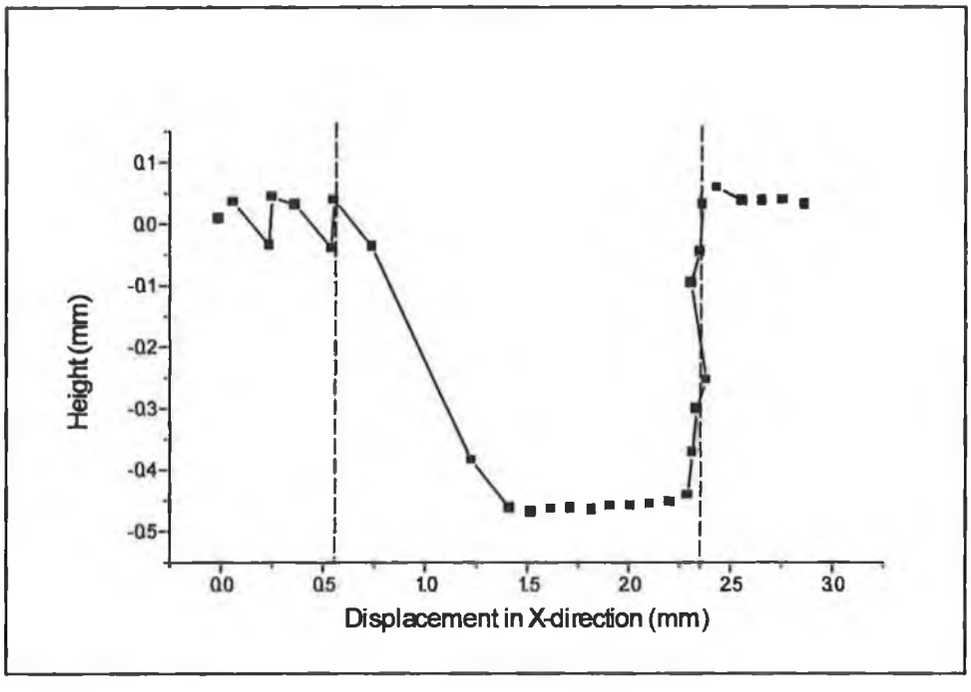

Figure 5.39: Graph of results for scanning stainless steel surface with the medium size blind hole. (diameter 2 mm, depth 0.6 mm)

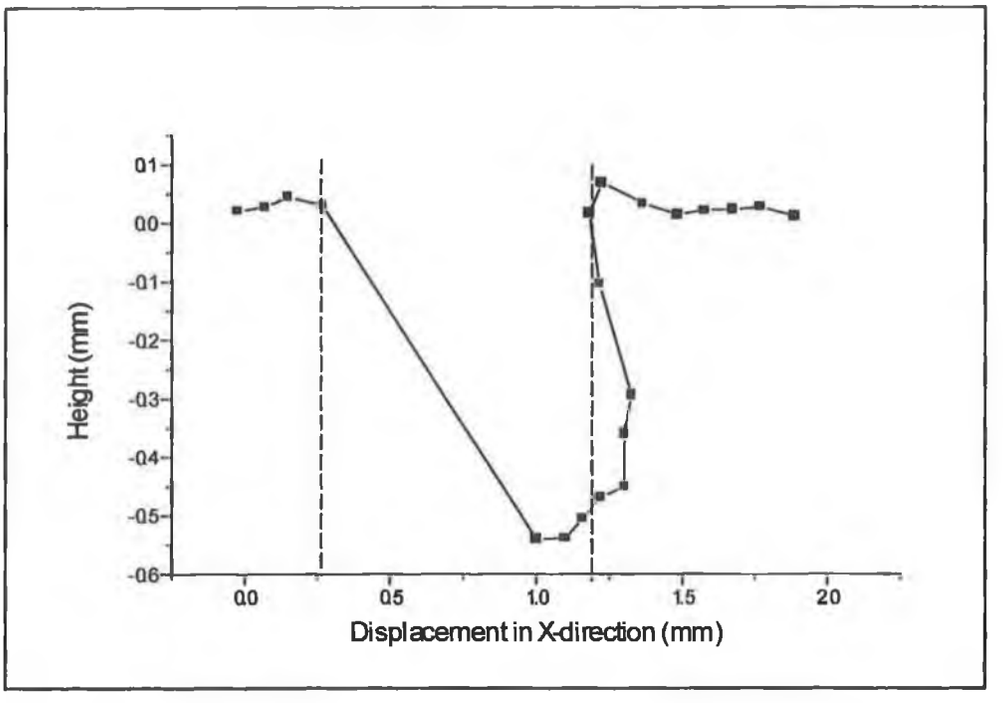

Figure 5.40: Graph of results for scanning stainless steel surface with the smallest blind hole. (diameter 1 mm, depth 0.6 mm)

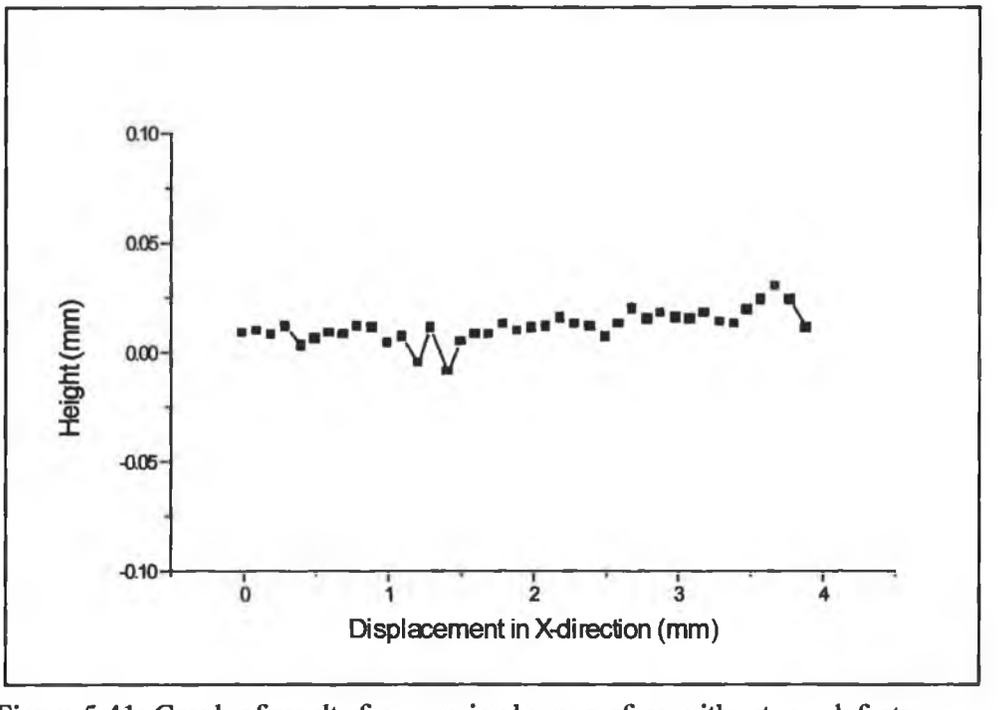

Figure 5.41: Graph of results for scanning brass surface without any defects.

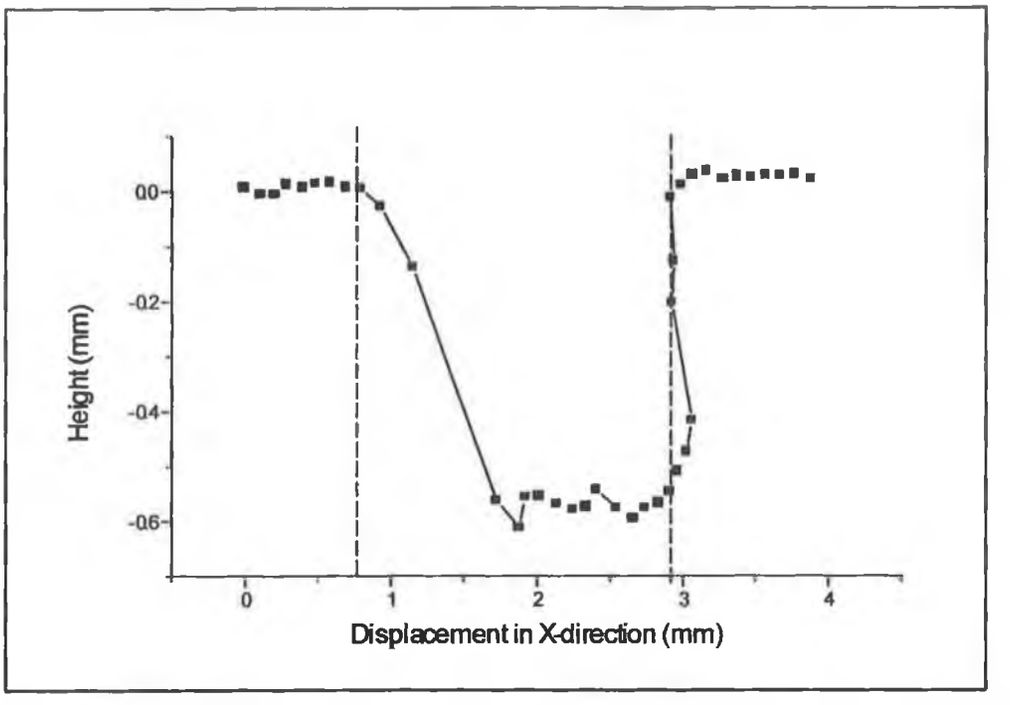

Figure 5.42: Graph of results for scanning brass surface with the biggest blind hole. (diameter 3 mm, depth 0.6 mm)

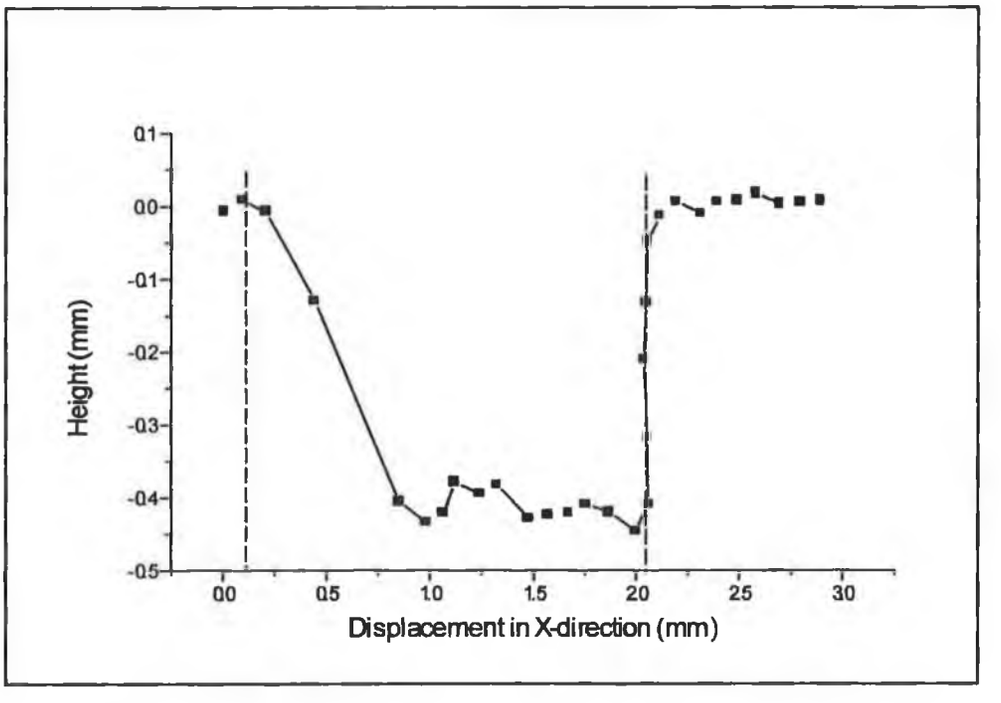

Figure 5.43: Graph of results for scanning brass surface with the medium size blind hole. (diameter 2 mm, depth 0.6 mm)

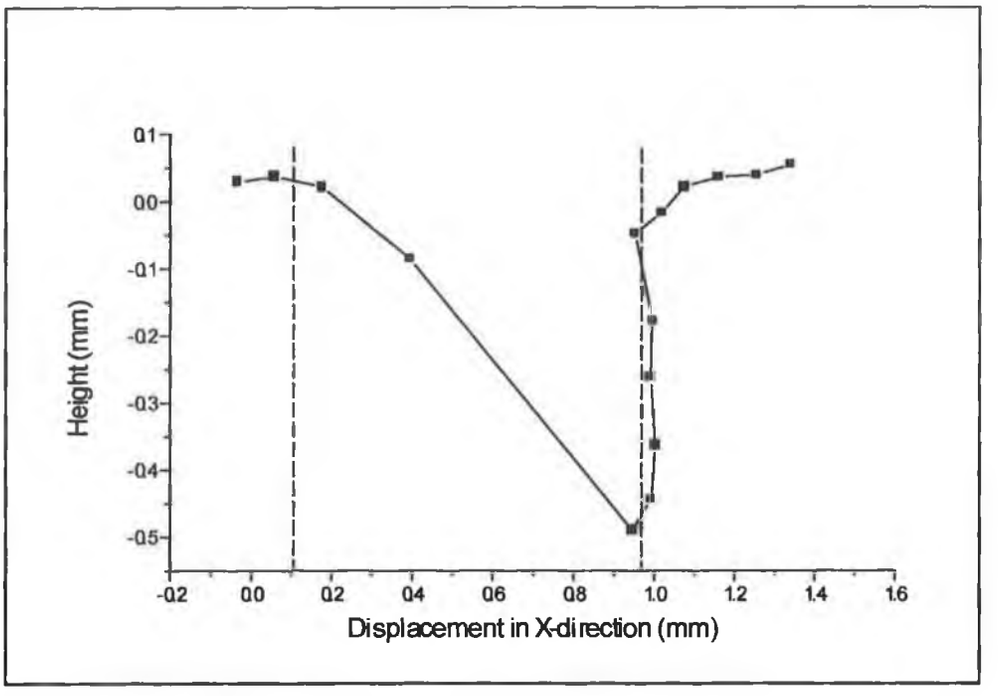

Figure 5.44: Graph of results for scanning brass surface with the smallest blind hole. (diameter 1 mm, depth 0.6 mm)

5.6.2 Three-Dimensional Surface Scan Results

The three-dimensional surface scans produced three-dimensional topographic maps of the surfaces. Three-dimensional mapping of the surface was obtained by compiling the X, Y and Z (depth) co-ordinates, which had been generated by scanning over the sample plate. The algorithm shown in figure 4.17 was employed to generate these three-dimensional maps. The three-dimensional graphical image of the scanned sample plate was plotted using the 3D-graph object in LabVIEW software. This enabled rotation of the graph so that it could be viewed from different positions.

Three-dimensional inspection of the surfaces was carried out on the three sample materials: brass, aluminum and stainless steel (see figure 5.1). Results from one sample material are presented here. The surface maps shown in figures 5.45 to 5.51 are the results obtained from the scanning of the brass plate. Four different three-dimensional surface maps were generated, one of the plain surface without any defects, and the three others from the three different sizes of blind holes. Each blind hole was represented by two surface maps shown from two different positions. One

position provides a pure three-dimensional view and the other position was selected to show two-dimensional surface map displaying only the X and Y-axis of the surface (top view of 3-D surface map). This view would give a clear picture about the diameter of each hole.

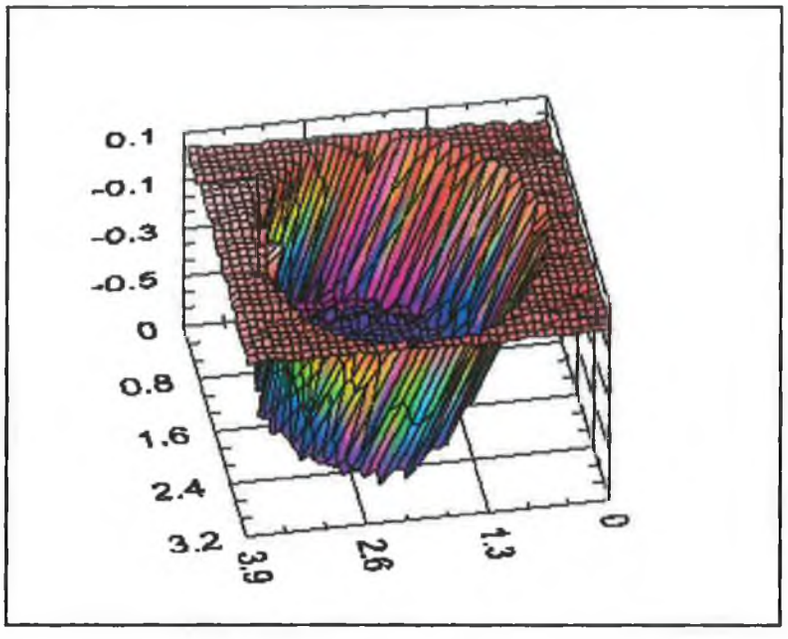

Figure 5.45: 3-D maps of the brass sample surface with the biggest size hole. (diameter 3 mm, depth 0.6 mm)

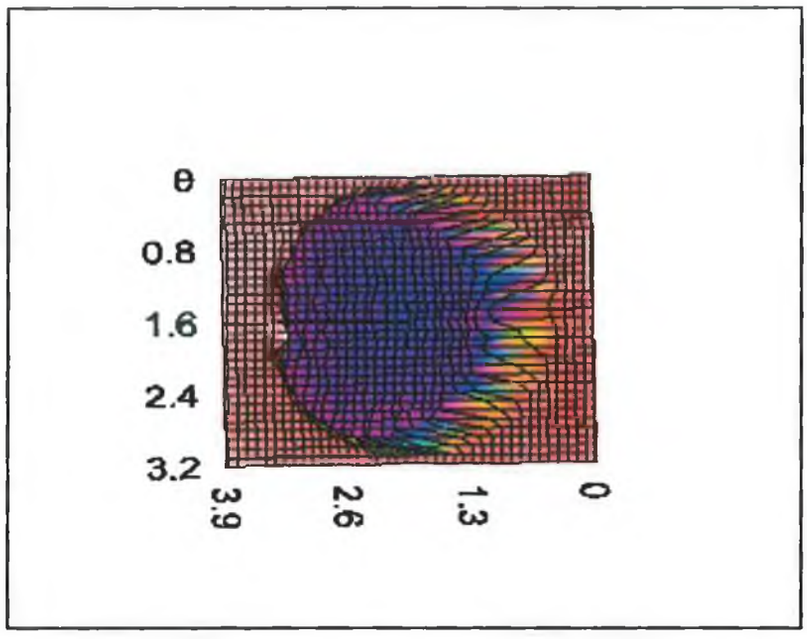

Figure 5.46: 3-D maps of the brass sample surface with the biggest size hole. (diameter 3 mm, depth 0.6 mm)

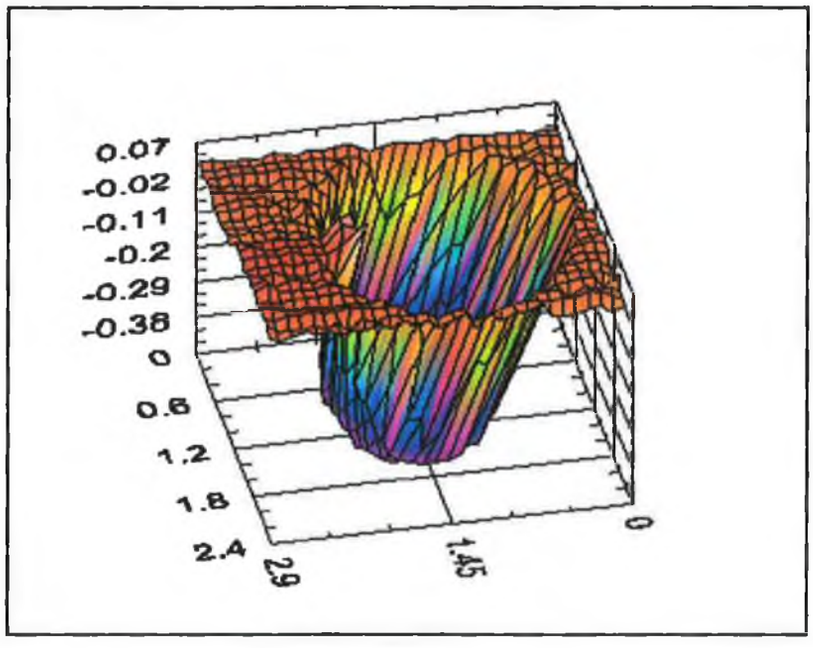

Figure 5.47: 3-D maps of the brass sample surface with the medium size hole. (diameter 2 mm, depth 0.6 mm)

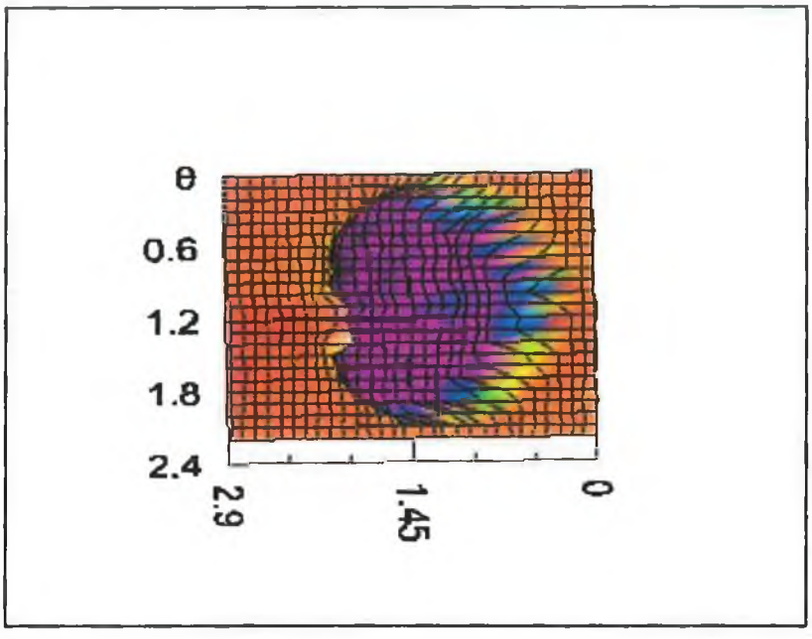

Figure 5.48: 3-D maps of the brass sample surface with the medium size hole. (diameter 2 mm, depth 0.6 mm)

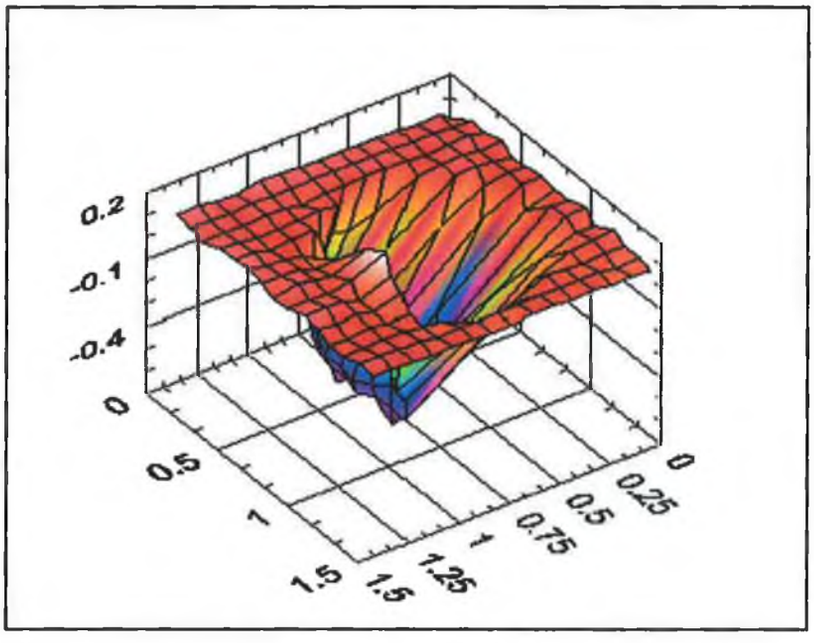

Figure 5.49: 3-D maps of the brass sample surface with the small size hole. (diameter 1 mm, depth 0.6 mm)

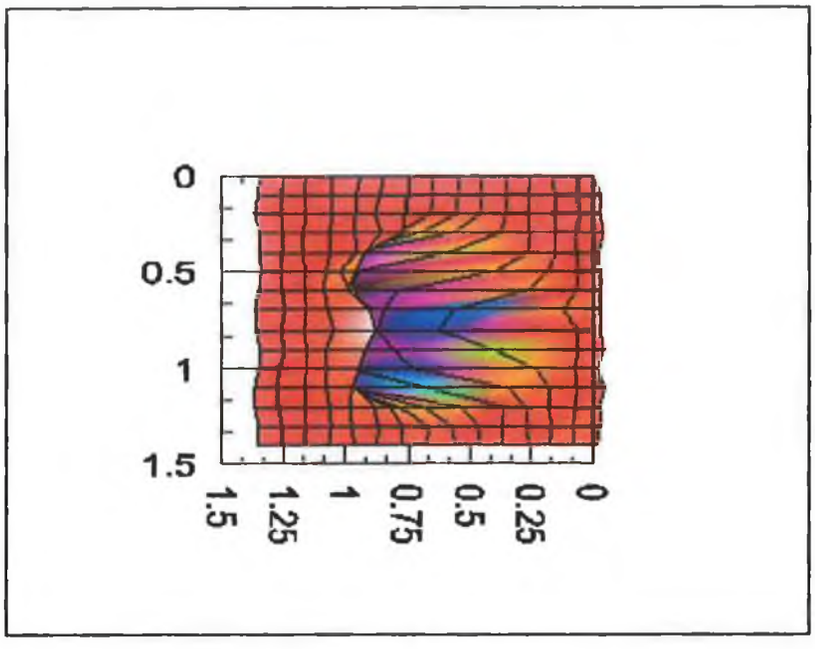

Figure 5.50: 3-D maps of the brass sample surface with the small size hole. (diameter 1 mm, depth 0.6 mm)

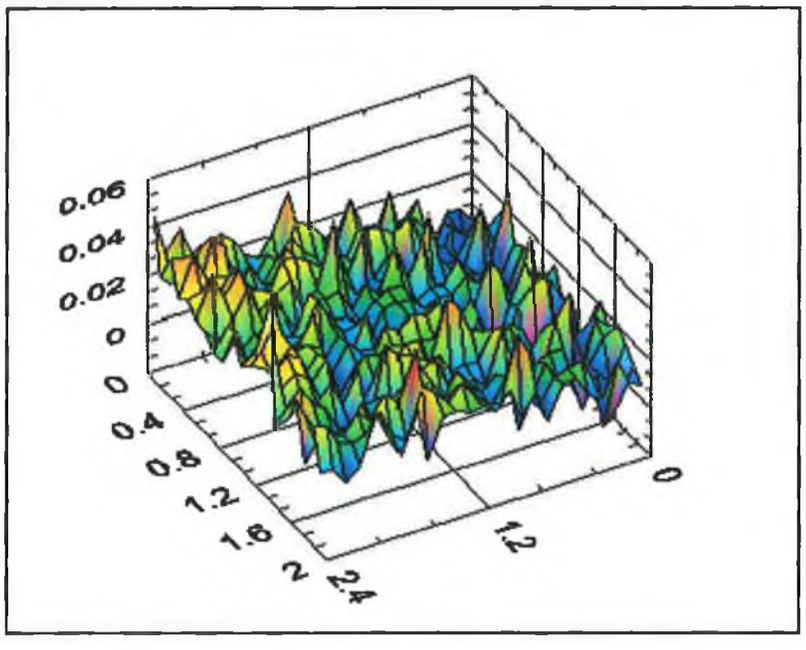

Figure 5.51: 3-D surface map of the plain surface of brass plate.

5.7 Scan Results of Small Unknown Defects

Figures 5.53 to 5.57 show the scan results obtained from the scan performed across the defects on an aluminium surface which produced two-dimensional surface profile. Defects are in the form of crevices of different sizes and depths. These crevices were created by drawing steel scribe across the aluminium surface. Figure 5.52 shows the crevices on the aluminum surface. The six crevices were numbered from one to six from the left side of the figure. The first crevice (number 1) was scribed with the lightest pressure. Increasing pressure was used for creating the crevices 2 through 6.

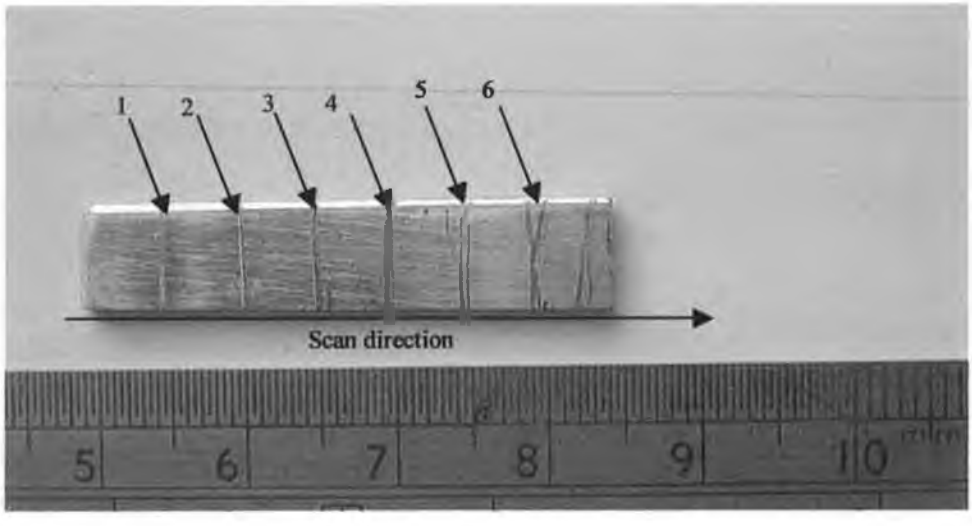

Figure 5.52: Photograph of the aluminium sample with six crevices as defects.

A one-dimensional scan was carried out along the scanning direction as shown in the figure 5.52 and across the each crevice to detect the presence of the crevices on the aluminium surface. The aluminium sample was mounted on the XYZ translation stage and images were captured after every 70 μm step of translation across the crevices. Figures 5.53-5.54, show the scan results that were obtained from scanning across the smallest crevices (crevices 1 and 2 in figure 5.52). The height measurement points vary due to the roughness of the surface, which are almost of the same range of these two crevices. Figures 5.55-5.58 display the graphs that were obtained by scanning across crevices 3 to 6 in figure 5.52. Positions of the crevices and the width of them are shown in the figures by the two vertical lines in each crevice. It can be seen from the figures 5.55-5.58 that the right side of each crevice is higher with respect to the

other side. In figure 5.55 it may be seen that there is a spike (land area) at the middle of the crevice 3.

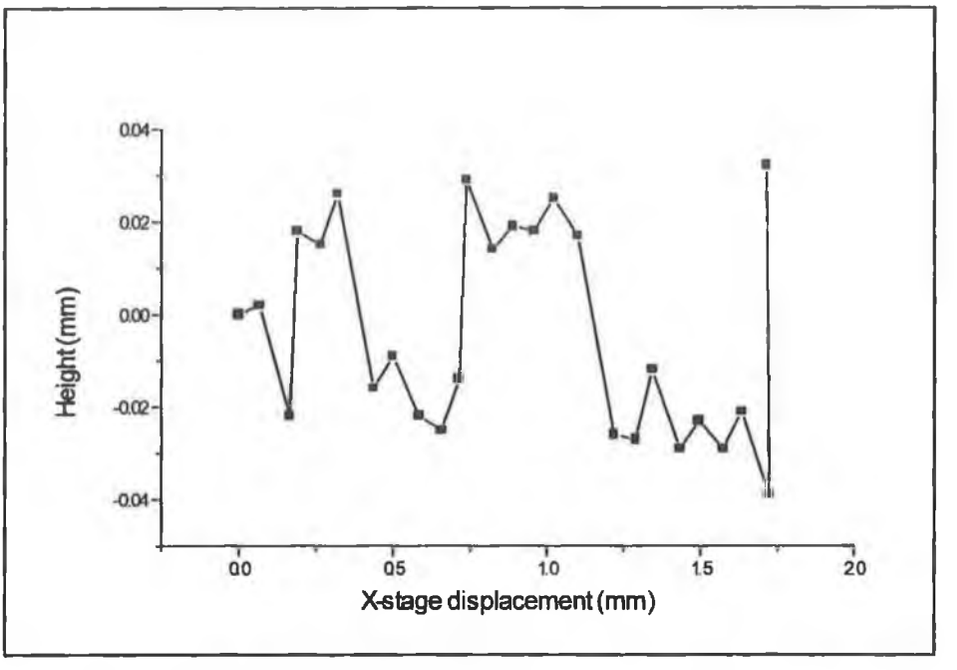

Figure 5.53: Graph of the result for the scanning of crevice 1

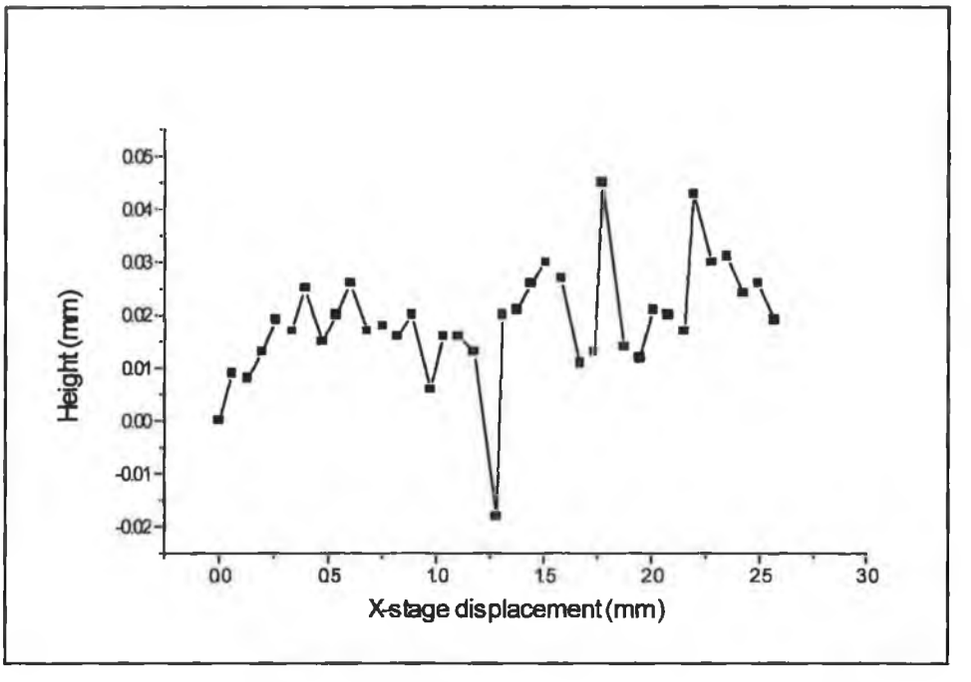

Figure 5.54: Graph of the result for the scanning of aluminum crevice 2.

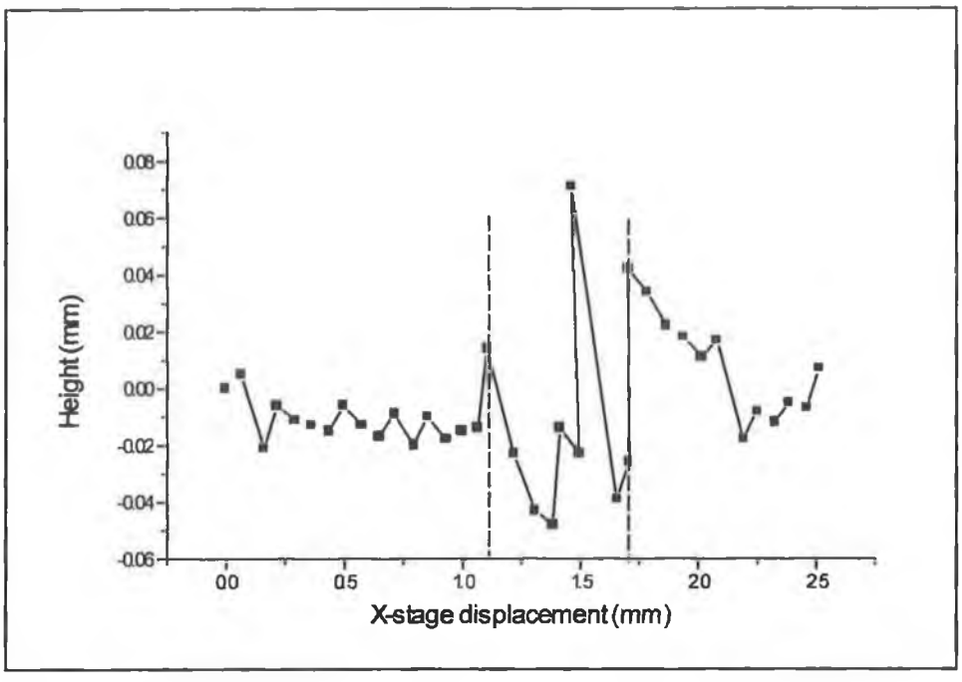

Figure 5.55: Graph of the result for the scanning of aluminum crevice 3.

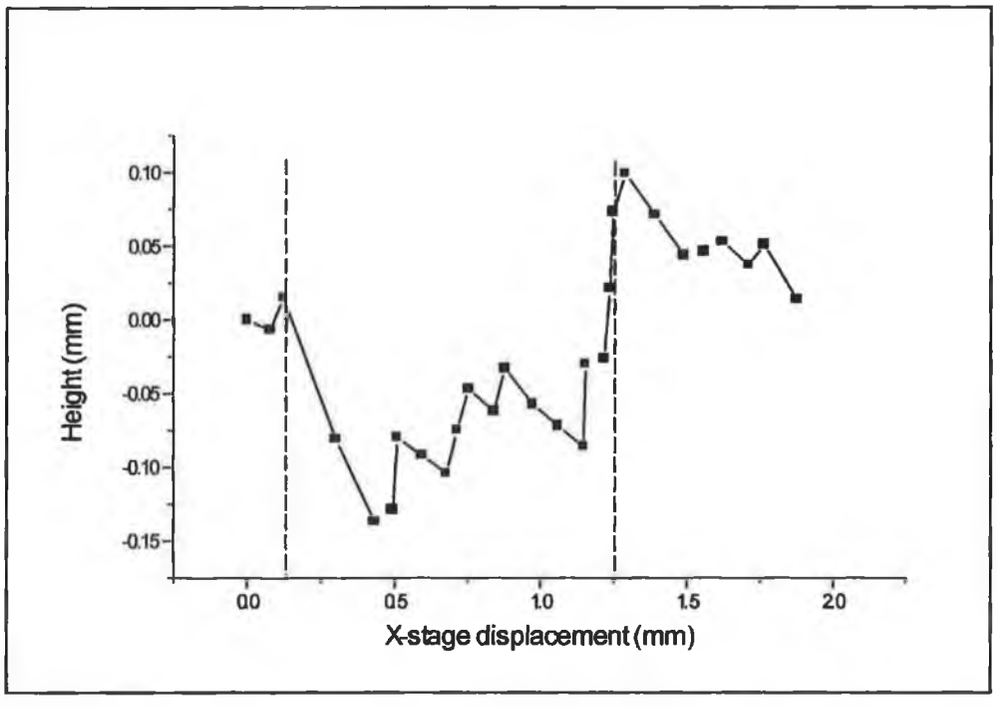

Figure 5.56: Graph of the result for the scanning of aluminum crevice 4.

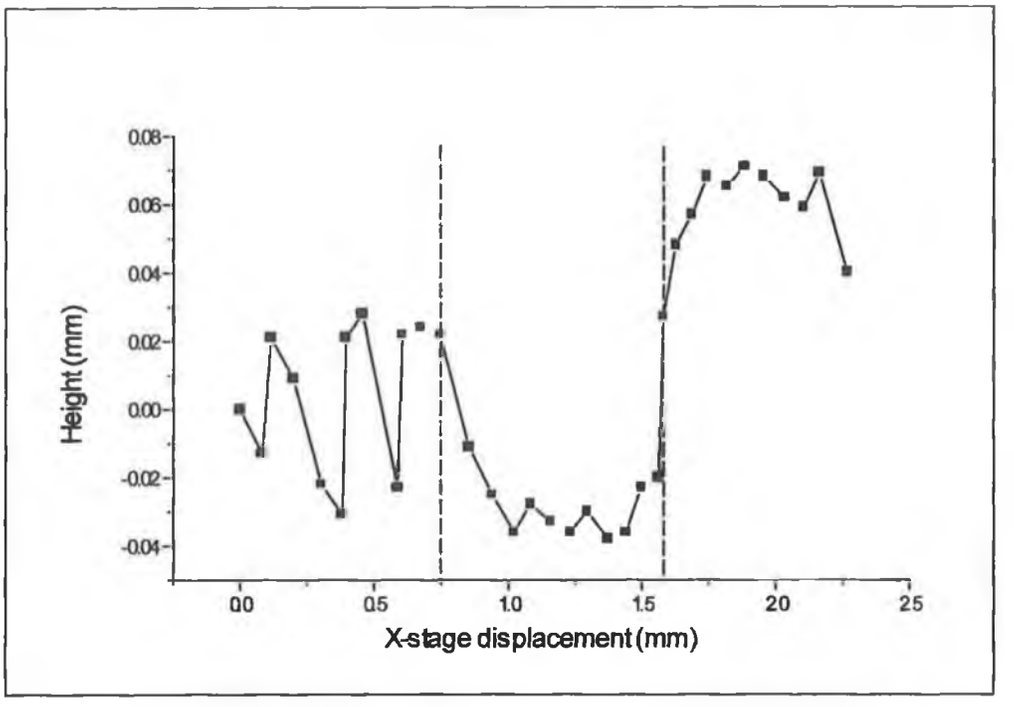

Figure 5.57: Graph of the result for the scanning of aluminum crevice 5.

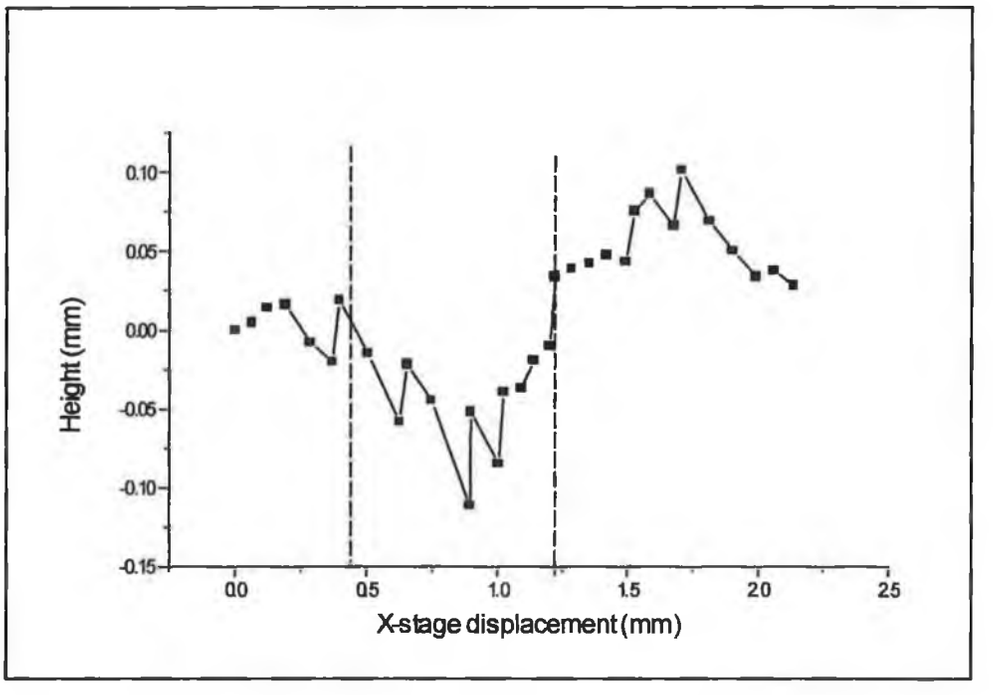

Figure 5.58: Graph of the result for the scanning of aluminum crevice 6.

Chapter Six

6 Discussion of Experimental Results

6.1 Introduction

In this chapter the experimental result presented in the previous chapter are discussed. Initially, the results are analyzed of those experiments required to determine the sensor systems parameter and characteristics. This includes measuring the calibration factor of the system and the lateral resolution of the system. Then, the recorded reflectance of the different sample material surfaces is discussed. Finally, results obtained by scanning different sample surfaces is analyzed.

6.2 System Calibration

For a fixed incident angle of the laser beam and a fixed optical system of the sensor the conversion factor must be fixed. As can be seen from the graphs (figures 5.18-5.27) that the conversion factor calculated varies. This is because of the uncertainty of measurement of the beam centroid location from the image. Different threshold values affect the centroid value measurement. If the threshold value is not large enough to suppress the background noise it would lead to erroneous centroid calculations. It can be observed from table 5.2 that for a fixed Z-step increment value, conversion factor decreases as the threshold value increases. Uncertainty of the centroid location measurement is also noticeable when the Z-stage increment is small. From the graphs it can be seen that for smaller Z-stage increment values and smaller threshold values, the calibration curves are not as smooth. This is because of the speckle effect that occurs due to the roughness of the surface (see equation 3.3).

From table 5.2 it is observed that the experimental value of conversion factor range from 42.47 μm/pixel to 55.29 μm/pixel. In order to be able to find the conversion factor close to the optimum for the present system, different conversion factors were employed on a height measurement scan. The relative percentage errors for different

conversion factors were calculated as shown in the figure 6.1. In the figure 6.1 curve A, curve B and curve C are the three curve points for different conversion factors 44.96 μm/pixel, 42.47 μm/pixel, and 44.7 μm/pixel respectively. These conversion factors were used to determine the vertical displacement and the scanning points were obtained by incrementing the surface along Z-axis direction in steps of 100μm. From the figure 6.1 it is seen that the conversion factor of 42.47 μm/pixel resulted in the largest percentage error in measurement. For the conversion factor 44.7 μm/pixel and 44.96 μm/pixel, percentage error was small. The error is the smallest for 44.96 μm/pixel. So this value was taken as the conversion factor for the system.

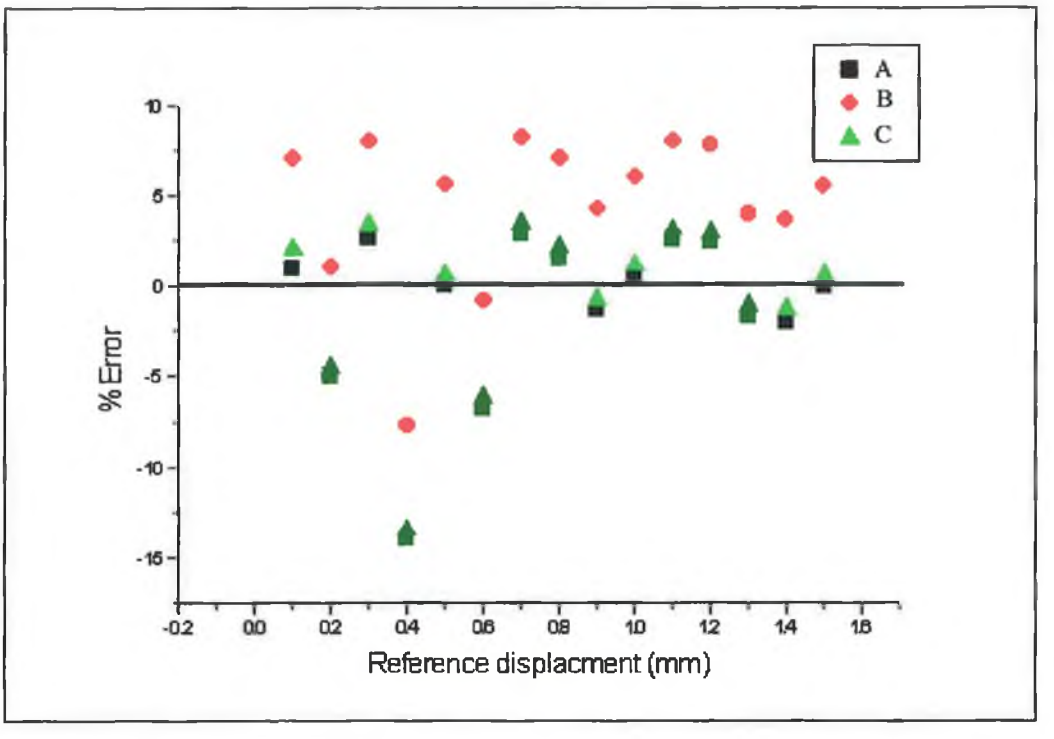

Figure 6.1: Measurement of percentage error when taking vertical measurement with different conversion factors. 100 μm steps were taken in the Z-direction.

6.3 Lateral Resolution of the Inspection System

Lateral resolution of the system is the measure of the laser beam spot width on the surface of the part to be scanned. Figures 5.29-5.31 show the results of laser beam width measurement. These experimental results were following a methodology similar to the knife-edge method. Since intensity distribution of the laser beam

follows a gaussian form, it does not have a sharp boundary. Instead, the beam intensity gradually decreases at farther distances from the beam center. In the experiment, when laser beam spot was made to pass a sharp edge, the intensity of that portion of the laser beam that fell on the other surface level followed the Gaussian distribution as shown in figure 5.28. This gradual split of the laser beam in two surface levels caused the centroid position to shift. It can be seen in the figures 5.29-5.31 that a significant slant is noticeable while the centroid positions change from one level to another level. Slight bends are observed at the beginning of the slant where it just leaves one surface level and at the end where it meets the other surface level. These bends are due to the gradual change in centroid positions that occurred.

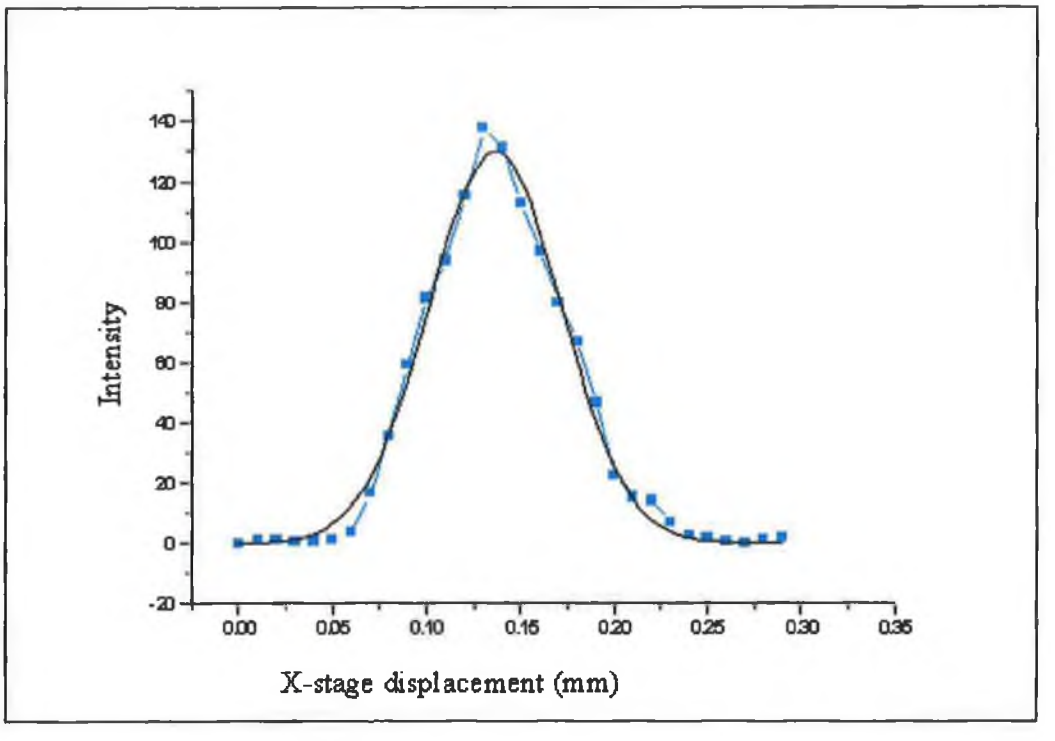

Figure 6.2: Gaussian intensity distribution of the beam spot obtained from figure 5.31.

To obtain a Gaussian distribution profile the smooth curve from figure 5.31 was differentiated. The line with square points indicates the differentiated curve. Y-axis of the curve in figure 6.2 represents the intensity values. An algorithm was applied on this curve in order to obtain the gaussian fitted curve shown in the figure 6.2 with solid black line. The width of this gaussian fit curve is 140μm, which is the width of the laser beam. The lateral resolution of the system is the half of the laser beam width

[68], 70μm. Experimental value of the laser beam width is found to be close to the calculated one that was obtained from the present system. The laser beam spot width was calculated using the equation 2.7. Assuming that the diffraction limited beam spot occurs on the sample surface at an angle of 45°, the theoretical laser beam spot width is approximately 129μm.

6.4 Reflectance Property of the Sample Materials

From table 5.1 it can be seen that surfaces of different sample materials show different average intensity values. The uncoated aluminium surface was found to have the highest reflectivity and stainless steel the lowest. These values are dependent on various parameters such as roughness of the surface, reflectivity, external lighting conditions, and aperture of the camera. As the camera viewed the reflected laser light normally, brightness values obtained were only due to the diffuse reflections and the specular reflection was not counted. Stainless steel surfaces seemed to show lower values of brightness as perhaps greater portions of the reflected beam are due to the specular reflections and only small portions contributed to diffuse reflections. Absorption of light beam was more evident in anodized aluminum compared to the other surfaces. Intensity values increased when the opening of the camera was widened since light passing through the lens was higher.

So, it can be said that the brightness values are one of the fundamental characteristics of a material surface that indicate its reflectivity. Different brightness values for different material surfaces at different aperture openings are used to select threshold values to eliminate background intensity levels while carrying out the calculation of the laser beam centroid position.

6.5 Surface Defect Sensing

In this section experimental results shown in the sections 5.6.1 and 5.6.2 are analyzed and discussed. Analysis of these results is intended to assess the performance of the inspection system in measuring surface defects. Results were obtained for scanning

plane surfaces without any defects and for scanning surfaces with defects of different sizes.

6.5.1 Scanning of Defect Free Surfaces

At first, plane surfaces of different material were scanned. Two-dimensional scan results of the defect free plane surfaces are shown in the graphs 5.33, 5.37, and 5.41 and a three-dimensional mapping of the plane surface is shown in figure 5.51. It can be seen from these graphs that the apparently plain defect free surfaces contain a significant amount roughness. The developed system is able to sense the roughness of the sample surface. However, the random variations of the range data are not the real measure of the roughness. This inspection system was not intended for the measurement of the surface roughness although it could clearly be used as a roughness sensor by employing suitable optical system, which could also enable the system to inspect surface at higher resolution. Variations in height measurement in the plain surfaces occur due to the uncertainty in the measurement of the laser beam centroid positions. Laser beam spot centroid position was affected by the surface roughness which resulted the variations in height measurement. This value was also affected by the selection of the threshold value to suppress the background noise level. For different threshold values different range value would be obtained.

Although it is not possible to measure the surface roughness values from these results, it can be used to classify the roughness for different sample surfaces relative to each other. The stainless steel surfaces were observed to have a higher roughness with compared to the other two sample surfaces. From the figure 5.41 it was seen that brass sample was smoother than the two other sample surfaces. In figure 5.37 the profile curve has spikes at a regular interval. These spikes corresponded to machining marks that could also be seen from examination of the surface without any optical aid.

From these figures it was also seen that height values were higher on the right hand side of the graphs with respect to the left hand side. This was due to the misalignment of the X-Y-Z translation stage that held the samples and as a result one side of the stage appeared to be elevated with respect to the other side. This caused an angle between the virtual reference plane and the stage. The affect of this misalignment is

particularly critical to this inspection system's operation when the measuring range is small and liable to create significant misconception about the height measurements. At the same time this effect suggests the systems ability to sense misalignment.

6.5.2 Scanning of Surfaces with Defects

Blind circular holes were regarded as the known defects. Their size and height were known beforehand. The sizes of the blind holes were of 1 mm, 2 mm and 3 mm diameters. The blind holes were scanned to determine the performance of the inspection system as a surface defect sensor. Results from sections 5.6.1 and 5.6.2 were required to describe the geometry of the holes.

In section 5.6.1, results describe mainly the depth of the holes and also show the affect of the surface properties in height measurement. The machining operation required to produce a blind hole produced a surface at the base of the hole that behaved differently from the surface of the plate. The surface at the base of the blind holes appeared to be polished and shiner than the surface of the plate. The shine of the base of the holes changed the reflectance properties of the sample surface. It was also noticed that for the surface of the base machined blind holes, due to the machining process, there were a number of concentric scratch marks. The laser beam fell on the scratch mark was distorted and therefore, erroneous height measurement resulted. In figures 5.35, 5.42 and 5.43 it can be seen that the surfaces at the base of these holes were not smooth. If the surface of the blind hole was slightly curved this was also sensed by the inspection system, as shown in the figures 5.38 and 5.42.

While scanning across a hole, as long as the laser beam spot fell on the portion of surface that lay before the center of the hole, the reflected laser beam was found to be quite bright. But, as soon as laser beam crossed the center, reflected laser beam intensity became subdued due to the surface profile and sometimes was very difficult to distinguish from the background intensity level.

The depths of the holes shown in the figures of the section 5.6.1 were found to vary for different sample materials. For aluminium, the depth values obtained from the three blind holes were very much close to the actual depths of the holes (measured by

vernier). Depth of the stainless steel big hole (figure 5.38) and medium hole (figure 5.39) were around 0.5 mm and the small hole (figure 5.40) was found to have a depth value of 0.55 mm. The brass sample with the biggest hole had a depth value, as found from the figure 5.42, very close to the actual depth measured by the vernier. For medium size brass hole the depth value found was around 0.45 mm and from the small hole the depth value found was around 0.5 mm. The reason of these variations in the depth values of different samples might be due to the different profiles generated by machining of the base of the holes.

It was seen in all the figures of section 5.6.1 that the left edge of the holes was not steep, instead a significant slope was observed. While switching from one level to the another, there were mostly no measurement points in between. This was due to the shadow effect as described in section 3.2.3. Due to this effect some of the areas in the surface remained unscanned. This thing was very much evident in the figures 5.36, 5.40 and 5.44 where it showed the scan results of the smallest holes (1mm diameter). Most parts of the surface at the base of the small holes remained unscanned.

In figures 5.34, 5.35, and 5.40 it was seen that when switching from one level to another on the left hand side there were no other points in between. That means that the laser beam spot fell sharply from one level to another. But in other figures one or two more points were seen halfway between these two points. This occurred because during scanning, the laser beam spot sometimes split up at the edge. One portion of the spot fell in the surface of the plate and the other portion fell in the base surface of the hole. Thus the measured range data is positioned somewhere between the two surface levels. On the other hand, the right edge of the holes consisted of a number of measurement points.

In section 5.6.2, three-dimensional maps of the scanned surfaces are shown. It was seen that for larger sized hole, the inspection system could reconstruct the holes more accurately. It is clear that the 3-D surface maps presented in section 5.6.2 were able to detect the presence of holes of any size, but the detection of the shape was subject to the size of the holes. In the figures 5.46, and 5.48 it can be seen that the diameter of the open end of the holes are almost exactly equal to the actual diameter of the holes. However, the diameter at the surface of the base of the holes is smaller than the actual

diameter. The reason as explained earlier is also a result of the shadow effect. The sensor is able to sense every point on the edge of the open end of the holes. However, when the laser beam spot was incident at the base surface of the hole, some of the area remained out of sight of the laser beam and hence the diameter detected was smaller than the actual diameter. In the figure 5.50 shape of the small hole (1mm diameter) was clearly not well defined. Due to this effect the open end of the hole was not found to be circular, instead the shape was distorted at one side. The side walls of the smallest holes were also seen to be narrowed from actuality at the bottom of the hole.

The above discussion of the observed three-dimensional maps described a fundamental limitation of the optical triangulation based inspection system. If the hole is deep enough it might be possible, depending upon the width of the hole, that the laser beam never reaches the bas surface but instead hits the sidewalls. Although the system could be able to sense the position of the hole as a defect, in this case it would not be able measure the exact shape of the hole. This limitation was especially noticeable when the diameter of the hole was quite small. There must be a relationship between the width and the height of holes that can be scanned. This is depicted in the figure 6.3 where the incident angle of the laser beam is 45°. In order to detect the base surface of the blind holes the width and height of the hole must satisfy the following relationship:

$$\frac{w}{h} \geq 1 \qquad 7.1$$

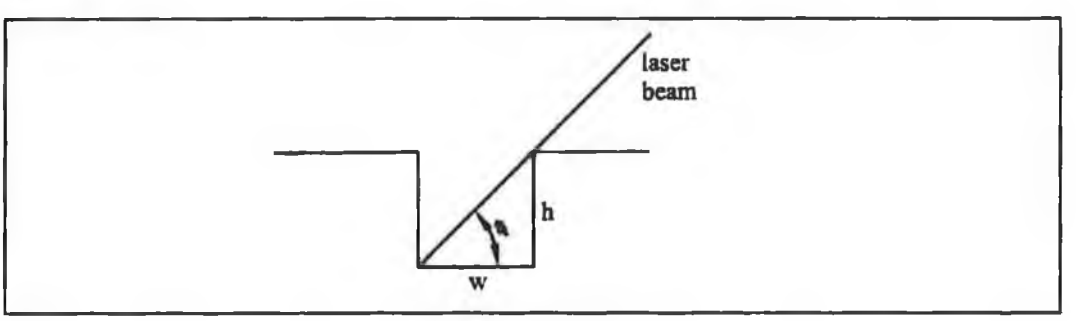

Figure 6.3: Relationship between the width and height of a hole.

The figures in the section 5.7 show the results obtained from the scanning of the six crevices on the aluminum samples. The crevices were regarded as the unknown

defects. In figures 5.53 and 5.54, it was seen that for scanning the crevices number 1 & 2, the inspection system was unable to sense them. These figures only show the height measurement data points due to the surface roughness only and the presence of the crevices were completely unnoticed by the inspection system. This suggests that the crevices 1 & 2 were of smaller in size with respect to the lateral resolution of the system and also the depth of the crevices were also insignificant for the system to measure. In the figures 5.55 to 5.58, it was seen that the system is able to sense the presence of the crevices. Crevices 3 to 6 can be seen in the figure 5.52 to be much deeper and wider in size and that was reflected in the scan results, figure 5.55 to 5.58. In figure 5.55, it was seen that there was a spike in the graph in the middle of the crevice position. This crevice (number 3) has another small scratch as a branch of it, which is positioned just parallel to it leaving some material not removed between the two crevices. The crevices in figure 5.56 and 5.57 were found to be much wider than the other crevices. From figures 5.55 to 5.57, it can be seen that the one side of the crevices represented had one side higher with respect to the other. This can be explained as a result of the materials that accumulated on that side when the crevices were created.

6.6 Source of Error in Depth Measurement

There are a number of conditions under which the optical triangulation based system suffers from reduced accuracy or even fails completely. Since the developed system was to detect the surface defects and not intended to be used for extremely accurate surface reconstruction, errors in the range measurement do not receive much importance. Yet, these errors may sometimes indicate defects which do not exist. Most of the errors affect the height measurement by causing beam centroid positions on the sensor to be shifted from the positions where it is supposed to be. Shift of the beam centroid positions occur as the center of the laser beam spot image gets distorted on the sensor due to range or intensity discontinuity. The sources of errors are explained and their effects on the height measurement are mentioned below.

Adverse illumination is one of the sources of errors that affect the height measurement of the inspection system. When the surface is illuminated strongly due to the external lighting, the contrast of the image is greatly reduced. This results in a bad separation

between the laser beam spot and the background color of the surface, hence making detection difficult. This problem can be alleviated by controlling the amount of light falling on to the sensor. Amount of light passing through the lens is controlled by narrowing the aperture of the lens, which acts as natural filter to reduce the scatter. Even with the narrowed aperture, variation in ambient lighting can affect the laser beam centroid position measurement. As the different ambient lighting renders different values of background intensity levels, the threshold value to eliminate the background intensity level varies.

When the laser beam strikes at the corner of an object, it is often the case that only a part of the laser strikes the surface and not the whole laser as shown in the figure 6.4. The centroid position of the partially reflected laser beam on the sensor is shifted and this results in the corner of the object being lifted away from its real position, by a distance proportional to the with of the beam.

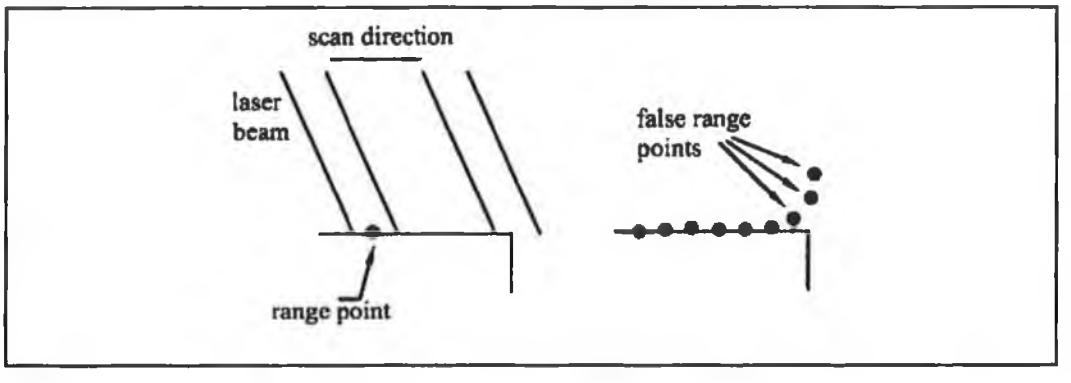

Figure 6.4: Depth measurement error due to vertical edge.

The same affect can occur if there is sharply contrasting texture on the surface. When laser beam falls on the surface with contrasting texture, laser beam is reflected at different intensities. Image spot on the sensor comprises of different intensities of light and the Gaussian intensity distribution is distorted which results in the shift of the beam centroid position. Hence, false range measurement point is obtained.

Height measurement error can take place due to unwanted reflection of the laser beam. When the laser beam is incident on a surface, the specular portion of the reflected beam may illuminate another object on its way. The sensor may then see two beam spots instead of the real beam spot causing the beam centroid position to be

shifted representing false height data. In this inspection system, this effect was avoided by carefully selecting the image window of interest (WOI) size so that extra reflections did not appear in the image. False measurement points can also be created when the laser strikes two surfaces at different angles causing the reflection from one surface to be ignored because it is too dim. This effect can be seen in the figures in section 6.6.1, as some spurious height points were noticeable where the vertical edge of the right hand side adjoined the surface of the plate at different angles. This error indicated that the surface was protruding upward.

Chapter Seven

7 Conclusions and Recommendations for Further Work

7.1 Introduction

This chapter draws conclusion of the developed surface defect inspection system regarding its intended objectives, design, development and the results achieved by the system. Also, recommendations for further work are outlined in order to improve the system.

7.2 Conclusions

The objective of this project was the development of laser inspection system to detect surface defects. The developed system is the prelude to a comprehensive inspection system that will perform high-speed online laser scanning for surface inspection. As the part of a broader inspection system, the present system was successfully developed to assess the data processing ability in constructing three-dimensional maps of surfaces and hence to detect different types of defects on the surface.

7.2.1 Laser Inspection System Development

- The developed laser based inspection system is a simple system which consists of a laser diode module, a random addressable CMOS camera and an optical system as the main components of the system. The laser diode module is able to produce a small beam spot using proper optics compatible to the defect sizes. It was seen in designing the system that the optical systems determine the different parameters of the inspection system such as resolution, accuracy. The plano-convex lens was used to focus the laser beam spot on to the sample surface and had a focal length of 150 mm. It was calculated theoretically and substantiated experimentally that laser beam spot size onto the sample surface is approximately 140 μm, which rendered the spatial resolution of the system to be 70 μm. Depth of field of the laser beam focusing system is 6 mm. Camera resolution is determined by the

objective lens and the plano-convex lens of 100 mm focal length and was found to be 50 μm/pixel. Depth resolution of the system is around 60 μm.

- Calibration of the laser inspection is easy although there are some uncertainties involved due to the surface roughness while calibrating the system. Calibration of the system resulted a conversion factor between the measured spot's shift and the corresponding surface's vertical displacement. In this system the conversion factor was 45 μm/pixel.

- The pixels in the Fuga 15 sensor can be accessed randomly, which enables a window of interest of variable size. If the window of interest is small, it is possible to achieve very high frame rates, which indicates that the developed inspection system has the potential for high-speed operation. Although manual capture of the images was used, high speed operation was observed due to the small window size while processing the series of captured images with the developed software.

- A number of programs were written to carry out different tasks regarding the inspection system. An algorithm was developed to measure the laser beam spot centroid location. The function of the "CALIBRATION".vi was to calibrate the system. The data processing task was carried out by the "3D SURFACE MAPPING".vi, which generated the three-dimensional topographic maps of the surface. This software was able to produce the reconstruction of the scanned surface. "SURFACE MAPPING".vi was used to generated two-dimensional profile of the scanned surface.

- Since, the depth and lateral resolution depends upon the system configuration, incidence optics and observation optics, this laser inspection system is able to inspect a large variety of surfaces with resolutions, down to the submicron level.

7.2.2 Conclusions from the Experimental Results

- Reflectivity of the surface materials was measured in terms of the intensity values of the surfaces. Reflectivity values were found to be dependent upon the external

lighting and aperture stop of the objective lens. It was seen that different reflective properties of the different material used did not affect the system in measuring.

- In the preliminary experiments laser scanning was performed on the surface of plates of the following materials: brass, stainless steel and aluminum. Blind holes of 3 mm, 2 mm, and 1 mm diameter on the surface plates were regarded as known defects and were scanned by the inspection system in order to detect the presence of holes and to generate three dimensional surface map. Scanning was also carried out on the plane surfaces without any defects.

- Three-dimensional maps of the plane surfaces without defects were found not to be smooth. Small height variations were observed due to the surface roughness. As it was discussed in the previous chapter, although these variations were due to the surface roughness, it was not the measure of the actual roughness value rather it was indicative to the relative surface roughness.

- The developed inspection system is able to sense the presence of 3 mm, 2 mm and 1 mm diameter of blind holes of the surfaces of different materials. But there is a limitation in the adequate representation of the diameter, shape and positions of holes of any sizes. It was seen that the diameter, shape and position of the holes of 3 mm and 2 mm diameter and around 0.6 mm depth can be represented by the inspection system quite well. However, 1 mm diameter holes could not be represented properly. It was explained in the previous chapter that this limitation was due to the shadow effect that excludes some region being completely scanned.

- There are few limitations present in the height measurement. The system can not sense any through holes as the developed inspection system utilized the triangulation method for measuring height points. The depth of the holes that the inspection system can measure is limited by the width (diameter) of the holes and in order to be able to measure the depth of the holes, the ratio of the width and the height of the holes must be greater than one. Limitations in height measurements may result from the errors in the measurement beam centroid location, which, as

explained in the previous chapter, are due to the unwanted double reflections, edge curl, texture variations and adverse illumination.

- Results obtained from scanning the crevices on the aluminum surface showed that the system could detect small defects comparable to spatial resolution of the system.

- The inspection system was able to sense the misalignment of the XYZ stage. As a result the sample plates were slightly tilted horizontally. This misalignment may incur false height points.

- A reasonable degree of accuracy was obtained in the height measurement by the developed laser inspection system. The percentage uncertainty in height measurement by the inspection system was found to be large at a range close to the depth resolution. The system was found to be highly repeatable in the range measurement.

7.3 Recommendations for Further Work

In this project the development of the laser inspection system was found to conform with the intended goal of surface defect detection by generating three-dimensional surface maps. Yet there is a huge scope in the improvement of the system that would enhance the systems applicability. A number of recommendations for further works are proposed in this section in order to turn the system into a highly novel system. The possibilities of wider application are also explored.

7.3.1 High-Speed Defect Detection System.

Further work is recommended mainly to develop an inspection system that would enable high-speed online inspection of the surfaces with higher accuracy and resolution. In the present inspection system, speed consideration was overlooked. Scanning was performed by manual operation of the translation stage rendering the system very slow. Taking a full set of readings consisted of choosing a suitable

window of interest in the camera sensor, manually incrementing the translation stage at certain steps followed by capturing the image at every steps. Once the scanning of the surface was finished and the images were stored in the specific directory, the analysis software was run to process the images to generated three-dimensional mappings of the surface. So the whole process of surface inspection involved two different steps, scanning the surface and processing the images. In the real time online inspection, it is imperative that the two steps are being carried out simultaneously.

Automation of the scanning can be achieved either by motorized translation stages or by using high-speed laser beam deflector. Motorized translation would improve the system but the inertia of the system might limit the high-speed performance. Online operation of the inspection system could only be achieved by employing high-speed electro-optic laser beam deflector.

The main idea of a future inspection system could be to generate a topographic map, scanned from a defect free part and. This map would then be used by a software application for comparing it with that received from the laser inspection system. The online inspection system consists of various functional blocks, laser scanning unit, camera, and data processing unit. Each functional block consumes time, which represents its working bandwidth. Real time online inspection requires that the global system scans the surface and then decides about the inspected piece in a very short amount of time. This time is split up for the operation of various functional blocks. Time is required for reading the pixels of the array sensor and then to process the images. Between two successive image acquisitions, the data processing takes place for the latest scan. Therefore, the scanning speed is determined by the combined times of the image acquisition and the data processing.

The random access property of the camera allows the sensor to form a small window of interest, which enable high frame speed as shown in the figure 4.7. The Smaller the window of interest is, the less data that needs to be processed. But if the window of interest is small, then the frame speed is higher and might be much faster than the scanning speed, unless a high-speed laser beam deflector is used. The number of image frames required to inspect a particular surface area is equal to the total number of scan points required for scanning that surface. If the scanning speed is much slower

than the image frame speed between two consecutive scan steps a number of superfluous image frames are generated. It is necessary to dispense with those redundant image frames and only capture those frames that synchronize with the scan steps. A scan controller could control the scan speed with knowledge of the step size of the laser scan and the time to travel that step. Synchronization of the scan steps and the image frame acquisition can be performed by the controller by triggering signals simultaneously to the scanner and to the camera software. The software with the CCf15 camera allows for such automation. The time delay between the two consecutive steps can be utilized for processing the data obtained from the images. Data processing tasks involve converting of the image BMP file to text files, locating the beam spot centroid position in the image, and carrying out the mathematical calculation to generate height points. For the high speed, system might require a special DSP unit to perform these tasks.

In the present system, the algorithm used to detect the laser beam centroid position onto the image was simple. A much faster algorithm could also be employed to reduce the processing time.

In the present system, angle between the direction of laser beam illumination and the direction of observation was set to be at 45° angle. But it was not possible to measure the angle accurately. Accurate knowledge of this angle could help determine the conversion factor precisely. An optical encoder could be employed to determine the angle.

7.3.2 Further Application

The ability of the developed inspection system to generate three-dimensional topographic maps suggests that could be used in the three-dimensional reconstruction of objects. Three-dimensional reconstruction of objects is an important task in almost every stage of industrial product or tool life cycle. Optical measurement of surfaces is much faster than mechanical measurement. Three-dimensional reconstruction of objects can be employed in reverse engineering and quality control processes [95]. Three-dimensional reconstruction of the free-form surfaces can be used to generate

CAD models. To be used in those applications, the inspection system also requires improvements. In 3-D reconstruction, emphasis must be given to the accurate height measurements. All the source of errors discussed in the section 7.6 must be dealt in order to dispense with them. Stereo vision could remove the problem of the shadow effect and the associated errors in height measurement points could be avoided by developing suitable algorithms. Instead of a laser spot, a laser line could be used to perform the scanning. By projecting a laser beam line on a surface, scanning speed could be increased since it would save the system from generating raster-scanning pattern.

References

[1] Uiga, E, 1995, Optoelectronics, Prentice Hall, Inc., New Jersey.

[2] Chaimowicz, J. C. A., 1989, Optoelectronics-An Introduction, Butterworth Heinemann Ltd., Oxford.

[3] Iga, K, 1994, Fundamentals of Laser Optics, Plenum Press, New York.

[4] Young, M, 1993, Optics and Laser- Including Fibers and Optical Waveguides, Springer-Verlag, Berlin Heidelberg New York.

[5] Wilson, J., Hawkes, J. F. B., 1987, Lasers Principles and Applications, Prentice Hall International (UK) Ltd.

[6] Luxon, J. T., Parker, D. E., 1985, Industrial Lasers and their Applications, Prentice Hall, Inc., New Jersey.

[7] Clarke, T. A., Katesimbris, A., 1994, The Use of Diode Laser Collimators for Targetting 3-D Objects, International Archives of Photogrammetry and Remote Sensing, XXX(5), pp. 47-54.

[8] Kogelnik, H., Li, T., 1966, Laser Beams and Resonators, Applied Optics, 5, 10, pp. 1550-1567.

[9] http://nctt1.stcc.mass.edu/photonic_web/code/laserapps.htm

[10] Fein, H., 1997, Holographic interferometry: Non Destructive Tool, The Industrial Physicist, 3 (3), pp. 37-38.

[11] Beiser, L., 1995, Fundamental Architecture of Optical Scanning Systems, Applied Optics, 34, 31, pp7307-7317.

[12] Beiser, L., 1974, Laser Scanning Systems, Laser Applications, Academic Press, New York, 2, pp. 53-169.

[13] Cahill, B., 1998, Laser-Based Fibre-Optic Sensor for Measurement of Surface Properties, M.Eng. Thesis, Dublin City University, Ireland.

[14] Marshall, G. F., 1980, Scanning Devices and Systems, Applied Optics And Optical Engineering, Academic Press, 6, Inc, New York.

[15] Rowe, D.M., 1997, Developments in holographic-based scanner designs, Proc. SPIE, 3131, pp 52-58.

[16] Aronson, H. J., 1976, Acousto-optic Scanning, Laser Focus, 12, 12, pp. 36-39.

[17] Huang, Z., Munro, N., Huhmer, A. F., Landers, J. P., 1999, Acousto-optical deflection-based laser beam scanning for fluorescence detection on multichannel electrophoretic microchips, Analytic Chemistry, 71, pp. 5309-14.

[18] Jennewein, H., Ganz, T., High-precision optical profile measurements by simultaneously material characterization, IAP/LTO-Annual report 1998/1999, pp. 37-40.

[19] Fujita, H., 1990,Two Dimensional Micropattern Measurement Using Precision Laser Beam Scanning, Proc. SPIE, 1332, pp 456-467.

[20] Maak, P., Jakab, L., Richter, P. I., Brignon, A., Huignard, J. P., 2000, Combination of A 2-D Acousto-Optic Deflector With Laser Amplifier For Efficient Scanning of A Q- Switched ND:YAG Laser, Optics Communications, 176, pp 163-169.

[21] Hinkov, I., Hinkov, V., Wagner, E., 1995, Digital Electro-Optical Laser Beam Deflector With Domain-Inverted Prism-Array, Laser'95, Optical Components and Systems, pp19-23.

[22] Ninomia, Y., 1974, High S/N-ratio electrooptic prism-array light deflectors", QE-10 pp. 358-362.

[23] Elliot, R. A., Shaw, J. B., 1979, Electro-Optic Streak Camera, Applied Optics, 18, 7, pp 1025-1033.

[24] Gottlieb, M., Ireland, C. L. M., Ley, J. M., 1983, Electro-Optic And Acousto-Optic Scanning And Deflection, Mercel Dekker, Inc. New York.

[25] Gahagan, K. T., Gopalan, V., Robinson, J. M., Jia, Q. X., Mitchell, T. E, Kawas, M. J., Schlesinger, T. E., Stancil, D. D., 1999, Integrated Electro-Optic Lens/ Scanner In a $LiTaO_3$ Single Crystal, Applied Optics, 38, 7, pp- 1186-1190.

[26] Chen, Q., Chiu, Y., Lambeth, D. N., M. C., Schlesinger, T.E., Stancil, D. D., 1994, Guide-Wave Electro-Optic Beam Deflector Using Domain Reversal in $LiTaO_3$, Journal of Lightwave Technology, 12, 8, pp-1401-1404.

[27] Nimomiya, Y., 1973, sUltrahigh Resolving Electro-Optic Prism Array Light Deflectors, IEEE Journal Of Quantum Electronics, QE-9, 8, pp- 791-795.

[28] Nelson, T. J., 1964, Digital light Deflection, Bell System Technology Journal, 33, 3, pp 821-845.

[29] Lotspeich, J. F., 1968, Electrooptic Light-Beam Deflection, IEEE Spectrum, 5, pp 45-52.

[30] Lee, T. C., Zook, J. D., Light Beam Deflection With Electrooptic Prisms, IEEE Journal of Quantum Electronics, QE-4, pp 442-454.

[31] Khayim, T., Shibuya, K., Kobayashi, T., 2000, A New Type of Electrooptic Deflector Using Lens Effect for Ultrafast Light Control, IEICE Trans. Electron., 83, 6, pp 993-996.

[32] Friel, G. J., Conroy, R. S., Kemp, A. J., Sinclair, B. D., 1998, Q-Switching of a Diode-Pumped Nd:YVO_4 Laser Using a Quadrupole Electro-Optic Deflector, Applied Physics B, 67, pp 267-270.

[33] Thomas, J. A., Fainman, Y., 1998, Optimal Cascade Operation of Optical Phased-Array Beam Deflectors, Applied Optics, 37, 26, pp 6196-6212.

[34] Titus, C. M., Bos, P. J., Lavrentovich, O. D., 1999, Efficient, Accurate Liquid Crystal Digital Light Deflector, Proc. SPIE, 3633, pp 244-253.

[35] Klaus, W., Ide, M., Morokawa, S., Tsuchiya, M., Kamiya, T., 1997, Angle-Independent Beam Steering Using a Liquied Crystal Grating with Multi-Resistive Electrodes, Optics Communications, 138, pp 151-157.

[36] Roberts, D. A., Syms, R. R. A., 2000, 1D and 2D Laser Line Scan Generation Using a Fibre Optic Resonant Scanner, Proc. SPIE, 4075, pp 62-73.

[37] Curles, B. L., 1997, New Methods for Surface Reconstruction from Range Images, PhD Thesis, Stanford University, USA.

[38] Schwarte, R., Heinol, H., Buxbuam, B., Ringbeck, T., Xu, Z., Hartmann, K., 1999, Principles of Three-Dimensional Imaging Techniques, Handbooks of Computer Vision and Applications, 1, Academic Press, San Diego.

[39] Howland, R. S., Wells, K. B., Trafas, B. M., 1995, High-Speed Detection of Pattern Defects Using Laser Scattering, Solid State Technology, November, pp. 123-126.

[40] Miller, M., Lakes, R. S., Conner, S., 1996, Optical Testing of Hard Disks, Optics & Laser Technology, 28, 3, 151-156.

[41] Dixon, G. J., 1998, Laser Radars Produce Three-Dimensional Pictures, Laser Focus World, 34, pp. 137

[42] Chen, Y. D., Ni, J., 1993, Dynamic Calibration and Compensation of a 3-D Laser Radar Scanning System, IEEE Transactions on Robotics and Automation, 9, 3, pp. 318-323.

[43] Tsai, M. J., Zahid, M., Smith, J. S., Lucas, J., 1997, A Two-Dimensional Vision System with Optical Ranging Capability, Optics & Laser Technology, 29, 5, pp. 239-247.

[44] Nitzan, D., 1988, Three-Dimensional Vision Structure for Robot Applications, IEEE Transactions on Pattern Analysis and Machine Intelligence, 10, 3, pp. 291-309.

[45] McNeil, M. D., Williams, L., Chu, H., 1999, Design of a Time-of-Flight Range-Finder, Proc. 29th ASEE/IEEE Frontiers in Education Conference, pp. 13d6-17-22.

[46] Beraldin, J. A., Blais, F., Cournoyer, L., Godin, G., Rioux, M., 2000, Active 3D Sensing, Modelli E Metodi per lo studio e la conservazione dell'architettura storica, University: Scola Normale Superiore, Pisa, 10, pp. 22-46.

[47] Subbarao, M., Wei, T.C., 1992, Depth from Defocus and Rapid Autofocusing: A Practical Approach, In Proceedings of CVPR, pp. 773-776.

[48] Hasegawa, J. K., Tozzi, C. L., 1996, Shape from Shading with Perspective Projection and Camera Calibration, Computing & Graphics, 20, 3.

[49] Tsai, R. Y., 1387, A Versatile Camera Calibration Technique for High-Accuracy 3D Machine Vision Metrology Using Off-the-Shelf TV Cameras and Lenses, IEEE Journal of Robotics and Automation RA-3, 4, pp. 323-344.

[50] Beraldin, J. A., Blais, F., Cournoyer, M., Laurin, D., MacLean, S. G., 2000, Eye-Safe Digital 3-D Sensing for Space Applications, Optical Engineering, 39, 1, pp. 196-211.

[51] Clarke, T. A., Gratten, K. T. V., Lindsey, N. E., 1990, Laser-Based Triangulation Techniques in Optical Inspection of Industrial Structures, Proc. SPIE, 1332, pp. 474-486.

[52] Costa, M. F. M., Almeida, J. B., 1993, System of Optical Noncontact Microtopography, Applied Optics, 32, 25, pp. 4860-4863.

[53] Costa, M. F. M., 1996, Surface Inspection by an Optical Triangulation Method, Optical Engineering, 35, 9, pp. 2743-2747.

[54] Ji, Z., Leu, M. C., 1989, Design of Optical Triangulation Devices, Optics & Laser Technology, 21, 5, pp. 335-338.

[55] Rioux, M., 1984, Laser Range Finder Based on Synchronized Scanners, Applied Optics, 23, 21, pp. 3837-3844.

[56] Livingstone, F. R., Rioux, M., 1986, Development of a Large Field of View 3-D Vision System, Proc. SPIE, 665, pp. 188-194.

[57] Levi, P., Vajta, L., 1989, Combined 2-D and 3-D Robot Vision System, Sensor Devices and Systems for Robotics, NATO ASI Series, F52, Springer-Verlag Berlin Heidelberg, pp. 187-194.

[58] Clark, J., Wallace, A. M., Pronzato, G. L., 1998, Measuring Range Using a Triangulation Sensor with Variable Geometry, IEEE Transactions on Robotics and Automation, 14, 1, pp. 60-67.

[59] http://www.canadianmetalworking.com/Content/2001/04-01/cmm040106.htm.

[60] Dremel, W., Hausler, G., Maul, M., 1986, Triangulation with Large Dynamical Range, Proc. SPIE, 665, pp. 182-187.

[61] Wang, H., 1995, Long-Range Optical Triangulation Utilizing Collimated Probe Beam, Optics and Lasers in Engineering, 23, pp. 41-52.

[62] Xinming, Z., Yongxin, S., Jiandong, Y., 1998, Nonlinearity of Optical Triangulation, Proc. SPIE, 3558, pp. 262-265.

[63] Dorsch, R. G., Hausler, G., Herrmann, J. M., 1994, Laser Triangulation: Fundamental Uncertainty in Distance Measurement, Applied Optics, 33, 7, pp. 1306-1314.

[64] Bradshaw, G., 1999, Non-Contact Surface Geometry Measurement Techniques, Technical Report TCD-CS-1999-46.

[65] http://qualitymag.com/articles/1998/sep98/0998f2.htm.

[66] Zeng, L., Matsumoto, H., Kawachi, K., 1997, Two-Dimensional Scanning Method for Reducing the Shadow Effects in Laser Triangulation, Measurement Science Technology, 8, pp. 262-266.

[67] http://www.sensorsmag.com/articles/0598/tri0598/index.htm

[68] Hausler, G., Heckel, W., 1988, Light Sectioning with Large Depth and High Resolution, Applied Optics, 27, 24, pp. 5156-5169.

[69] Baribeau, R., Rioux, M., 1991, Influence of Speckle on Laser Range Finders, Applied Optics, 30, 20, pp. 2873-2878.

[70] Yue, L., Xianohong, L., Dahai, R., Shenghua, Y., 1998, Computer Vision Application for Weld Defect Detection and Evaluation, Proc. SPIE, 3558, pp. 354-357.

[71] Becker, M., 1995, Signal Processing for Reduction of Speckle-Noise in Light-Stripe-Systems, Proc. SPIE, 2598, pp.191-199.

[72] West, G. A. W., Clarke, T. A., 1990, A Survey and Examination of Subpixel Measurement Techniques, Proc. SPIE, 1395, pp. 456-463.

[73] Clarke, T. A., Cooper, M. A. R., Fryer, J. G., 1993, An Estimator for the Random Error in Subpixel Target Location and its Use in the Bundle Adjustment, Optical 3-D Measurements Techniques II, Pub. Wichmann, Karlsruhe, pp. 161-168.

[74] Trucco, E., 1998, Calibration, Data Consistency and Model Acquisition with a 3-D Laser Striper, International Journal of Computer Integrated Manufacturing, 11, 4, pp. 293-310.

[75] Blais, F., Rioux, M., 1986, Real-Time Numerical Peak Detector, Signal Processing, 11, pp. 145-155.

[76] Blais, F., Lecavalier, M., Bisson, J., 1996, Real-Time Processing and Validation of Optical Ranging in a Cluttered Environment, International Conference Signal Processing Applications & Technology, Boston, MA, 2, pp. 1066-1070.

[77] Carlson, B., 1999, An Investigation of CCD Cameras and Image Processing Techniques for the Large Adaptive Reflector CCD Based Surface Measurement System, National Research Council of Canada

[78] Shortis, M. R., Clarke, T. A., Short, T., 1994, A Comparison of Some Techniques for the Subpixel Location of Discrete Target Images, Proc. SPIE, 2350, pp. 239-250.

[79] Wong, K. W., Wei-Hsin, H., 1986, Close Range Mapping with a Solid State Camera, Photogrammetric Engineering and Remote Sensing, 52, 1, pp. 67-74.

[80] Theuwissen, A., Solid-State Imaging with Charge-Coupled Devices, Kluwer Academic Publishers, Eindhoven, 1995.

[81] Meynants, G., Dierickx, B., Scheffer, D., 1998, CMOS Active Pixel Image Sensor with CCD Performance, Proc. SPIE, 3410, pp. 68-76.

[82] http://www.on-trak.com/appnote2.htm.

[83] Fossum, E., 1997, CMOS Image Sensors: Electronic Camera-On-A-Chip, IEEE Transactions on Electron Devices, 44, 10, pp. 1689-1699.

[84] Fossum, E., Wong, I., 1994, Future Prospects for CMOS Active Pixel Sensors, IEEE Workshop on CCDs and Advanced Image Sensors, Dana Point, CA, April 20-22.

[85] http://archives.e-insite.net/archives/ednmag/reg/1997/100997/21df_02.htm

[86] Meynants, G., Dierickx, B., Scheffer, D., and Vlummens, J., 1998, A wide dynamic range CMOS stereo camera, Proceedings Advanced Microsystems for Automotive Applications Conference, pp. 173-182.

[87] Dierickx, B., Scheffer, D., Meynants, G., Ogiers, W., Vlummens, J., 1996, Random addressable active pixel image sensors. In: Advanced Focal Plane Arrays and Electronic Cameras. SPIE, pp. 2-7.

[88] http://www.vector-international.be/C-Cam/sensors.html

[89] C-Cam Technologies, 1998, Fuga Data Sheets, Belgium.

[90] Kolb, C., Mitchell, D., Hanrahan, P., 1995, A Realistic Camera Model for Computer Graphics, SIGGRAPH '95 Conference Proceedings, pp. 317-324.

[91] Thorlabs, 2002, The Thorlabs Catalog, Volume 14, Thorlabs Inc, USA.

[92] National Instruments Corporation, 1996, LabVIEW User Manual, National Instrument Corporation, Austin, Texas.

[93] http://www.dcs.ed.ac.uk/home/mxr/gfx/2d/BMP.txt

[94] Khosrofian, J. M., Garetz, B. A., 1983, Measurement of a Gaussian Laser Beam Diameter Through the Direct Inversion of Knife-Edge Data, Applied Optics, 22, 21, pp. 3406-3410.

[95] Malz, R. W., 1999, Principles of Three-Dimensional Imaging Techniques, Handbooks of Computer Vision and Applications, 1, Academic Press, San Diego.

Appendix A

LASER DIODE MODULE

Type number: CPS186

Properties
Housing: Aluminum
Lens: Glass
Type of laser N-type

Features
Operating temperature: -10 to 60°C
Storage temperature: -40 to 85°C
Application: Test & Measurement
Alignment

Reference data:

Symbol	Parameter	Conditions	Min	Typ	Max	Unit
	Wavelength			670	680	nm
P_0	Optical output power	100 mm from pen	4.0		4.5	MW
D⊥x D//	Beam diameter perpendicular x parallel to the laser stripe	FWHM at pen exit		4.4 1.2		mm mm
θ⊥x θ//	Beam divergence	Including natural divergence			0.6 1.8	mrad mrad
α_{om}	Optical-mechanical axis deviation			7	15	mrad
D_{ca}	Clear aperture			4.4		mm
I_{op}	Operating current laser pen			55		mA
V_{op}	Operating voltage	With reference to ground	-4.5	-5	-5.5	V

Laser pen dimensions

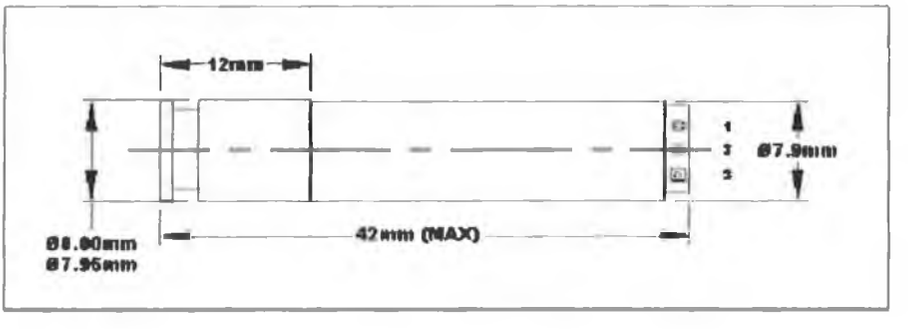

Pinning
1 = -5V
2 = Not connected
3 = Ground

Operating and Handling Precautions

Semiconductor laser diodes in general are easily damaged by overdriving and by electrical transients. The laser diode is highly susceptible to damage because of the extremely high optical flux density passing through both facets while in operation. In case of overdriving or of transients the optical flux density can rise to unacceptable values, causing catastrophic failure or gradual damage of the laser diode facets. Current transients should therefore be carefully avoided since they may destroy the laser or substantially decrease the laser diode lifetime. Before connecting the laser diode to the supply circuit, make sure that there are no transients that could make the laser diode output exceed the maximum rating for radiant flux or forward current. The following precautions should be taken to avoid failure of the device:

- Workers and workbenches should be grounded to a common stable earth at all times when working with laser diodes.
- All equipment, including power supplies, soldering irons, etc. must be grounded to a common stable earth.
- Power supplies should be well regulated and free of transients.
- Drive circuit connections should be made either by soldering or by high reliability connectors. Clip leads such as alligator clips are not recommended. Mechanically unreliable contacts cause transients and destroy the laser diode.
- Maximum soldering temperature is 250°C for a maximum of 5 seconds.
- Drive circuits should include a 'slow start and stop' feature to suppress turn-on/turn-off transients.
- High quality and high reliability components should be used throughout the drive circuits.
- It is recommended that the laser diodes be driven by an Automatic Power Control (APC) circuit, using the built-in monitor photodiode in a feedback loop to maintain constant optical power output over the full operating temperature range and throughout the life of the device.
- Always store laser diodes in static-free containers and use a short-circuit connector.
- Never connect or disconnect any components or external equipment such as voltmeters, to or from the device circuit while the power is on.
- Avoid touching the glass window. If necessary, clean gently with a cotton swab dampened with alcohol.
- Leads have to be soldered to their environment without mechanical stress. Any force during and after mounting must be avoided.
- Mechanical clamping should take place along the cylinder without any mechanical deformation of the housing (advised maximum force: 20 N).
- Do not look into the operating laser diode through a microscope!

Appendix B

CCf 15 Camera Specifications

Sensor Specifications

Imager Type:	CMOS integrating active pixel sensor (APS) Fuga15d designed by IMEC -FillFactory
Sensor Types:	Fuga15d Monochrome
Total Pixels:	262,144 (512H x 512V)
Total Light-Sensitive Pixels:	262,144 (512H x 512V)
Window of interest (WOI):	Any rectangle or line image format and even single pixels can be specified by the user
Active Image Area:	6.4 mm (H) x 6.4 mm (V)
Pixel Pitch:	12.5 x 12.5 µm
Fill Factor:	15 %
Spectral Response:	More than 30 %
Blooming:	Non-existent
Smear:	From 8 mW/cm2
Standard Dynamic Range:	120 dB
Grey Level Resolution:	8 bits or 256 grey levels
MTF:	0.35 @ Nyquist with 500 nm light
Response Time:	4 ms @ 0.04 W/cm2 and 400 µs @ 0.4 W/cm2 (650 nm)

Image Specifications

Pixel Rate:	Approx. 3.7 MHz (typical)
Frame Speed Full Resolution:	Approx. 14 frames/second (raw speed)
Frame Speed:	WOI Depending on frame size and selected readout speed (extreme high)

Exposure time:	Not applicable for this kind of sensor
Shutter:	Not applicable for this kind of sensor

Interface Specifications

Interface Type:	Digital LVDS (Texas Instruments) bi-directional (LVDM)
Remote Control:	Via Digital LVDS interface
Interface connector:	SCSI 50 pins connector
Cable Lengths:	1, 3, 5 or 10 meters from camera to PC interface

Mechanical Specifications

Dimensions:	Approx. 115 x 60 x 50 mm (not including lens)
Weight:	Approx. 450 grams (not including lens)
Housing:	Aluminum
Lens Adapter:	C-mount standard black anodized
Microscope Adapter:	1.25 inch Push-Fit adapter black anodized (optional)
Tripod mount:	1/4 inch mount (1 off)
Machine mount:	M6 x 1 (2 off)

Environmental Requirements

Operating temperature:	0°C to +50°C
Storage temperature:	-30°C to +80°C in noncondensing conditions

Power Requirements

Power supply voltage:	from PC through SCSI cable when used with standard I/O PCILVDS interface 8 – 12 Volts DC only if used with third-party digital frame grabbers

Appendix C1

Kinematic Mount

Product Number: KC1-T/M

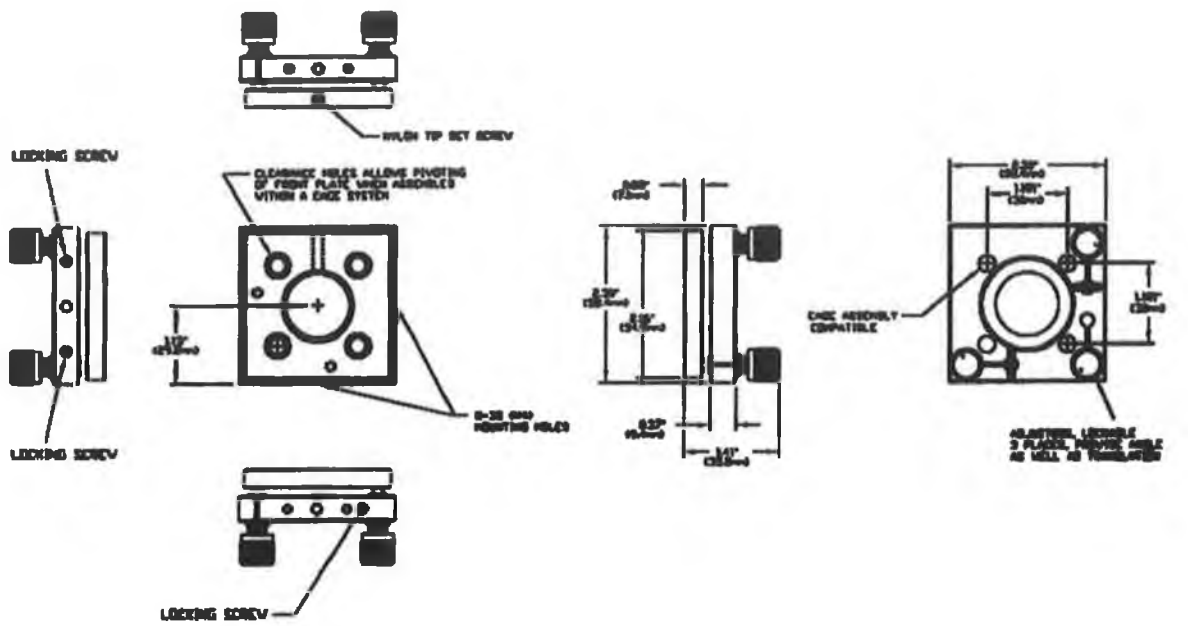

KC1

ANGULAR DISPLACEMENT ±5°
ANGULAR DISPLACEMENT PER REVOLUTION: 0.4°
TRANSLATIONAL DISPLACEMENT: ±3mm

SPECIAL NOTE ON THE LOCKING MECHANISM: FOR BEST RESULTS THE LOCKING SCREWS SHOULD BE TIGHTENED AND THEN RELEASED ONLY ENOUGH TO ALLOW FOR SMOOTH OPERATION OF THE THREE ADJUSTERS.

IF ADJUSTERS ARE LEFT LOOSE, EXCESSIVE PLAY IN THE ADJUSTER SCREWS WILL RESULT IN DRIFT OF THE FRONT PLATE.

Appendix C2

Post: TR75/M

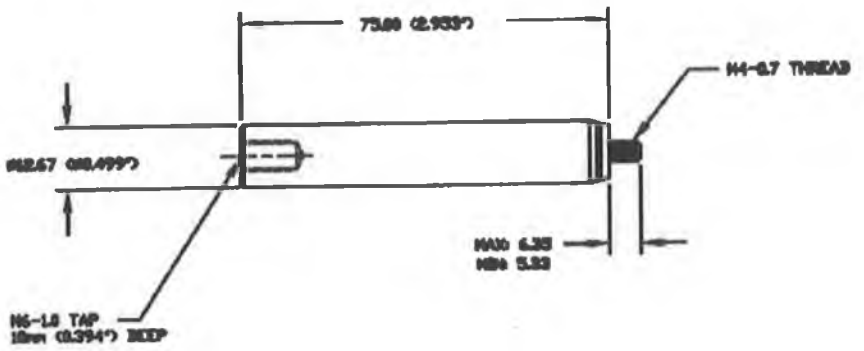

Appendix C3

Post Holder: PH3/M

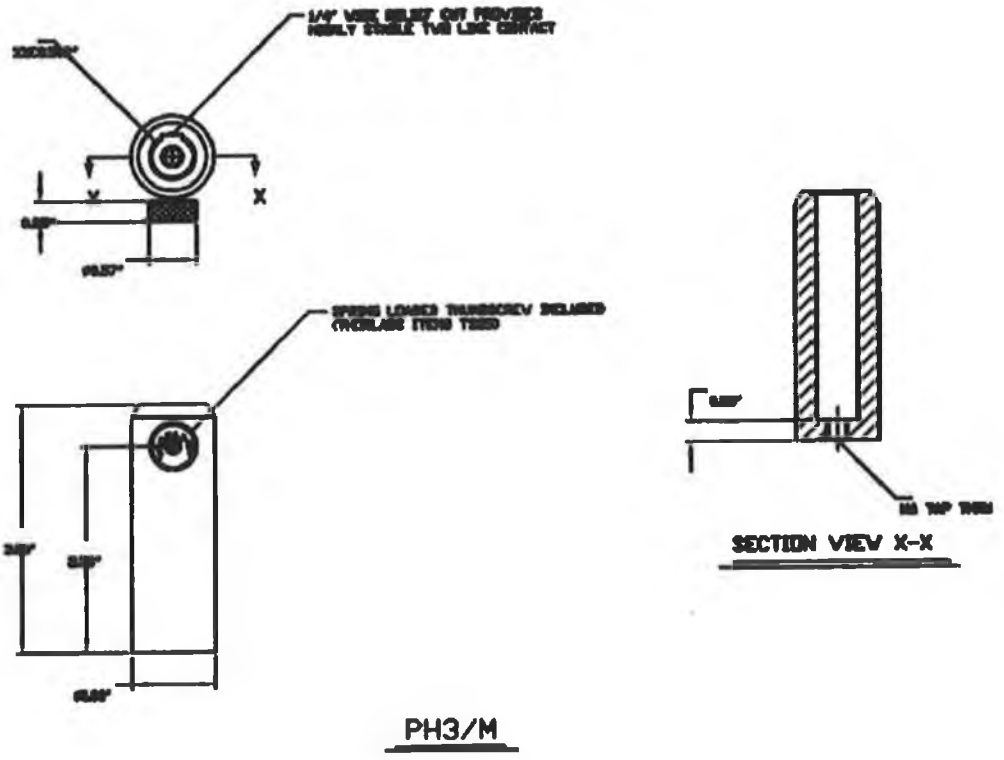

Appendix D

Objective Lens

Model: L25F1.4

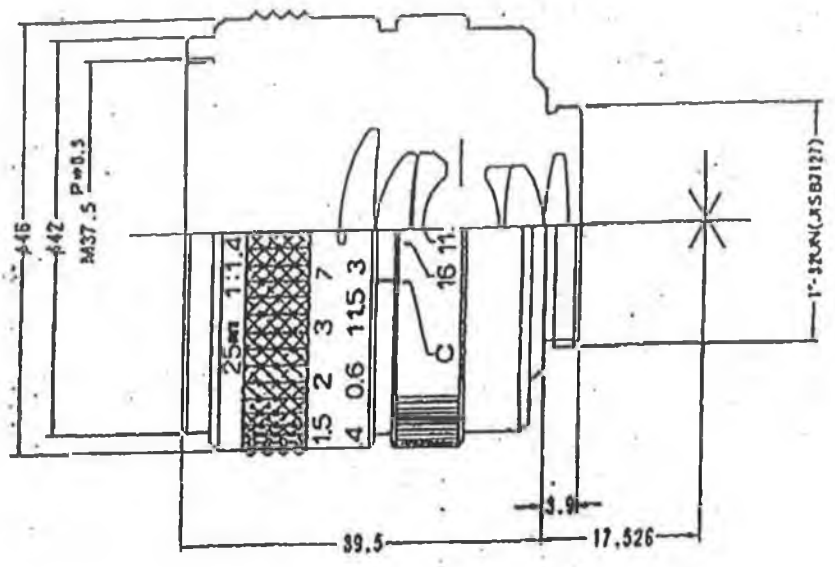

Specifications:

Part Number	2514	No of Elements	6 ele./ 5 groups
E F L	25 mm	O/I	NA
F/Number	1.4	Magnification	NA
Iris	1.4-16 C	Distortion	NA
Object Size Image Size	12.8x9.6 mm (Φ 16mm)	Lens Coating	Mgf2
Field of view D H V	35.0° 28.0° 21.0°	Clear Aperture	F 21mm R 15mm
B F L	14.9mm	Filter Size	37.5 mm
F F L	NA	Min. Obj. Dist.	0.3mm
Resolution	CTR 100 L/mm CTR 40 L/mm	Barrel Dimensions	Dia 46 mm Length 39.5mm Weight 90g

Electrophysics Corporation

Appendix E

The following table describes the different programs developed using LabVIEW software. Programs written in LabVIEW are known as virtual instrument (VI). This table lists the different VIs, their functions and the associated subVIs.

Name of the VI	Function of the VI	Associated SubVI
3D SURFACE MAPPING.VI	This VI reads the images recorded by scanning the surface and generate 3-D topographic map of the surface.	- CENTROID_X.VI - CENTROID_Y.VI - FPIXEL.VI
SURFACE MAPPING.VI	This VI reads the scanned surface images and produces a 2-D displacement characteristic of the surface.	- CENTROID_X.VI - CENTROID_Y.VI - FPIXEL.VI
CALIBRATION.VI	This VI is used to calibrate the developed inspection.	- CENTROID_X.VI - CENTROID_Y.VI - FPIXEL.VI
CENTROID_X.VI & CENTROID_Y.VI	These two VIs perform the calculation to measure the laser beam centroid positions in the images.	
FPIXEL.VI	This VI reads the bitmap image file and converts it into text format.	Read BMP header inf.VI
Read BMP header inf.VI	This VI reads the header information out of the BMP image file.	